



MONASH University

Problems in Low Mass Stellar Rotation

Tanner A. Wilson

Doctor of Philosophy

A Thesis Submitted for the Degree of Doctor of Philosophy at
Monash University in 2023
School of Physics and Astronomy

Copyright notice

Insert one of the following notices.

Notice 1

©[Tanner A. Wilson](#) (2021).

The second notice certifies the appropriate use of any third-party material in the thesis. Students choosing to deposit their thesis into the restricted access section of the repository are not required to complete Notice 2.

Notice 2

©[Tanner A. Wilson](#) (2021).

I certify that I have made all reasonable efforts to secure copyright permissions for third-party content included in this thesis and have not knowingly added copyright content to my work without the owner's permission.

Abstract

The abstract should outline the main approach and findings of the thesis and must not be more than 500 words.

The Thesis Abstract is written here (and usually kept to just this page). The page is kept centered vertically so can expand into the blank space above the title too...

Declaration

This thesis is an original work of my research and contains no material which has been accepted for the award of any other degree or diploma at any university or equivalent institution and that, to the best of my knowledge and belief, this thesis contains no material previously published or written by another person, except where due reference is made in the text of the thesis.

Signature:

Print Name: Tanner A. Wilson

Date:

Thesis including published works declaration

This declaration is to be included in a ‘thesis including published works’. You must provide details of all publications included in your thesis in the section below. If you have not completed a thesis including published works.

Please ensure your thesis meets the [thesis including published works requirements](#). Some faculties vary requirements in terms of the number of papers required, status of papers and other criteria. These faculty specific requirements can also be found at the above link.

Please remove the above section and include a standard thesis declaration.

I hereby declare that this thesis contains no material which has been accepted for the award of any other degree or diploma at any university or equivalent institution and that, to the best of my knowledge and belief, this thesis contains no material previously published or written by another person, except where due reference is made in the text of the thesis.

This thesis includes (*insert number*) original papers published in peer reviewed journals and (*insert number*) submitted publications. The core theme of the thesis is (*insert theme*). The ideas, development and writing up of all the papers in the thesis were the principal responsibility of myself, the student, working within the (*insert name of academic unit*) under the supervision of (*insert name of supervisor*).

(The inclusion of co-authors reflects the fact that the work came from active collaboration between researchers and acknowledges input into team-based research.) *Remove this paragraph for theses with sole-authored work*

In the case of (*insert chapter numbers*) my contribution to the work involved the following:

(If this is a laboratory-based discipline, a paragraph outlining the assistance given during the experiments, the nature of the experiments and an attribution to the contributors could follow.)

Here should be the table!

I have / have not renumbered sections of submitted or published papers in order to generate a consistent presentation within the thesis.

Student name:

Student signature: Date:

I hereby certify that the above declaration correctly reflects the nature and extent of the student's and co-authors' contributions to this work. In instances where I am not the responsible author I have consulted with the responsible author to agree on the respective contributions of the authors.

Main Supervisor name:

Main Supervisor signature: Date:

Publications during enrolment

You may wish to list your publications arising from your research degree enrolment using the standard citation format of your academic unit. Remove this section if you do not have publications.

Journal articles:

- 1) Dong, Xingbo, Zhe Jin, and Andrew Teoh Beng Jin. "A genetic algorithm enabled similarity-based attack on cancellable biometrics." 2019 IEEE 10th International Conference on Biometrics Theory, Applications and Systems (BTAS). IEEE, 2019.
- 2) xxx

Preface

Where applicable, the following information must be included in a preface:

- a description of work towards the thesis that was carried out in collaboration with others, indicating the nature and proportion of the contribution of others and in general terms the portions of the work which the student claims as original;
- a description of work towards the thesis that has been submitted for other qualifications;
- a description of work towards the thesis that was carried out prior to enrolment in the degree;
- whether any third party editorial assistance was provided in preparation of the thesis and whether the persons providing this assistance are knowledgeable in the academic discipline of the thesis;
- the contributions of all persons involved in any multi-authored publications or articles in preparation included in the thesis;
- the publication status of all chapters presented in article format using the descriptors below;
 - Unpublished material not submitted for publication
 - Submitted for publication to [publication name] on [date]
 - In revision following peer review by [publication name]
 - Accepted for publication by [publication name] on [date]
 - Published by [publication name] on [date]
- an acknowledgement of all sources of funding, including grant identification numbers where applicable and Australian Government Research Training Program Scholarships, including fee offset scholarships.

Acknowledgements

In accordance with Chapter 7.1.4 of the research degrees handbook, if you have engaged the services of a professional editor, you must provide their name and a brief description of the service rendered. If the professional editor's current or former area of academic specialisation is similar your own, this too should be stated as it may suggest to examiners that the editor's advice to the student has extended beyond guidance on English expression to affect the substance and structure of the thesis.

Free text section for you to record your acknowledgment and gratitude for the more general academic input and support such as financial support from grants and scholarships and the non-academic support you have received during the course of your enrolment. If you are a recipient of the "Australian Government Research Training Program Scholarship", you are required to include the following statement:

"This research was supported by an Australian Government Research Training Program (RTP) Scholarship."

You may also wish to acknowledge significant and substantial contribution made by others to the research, work and writing represented and/or reported in the thesis. These could include significant contributions to: the conception and design of the project; non-routine technical work; analysis and interpretation of research data; drafting significant parts of the work or critically revising it so as to contribute to the interpretation.

Contents

Copyright notice	i
Abstract	ii
Declaration	iii
Thesis including published works declaration	iv
Publications during enrolment	vi
Preface	vii
Acknowledgements	viii
List of Figures	xi
List of Tables	xvi
Abbreviations	xviii
Constants	xix
Symbols	xx
1 Introduction	1
1.1 History of observation of rotation	2
1.2 Evolution of rotation	5
1.2.1 Birth - Terminal age main sequence	5
1.2.2 Post-main-sequence	19
1.3 Effects of rotation	31
1.3.1 Hydrostatic effects	31
1.3.2 Increased mixing in stars	32
1.3.2.1 Dynamical shear instability	34
1.3.2.2 Solberg-Høiland instability	35
1.3.2.3 Secular shear instability	36
1.3.2.4 Meridional circulation	37
1.3.2.5 Goldreich-Shubert-Fricke instability	39
1.3.3 Magneto-rotational instabilities	40
1.3.3.1 Tayler instability and the Spruit Dynamo	40
1.3.3.2 Azimuthal Magnetorotational instability	41

1.3.4	Other angular momentum transport mechanisms	42
1.3.5	Implementation of diffusive processes in models of rotating stellar evolution	43
1.3.5.1	Transport of Angular momentum	43
1.3.5.2	Transport of Elements	44
1.3.6	Stellar Winds	44
1.3.7	Summary - Effects of rotation on low-mass evolution	48
1.3.7.1	Pre-main sequence	48
1.3.7.2	Main sequence	49
1.3.7.3	Post-main sequence	50
1.4	Todo	51
2	Constraining the Rotation Profile in a Low-Luminosity Subgiant with a Surface Rotation Measurement	52
3	Stellar spots cause measurable variations in atmospheric metallicity	62
4	The Intermediate Period Gap	72
4.1	Introduction	74
4.2	Stellar magnetic activity indicators	78
4.3	The gap aligns with a minima in photometric variability	81
4.4	The gap aligns with a minima in $\log R_{\text{HK}}^+$	88
4.5	Is there a sample of low-magnetic activity stars without rotational period detection?	92
4.6	Latitudinal differential rotation	98
4.7	Summary, Discussion, and Future Work	106

List of Figures

- | | | |
|-----|--|----|
| 1.1 | Normalised 2D histograms of the <i>Kepler</i> (McQuillan et al., 2014) (Top), <i>Gaia</i> DR3 (Distefano et al., 2022) (Middle), and Zwicky Transient Facility (<i>ZTF</i>) (Lu et al., 2022) (Bottom) samples. Each sample probes a different area of the rotational period against colour space with some overlap. This expands our knowledge of the evolution of rotation to different types of stars while the agreement between these samples confirms their independent accuracy. | 7 |
| 1.2 | Angular rotation rate (relative to solar) distributions of low-mass young open clusters and the Sun. Triangles, inverted triangles, and squares represent the 90 th , 25 th , and median rotation rates of the cluster. Open circle denotes the present value of the rotation rate of the Sun. Median values indicate that the rotation rate of cluster is approximately constant with age, despite the spin up by accretion. In order of increasing age (left to right) the clusters are ONC (1 Myr) (Herbst et al., 2002), NGC 6530 (Henderson & Stassun, 2012), NGC 2264 (2 Myr) (Affer et al., 2013), NGC 2362 (5 Myr) (Irwin et al., 2008), h PER (13 Myr) (Moraux et al., 2013), NGC 2547 (40 Myr) (Irwin et al., 2008), Pleiades (120 Myr) (Hartman et al., 2010), M50 (130 Myr) (Irwin et al., 2009), M35 (150 Myr) (Meibom et al., 2009), M37 (550 Myr) (Hartman et al., 2009), Praesepe (578 Myr) (Delorme et al., 2011), Hyades (625 Myr) (Delorme et al., 2011), and NGC 6811 (1 Gyr) (Meibom et al., 2011). Sourced from Gallet & Bouvier (2013), Figure 1. | 9 |
| 1.3 | Scatter plot of various cluster rotational periods against effective temperature overlayed on the <i>Kepler</i> McQuillan et al. (2014) rotational period sample. The agreement between low mass Praesepe and NGC6811 periods implies mass dependent core-envelope coupling for young (<1 Gyr) stars. Sourced from Top left panel of Figure 7 in Curtis et al. (2020) | 10 |
| 1.4 | Scatter plot <i>Gaia</i> $B_P - R_P$ colour against log of the rotational period of the <i>Kepler</i> McQuillan et al. (2014) rotational period sample coloured by the log of the photometric variation (R_{var}). R_{var} decreased towards the gap from above and below, suggesting the intermediate period gap is representative of a minimum of observability of rotation period. Highlighted by arrows in this Figure are two features that we discuss in more detail in this Section: the intermediate period gap and the long-period pile-up. | 13 |

1.5	Rotation period against $Gaia B_P - R_P$ from <i>Kepler</i> , <i>ZTF</i> overlayed with various open cluster measurements. Highlighted by this Figure is the disappearance of the intermediate period gap above $B_P - R_P = 2.5$ - the fully convective star boundary. This suggests that the rotational period gap is related to the coupling of the core and surface of low mass stars ($0.4 M_{\odot} < M < 1.3 M_{\odot}$). Sourced from the top panel of Figure 8 in (Lu et al., 2022)	16
1.6	Core (red) and surface (blue) rotation rates with additional angular momentum transport following the prescription of Spada et al. (2016). Coloured sections denote evolutionary milestones and the works that have provided constraints to these milestones. Pink: subgiant core and surface rotation, Orange: red giant branch cores, Green: clump core rotation rates, and Purple: white dwarf rotation rates. Adapted from Figure 3 in Fuller et al. (2019)	21
1.7	log of core to surface rotation rate against $\log g$. Dots: Observed core to surface rotation rates of the six subgiants measured in the Deheuvels et al. (2014) sample (A,B,C,D,E,F). Lines: rotating models of the stars in that sample without additional angular momentum transport (Eggenberger et al., 2019). The observed core-to-surface rotation rates are much smaller than models predict. This implies additional angular momentum transport than is currently accounted for models. Sourced from Figure 2 in (Eggenberger et al., 2019)	23
1.8	Same as Figure 1.7 but with additional angular momentum transport introduced for the models to reflect the observations. Sourced from Figure 3 in (Eggenberger et al., 2019)	24
1.9	Average core rotation rates of red giants against mixed mode density (a proxy for evolution) Dots: Observed core rotation rates from Gehan et al. (2018) Lines: rotating models of the stars in that sample without additional angular momentum transport (Moyano et al., 2022). The observed core rates are much smaller than models predict. Implying excess angular momentum transport is required for the models to reflect the observations. Sourced from Figure 6 in (Moyano et al., 2022)	25
1.10	Same as Figure 1.9 but with additional angular momentum transport introduced for the models to reflect the observations. Sourced from Figure 7 in (Moyano et al., 2022)	26
1.11	Surface rotation period against effective temperature of subgiants in the Santos et al. (2021) sample overlayed over the <i>Kepler</i> McQuillan et al. (2014) sample. Sourced from the bottom panel of Figure 5 in (Santos et al., 2021)	29
1.12	Surface rotation period against mass of red giant stars from Ceillier et al. (2017). Sourced from the top panel of Figure 7 in (Ceillier et al., 2017)	30
1.13	Left: PMS HR diagram tracks of $1 M_{\odot}$ solar metallicity models with and without rotation. The continuous line corresponds to a non-rotating model, while the dashed line corresponds to a rotating model with $\Omega = 20\Omega_{\odot}$. The tracks end when the ZAMS is reached. Right: Surface lithium abundance with time during the PMS for the same models. Sourced from Figure 1 in Eggenberger (2013)	48

1.14 Left: MS HR diagram tracks of $1 M_{\odot}$ solar metallicity models with and without rotation. The continuous line corresponds to a non-rotating model, while the dashed line corresponds to a rotating model with ZAMS surface velocity = 50 km/s. The tracks end when the ZAMS is reached. Right: Surface helium abundance with time during the MS for the same models. Sourced from Figure 3 in Eggenberger (2013)	50
4.1 HR diagram of the closeby rotating main-sequence sample colours by photometric variability (R_{per})	82
4.2 \log_{10} of the rotation period against $GaiaB_P - R_P$ colour of the closeby rotating main-sequence sample colours by photometric variability (R_{per}). In this Figure, we can see observe the decrease in the photometric variability of stars near the gap.	82
4.3 2D binned photometric variability (R_{per}) for the slices of \log_{10} of the rotation period and colour $GaiaB_P - R_P$ used in this work. Comparing this Figure and 4.2, the alignment of the minima of photometric variability and observation of stars in the gap can be seen.	83
4.4 Median and median absolute deviation of photometric variability (R_{per}) against \log_{10} of the rotation period in bins of and colour $Gaia B_P - R_P$ (indicated in brackets). Here we have fitted a cubic spline to median R_{per} and calculated minima using the first and second derivatives of the fitted cubic spline. Solid vertical blue lines show the minima here. These minima align with the rotational period gap.	85
4.5 The position of the identified minima in R_{per} against rotational period using the full close-by rotating main-sequence Kepler sample, the R_{per} minima identified with the Kepler LAMOST crossmatch and the $\log_{10} R_{HK}^+$ minima identified with the Kepler LAMOST crossmatch.	86
4.6 Median and median absolute deviation of photometric variability (R_{per}) (blue) and $B_P - R_P$ (orange) against \log_{10} of the rotation period in bins of and $Gaia B_P - R_P$ colour (indicated in brackets). The position of the minima in R_{per} do not align with maxima or minima in $B_P - R_P$ implying that the colour bias when fitting across the dearth can be the cause of the R_{per} minima.	87
4.7 The LAMOST chromospherically active and Kepler rotating closeby, main-sequence cross-match \log_{10} of rotational period \log_{10} against $GaiaB_P - R_P$ colour coloured by $\log_{10} R_{HK}^+$. It is unclear from this whether $\log_{10} R_{HK}^+$ decreases toward the gap like R_{per}	89
4.8 Median and median absolute deviation of photometric variability (R_{per}) (blue) and LAMOST $\log_{10} R_{HK}^+$ against \log_{10} of the rotation period in bins of and colour $Gaia B_P - R_P$ (indicated in brackets). Here we have fitted a cubic spline to the median of these values in each bin and calculated minima using the first and second derivatives of the fitted cubic spline. The minima in R_{per} are shown by solid vertical blue lines, while the minima in $\log_{10} R_{HK}^+$ are shown in solid vertical orange lines. These minima align with each other and the rotational period gap.	90
4.9 HR diagram of the closeby rotating (top) and non-rotating (bottom) main-sequence sample crossmatched with the LAMOST-Kepler field coloured by the chromospheric magnetic activity indicator $\log R_{HK}^+$. Comparing these two samples, we observe very few low-mass stars for which the rotation period is undetected.	93

4.10 The probability density function (left) and cumulative probability density function (right) of $\log R_{HK}^+$ are separated by whether rotation was or was not detected in the close-by main-sequence LAMOST-Kepler crossmatch. We expect less magnetically active stars to have a lower detection rate due to the decrease in prominence of stellar spots with lowering magnetic activity. This is supported by the data here as the non-rotation detected sample contains a larger number of low $\log R_{HK}^+$ stars.	94
4.11 The detectability of rotation (top) and 2D histogram of stars without detected rotation periods (bottom) across <i>Gaia</i> $B_P - R_P$ colour and $\log R_{HK}^+$. Rotation is preferentially measured in stars with higher magnetic activity (larger $\log R_{HK}^+$) and tends to increase with colour. Low-mass stars have a high probability of rotation being measured. Stars with low magnetic activity have a lower likelihood of rotational observation. Bins with detection efficiency equal to zero or one tend to contain single stars, with detected rotation or without detected rotation, respectively and are not indicative of trends in the detection efficiency. We do not observe an ultra-low magnetic activity population with non-detected rotation that would be required to explain the lack of observation of stars in the intermediate period gap. While there are stars with ultra-low $\log R_{HK}^+$ (<5.5) in each $B_P - R_P$ bin they can either both rotationally detected or not rotationally detected. The ultra-low magnetic activity does not indicate their lack of rotational observation probability.	95
4.12 A histogram of the distribution of $B_P - R_P$ colour of stars with (green) and without (red) detected rotation periods. Inset: A zoom-in of the distribution for $B_P - R_P \geq 1.5$ where the rotational period gap is most apparent. The distribution in colour of stars with and without detected rotation periods vary. The undetected rotation sample is strongly biased towards stars with $B_P - R_P$ close to 1, comparative to the lower-mass stars where the number of stars drops quickly. Despite the $\sim 3:1$ ratio of the number of stars with undetected rotation periods to those with detected rotation periods, the number of stars without detected rotation periods drops below those with detected rotation at $B_P - R_P \geq 1.3$	97
4.13 Number of stars in each bin against \log_{10} of the rotation period in bins of colour <i>Gaia</i> $B_P - R_P$ (indicated in brackets). Here we have fitted a cubic spline to the number of stars in each bin and calculated minima using the first and second derivatives of the fitted cubic spline. Solid vertical black lines show the minima in number of stars. These minima are the rotational period gap.	99
4.14 The number of stars required to fill the gap (black scatter points) against the number of stars with undetected rotation periods against $B_P - R_P$. The number of stars required to fill the intermediate period gap is roughly constant at $N \sim 20$. While the number of stars without detected rotation greatly outnumbers the number required to fill the gap below $B_P - R_P \sim 1.8$, the two are almost equal for lower mass stars.	100

- 4.15 The various relationships between latitudinal differential rotation and the stellar R_o adopted in this work. We compare between the observationally derived relation from Saar (2011) (orange) and two steeper relations for $R_o \leq 0.45$, $|\Delta\Omega|/\Omega \propto R_o^4$ (green) and $|\Delta\Omega|/\Omega \propto R_o^6$ (purple). The scale of differential rotation is greater for the latter two relations and we have an increase to the scale of differential rotation for $R_o \geq 2$. All three relations are consistent with the magnetohydrodynamic investigations into stellar differential rotation from Brun et al. (2022). 106
- 4.16 The effect of the differential rotation on the observed rotational period of a $0.7 M_\odot$ star. Here the colour of the relations corresponds to the adopted differential rotation relation in Figure 4.15 compared to the observed rotation profile of a latitudinally flat rotating star. At $R_o < 0.45$ for injected rotation periods ($P_{\text{rot,injected}}$) less than 20 days. It is evident that steeper relations between R_o and differential rotation lead to more rapid growth in observed rotation periods for the same injected period. Moreover, a steeper growth in the observed rotational period corresponds to a lower number of observed stars with that particular rotation period. The transition from solar-like to anti-solar-like rotation, occurring at $P_{\text{rot,injected}} = 70$ days, results in an instantaneous shift in observed rotational periods from being greater than the injected value to being less than the injected value. 107
- 4.17 The observed rotational period distributions of the synthetic sample of stars given various relations between latitudinal differential rotation and R_o overlayed over the observed distribution of rotational periods of the Kepler sample from McQuillan et al. (2014) (black). Here, the coloured observed rotational period distributions correspond to the various differential rotation relations adopted in this work, as seen in Figure 4.15. The latitudinally flat (blue, top left) sample reflects the injected rotational periods of our sample considered in this work. We observe that there is no intermediate period gap in this synthetic sample of stars without differential rotation. If we include the effects of differential rotation on the observed rotation period, a dearth of observations at the transition between latitudinally flat ($R_o < 0.45$) and solar-like rotation occurs precisely at the location of the intermediate period gap. Further, we find that as the steepness of the relation between $|\Delta\Omega|/\Omega$ increases (where in order of increasing steepness, we have the orange, green and purple distributions) the gap becomes more distinct - fewer stars are observed within the gap. We also find that due to the transition from solar-like to anti-solar-like differential rotation, we obtain an over-density of stars consistent with the overdensity of slow-rotating stars near 6000K. See ?? for 2D histograms of the distribution of rotation periods in these panels. . 108
- 4.18 A 2D histogram of the synthetic observed rotational period distribution assuming various relations between the scale of differential rotation and R_o . Here, the panels correspond to the same panels in Figure 4.17. 109

Write shortened figure list names.

List of Tables

Abbreviations

LAH List Abbreviations Here

Constants

Speed of Light c = $2.997\ 924\ 58 \times 10^8$ ms^{-s} (exact)

Symbols

a	distance	m
P	power	W (Js ⁻¹)
ω	angular frequency	rads ⁻¹

Chapter 1

Introduction

Humans have been captivated by the stars since the dawn of civilisation, and this fascination has driven our curiosity and drive to understand the universe around us. The history of astronomy is rich and diverse. Indigenous cultures still use the stars for navigation, seasonal calendars, and mythological stories. Since the invention of the modern telescope, some would say the birth of modern astronomy in the 16th century, to the launch of the James Webb space telescope, technology has advanced during the period that this PhD was undertaken. Our ability to observe and study the stars has grown in scale and sophistication.

Each observation that we make improves our understanding of the underlying physics of the universe. In recent years the sheer amount of data available to astronomers has increased dramatically due in part to technological advances, such as space-based observatories, which allow us to perform large sky surveys in unprecedented detail. It is clear from these studies that our models of the universe are lacking in a number of important physical processes. One of these physical processes that are particularly not well understood is the evolution of stellar rotation¹.

This introductory chapter is intended to provide context for the reader to understand the following science chapters. The introductory chapter is broken down into the following sections of increasing level of detail:

Section 1.1 provides a historical overview of the history of astronomical observation and briefly introduces the techniques used to observe the rotation of stars. Section

¹Infact a majority of models of stellar evolution completely ignore angular momentum transport

1.2 reviews our current understanding of the evolution of rotation from birth, through post-main-sequence evolution, to the remnants of rotating stars. Within this Section we also describe what we call the "problems of stellar rotation" that we have attempted to address in this work. Section 1.3 describes the astrophysical effects of rotation on stellar evolution.

The scientific works in this thesis are motivated by the problems in stellar rotation that are described in detail in this introduction. As a result, this introduction will overlap with the introductions of the scientific works' topics and serve as a companion for readers unfamiliar with the topic.

1.1 History of observation of rotation

In this section, we look back at the history of observing stellar rotation, how observations of stellar rotation are performed, the qualitative effects of rotation on stellar rotation and some of the problems that the big-data boom of astronomy has identified. This discussion will provide the necessary background to our attempts to understand and constrain the astrophysical process that underlies these problems.

The history of observing the rotating stars began with observations of the Sun². In approximately 1610, Galileo reported evidence of sunspots and tracked their motion in his book "l'Istoria e dimostrazioni intorno alle macchie solari e loro accidenti". He interpreted the motion of stellar spots on the surface of the Sun as a result of its rotation. Adding onto this work in 1630, Christoph Scheiner found that the stellar spots had different rotational periods at the poles and the equator - measurements that agree with modern observations of the Sun. This was the first observation of latitude-dependent rotation - more commonly known as latitudinal differential rotation.

The history of observing stellar³ rotation can be traced back to the early 20th century when astronomers first discovered that some stars they observed were rotating. They came to this conclusion through spectroscopic observations (Elvey, 1929; Struve & Elvey, 1930; Struve, 1930). They found that lines in their spectra were broadened due to the Doppler effect - a technique used to this day.

²as most astronomy does

³Here we make the distinction between the Sun and other stars through the use of the terms 'solar' and 'stellar' respectively

Around this time, astrophysicists such as Eddington (Eddington, 1918, 1926, 1929), Milne (Milne, 1923), von Zeipel (von Zeipel, 1924), and others delved into the theoretical aspects of the impact of rotation on stars. To simplify their work, they identified the effects of rotation on stellar structure, energy generation, shape and luminosity. Further, rotation induces mixing in stars that can transport angular momentum as well as elements. Advances in computational capabilities allowed astronomers to study the impact of rotation on the mixing of elements within stars in greater detail. This research revealed essential results: rotation significantly impacts the mixing of matter in stars. Enhanced mixing leads to an increased lifetime on the main sequence - hydrogen-rich material is transported to the core - and can create isotope anomalies, such as changes in the isotopic ratio $^{12}\text{C}/^{13}\text{C}$, nitrogen, oxygen and lithium enhancements (Maeder & Meynet, 2000; Heger et al., 2000; Charbonnel et al., 1994). Their results underlay our modern understanding of the impacts of stellar rotation on stellar evolution.

In the following decades, technological advances allowed for more precise photometric observations of stars. This paved the way for two techniques to obtain measures of the rotation of stars - stellar spot brightness modulation periods and asteroseismology.

Like with the Sun, stars were found to exhibit stellar spots. These spots cannot be realistically tracked on the surface of stars other than the Sun. They do, however, vary the star's observed brightness. With stellar spots tied to the star's rotation, these brightness variations are periodic. Measuring the period of brightness variation is used as a proxy for the rotation period⁴ of a star. Unlike the spectroscopic technique - where the inclination angle modulates the rotation rate - the rotational periods from stellar spot brightness modulations are more accurate to the star's actual rotation rate. As a result, this technique has made several fundamental discoveries about the evolution of stellar rotation. The accurate measurement of stellar rotation provides information to more accurately model a star's internal structure, dynamics and internal angular momentum transport - both at a specific point in evolution and with evolution. For example, it was found that the rate at which a star's surface rotates slows with time (Skumanich, 1972). Resultingly, measuring the stellar rotation can provide an imprecise measure of the age of a star⁵. Recent photometric missions such as Kepler (Borucki et al., 2010; Beck et al., 2011), Zwicky Transient Facility (ZTF) (Lu et al., 2022) and Gaia

⁴It is important to note here that the rotation period - time taken for one rotation - and rotation rate - frequency of rotation - of a star are not the same quantity. They are inversely related

⁵This is a contentious claim that we will discuss further in the coming sections

(Distefano et al., 2022) have provided a wealth of data, including a sample of 200,000 stellar rotational periods from stellar spot brightness modulations. Their results form the basis of a number of the problems in stellar rotation we discuss in this thesis.

Determining the rotation period of a star from stellar spots requires intermittent photometric measurements of stars - known as long-cadence observations - over the time scale of months. On the other hand, measurements made on the order of minutes - known as short cadence observations - reveal the internal structure of stars. Like bells, stars "ring" - or, more accurately, pulsate and thus vary in brightness - at particular frequencies related to the structure of the star. By measuring those frequencies, we can infer the internal structure of a star - for example, the density-sound speed profile of the star. Rotation introduces what are known as rotational splittings to the frequency profile. Rotational splittings vary between asteroseismic modes but are a weighted average of the rotation rate dependent on the structure of the star. Unlike brightness modulations from stellar spots and spectroscopic inference of rotation rate, asteroseismology can probe the rotation profile internal to the surface of a star.

Modern observations with asteroseismology⁶ have also found that the Sun, and most post-main-sequence stars, exhibit differential rotation along the radial axis - known as radial differential rotation. Measurement of the rotation profile of post-main-sequence stars has allowed us to probe these stars' internal mixing and angular momentum transport. It is important to note, however, due to the large amount of photometric data required to perform in-depth asteroseismic inference, the number of stars it has been performed on is only on the order of 100⁷ (Li et al., 2020b,a), and the constraints that state-of-the-art data can provide are limited. We would argue that the information that asteroseismology has provided has introduced more questions than currently answered.

The study of stellar rotation continues to advance and remains at the forefront of current research.

⁶and helioseismology for the Sun

⁷at the time of writing

1.2 Evolution of rotation

1.2.1 Birth - Terminal age main sequence

Before we discuss the observed evolution of rotation along the main sequence, we will briefly reflect on the methods of observing rotation in stars, where these methods are most conducive to understanding the evolution of rotation and their limitations. The three standard techniques of observing rotation in stars can be separated into three categories: measurement of the surface rotation period from stellar brightness oscillations owing to stellar spots, spectroscopic derivation of inclination projected surface velocity from doppler broadenings, and asteroseismology of rotational splittings. We will refer to these techniques by their data products: stellar spot rotation periods, spectroscopic rotation velocities, and asteroseismic rotation rates, respectively, for brevity. The results we discuss in this Section come from the inference of rotational evolution from stellar spot rotation. This results from two factors: stellar spot rotation periods are more accurate and less data and computationally intensive than their spectroscopic and asteroseismic counterparts.

While the spectroscopic rotation velocity has been inferred for orders of magnitude greater numbers of stars, the observed rotation rate is modulated by the inclination angle of the star relative to the observer ($v \sin i$). Constraining the evolution of rotation through spectroscopic rotation velocities of stars is only fruitful with independent constraints to stellar inclination. The stellar inclination is often difficult to measure as it requires either that the star is in a binary⁸ or that the star is intensively asteroseismically studied. As a result, only a few studies of the evolution of rotation rely on this data.

On the other hand, determining the rotation rate of stars with asteroseismology is computationally and data-intensive. We will discuss the difference in computational intensity in more detail when we outline how these methods are performed. Here we will focus on the difference data intensity. Obtaining high signal-to-noise asteroseismic signals of rotation requires short-cadence observations of stars over an observation period of 4 years

⁸and that the rotation axis aligns itself with the binary orbital inclination, which may always be the case [Albrecht et al. \(2011, 2013\)](#)

(Deheuvels et al., 2014). Short-cadence data is required because the oscillation frequencies of main-sequence stars must be greater than the Nyquist frequency of the observations. In the *Kepler* field, the cross-section of stars with both short-cadence observations and those observation periods long enough to obtain a high enough SNR to perform asteroseismic inference is very limited. Further, only limited constraints can be placed on the surface rotation rate from asteroseismology during the main sequence. Main-sequence stars only express p-mode⁹ solar-like oscillations with long lifetimes, which can only probe the structure of the convective surface region. Long mode lifetimes result in wide line widths of oscillations in the power spectrum. Main-sequence stars spend the majority of their lifetime slowly rotating. This results in rotational broadenings of the oscillations rather than distinct rotational splittings. Without precise measurements of the rotational splittings for many oscillation modes, precise inference of the surface rotation rates of main-sequence stars is limited.

The inefficiency of asteroseismic inference of rotation rates along the main sequence is best exhibited in Hall et al. (2021), who observed the asteroseismic surface rotation rates of 91 main-sequence stars. Figure 2. in Hall et al. (2021) compares the stellar spot rotation period with the surface rotation period from asteroseismic inference of the rotation profile. The surface rotation periods generally agree, confirming that the surface brightness oscillation period from stellar spots is indeed the surface rotation period. However, the rotation periods obtained from asteroseismology are much less precise than their stellar spot rotation period counterparts. Despite requiring much more data, the information provided by this technique is limited compared to stellar spot brightness modulation periods.

Stellar spot rotation period measurements can be made from long-cadence data with observation periods as low as 90 days (McQuillan et al., 2014). The technique employed to determine the rotation period is much less computationally intensive than required for asteroseismic inference of rotation rates. As a result and through the combination of various photometric missions, *Kepler* (McQuillan et al., 2014; Santos et al., 2021), *K2* (Santos et al., 2021), Zwicky Transient Facility (ZTF) (Lu et al., 2022), *Gaia* DR3 (Distefano et al., 2022) We show the rotational period distribution against colour (*Gaia* DR3 $B_P - R_P$) of the *Kepler* Mcquillan Sample, *ZTF* sample and *Gaia* DR3 samples in the top, middle and bottom panels of Figure 1.1 respectively.

⁹See Section ??

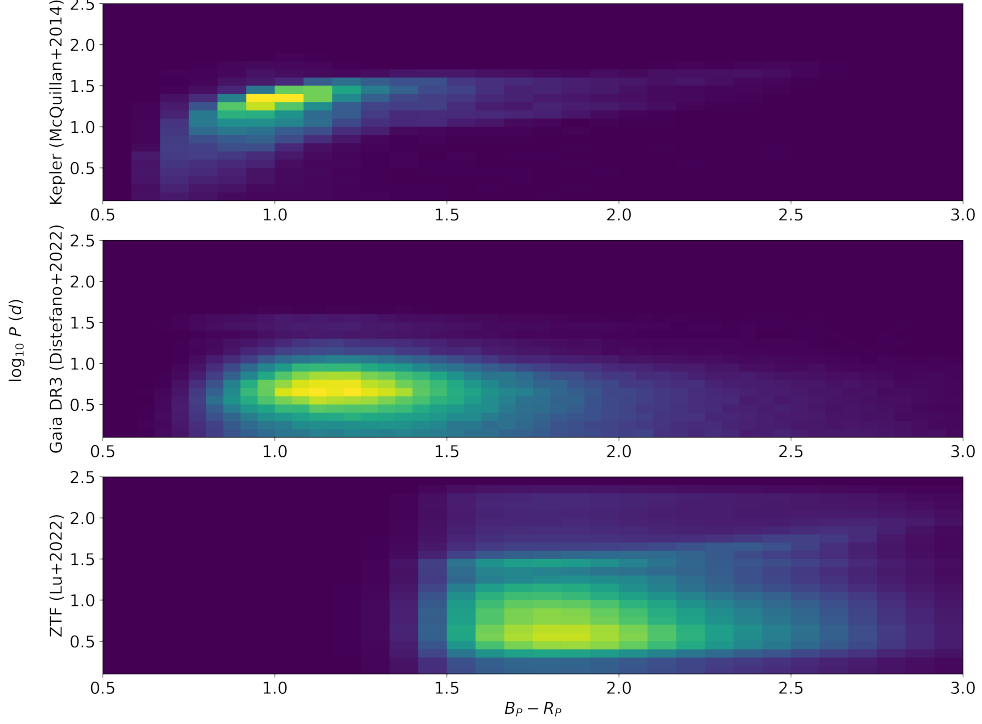


FIGURE 1.1: Normalised 2D histograms of the *Kepler* ([McQuillan et al., 2014](#)) (Top), *Gaia DR3* ([Distefano et al., 2022](#)) (Middle), and *Zwicky Transient Facility* (*ZTF*) ([Lu et al., 2022](#)) (Bottom) samples. Each sample probes a different area of the rotational period against colour space with some overlap. This expands our knowledge of the evolution of rotation to different types of stars while the agreement between these samples confirms their independent accuracy.

The stellar spot rotation periods that are obtained from each of these missions are suited to observe particular masses and rotation period regimes along the main sequence. This results from the underlying telescope parameters, the scanning technique employed, and each mission’s observation cadences ([Distefano et al., 2012](#)). Comparing the rotational period distributions in Figure 1.1 we observe a few notable features and limitations from each mission. The *Gaia DR3* rotation period sample exhibits spurious periods centred around 0.5, 18, 25, 32 and 49d. [Distefano et al. \(2022\)](#) suggest that the non-uniformity of the *Gaia* sampling could be the cause of these peaks. *Kepler* mainly targeted solar-like stars. As a result, in the *Kepler* sample, there is a lack of measured periods for M dwarfs and fast-rotating young stars. On the other hand, the *ZTF* and *Gaia* samples did not have this targeting bias. As a result, the *ZTF* and *Gaia* samples probe the rotation periods of the comparatively lower-mass (redder) stars. The *Gaia DR3* rotation sample

is, as a result of the Gaia scanning law, mostly suited to detect periods of rapidly rotating stars ($P < 5$ d). Due to the long observation baseline, the *ZTF* mission was more suited to observe longer rotation periods. Combining the results of these missions, we can accurately probe the evolution of rotation along the main sequence for a wider range of stellar parameters than the individual missions permit. Further, the cross-match of stars between these missions confirm whether the individual missions themselves provide accurate measures of the stellar surface rotation period.

Most of what we know about main-sequence rotational evolution arises from measuring stellar spot rotation periods. However, the technique is limited by the requirement for stars to express stellar spots to be effective - a limitation that is invoked several times to explain phenomena discussed later in this Section. [McQuillan et al. \(2014\)](#) attempted to measure the stellar spot rotation periods of solar-like stars in the *Kepler* sample. In this work, they recovered the rotation period of 20% of stars with long cadence observations - 34000 detected rotation periods out of 133000 selected stars in the sample. On the other hand, [Distefano et al. \(2022\)](#) places the efficiency of the Gaia DR3 period detection pipeline at 0.4%. They argue that the detection efficiency is non-constant and, in fact, a function of stellar magnitude, the amplitude of the rotational modulation, the stellar rotation period and the ecliptic latitude. There may be regions of evolution where the stellar spot rotation period does not effectively probe rotational evolution.

All matter in the universe has some angular momentum. Stars are born in the core of spinning molecular clouds from the infall of matter due to gravity. As a result, all stars are rotating. The amount of angular momentum a star is born with may depend on the cloud from which it was formed.

At the beginning of the pre-main-sequence (PMS) phase, a young star is typically surrounded by a disk of gas and dust from which it is accreting material. The accretion process can lead to an increase in the rotation rate of the star, as the angular momentum of the infalling material is transferred to the star. However, as the star grows in size and mass, its magnetic field becomes stronger, which can slow down its rotation through the process of magnetic braking.

One key feature of PMS rotational evolution is the "disk-locking" phenomenon, in which the star's rotation becomes locked to the rotation of the disk ([Eggenberger et al., 2012](#)). This occurs when the star's magnetic field is strong enough to interact with the disk,

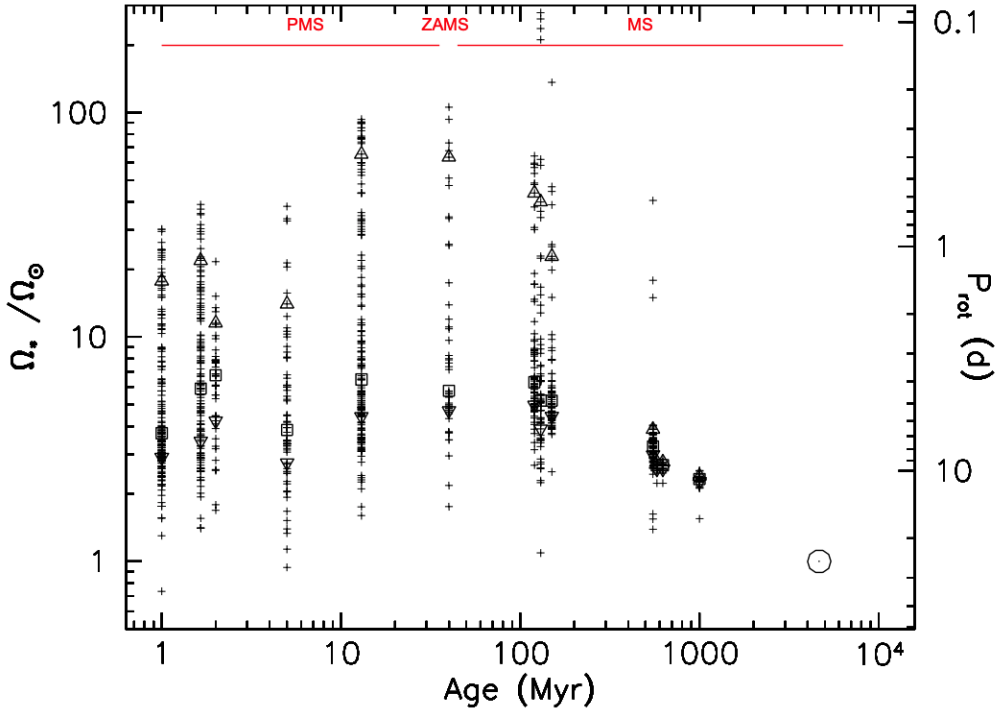


FIGURE 1.2: Angular rotation rate (relative to solar) distributions of low-mass young open clusters and the Sun. Triangles, inverted triangles, and squares represent the 90th, 25th, and median rotation rates of the cluster. Open circle denotes the present value of the rotation rate of the Sun. Median values indicate that the rotation rate of cluster is approximately constant with age, despite the spin up by accretion. In order of increasing age (left to right) the clusters are ONC (1 Myr) (Herbst et al., 2002), NGC 6530 (Henderson & Stassun, 2012), NGC 2264 (2 Myr) (Affer et al., 2013), NGC 2362 (5 Myr) (Irwin et al., 2008), h PER (13 Myr) (Moraux et al., 2013), NGC 2547 (40 Myr) (Irwin et al., 2008), Pleiades (120 Myr) (Hartman et al., 2010), M50 (130 Myr) (Irwin et al., 2009), M35 (150 Myr) (Meibom et al., 2009), M37 (550 Myr) (Hartman et al., 2009), Praesepe (578 Myr) (Delorme et al., 2011), Hyades (625 Myr) (Delorme et al., 2011), and NGC 6811 (1 Gyr) (Meibom et al., 2011). Sourced from Gallet & Bouvier (2013), Figure 1.

causing the star and disk to rotate together. Disk-locking can help to explain why some PMS stars have relatively long rotation periods, even though they are young and should be rotating rapidly due to the effects of accretion.

The interplay between accretion and magnetic braking can result in a complex evolution of the rotation rate of a young star during the PMS phase (Gallet & Bouvier, 2013). Observations of young stars in star-forming regions have revealed that the rotation rates of PMS stars span a wide range, with some stars spinning rapidly and others rotating slowly. We show this complex relationship in Figure 1.2. Comparative to the main-sequence where stars generally spin-down due to surface winds, the median rotation rate of PMS cluster is relatively constant with age.

While the many main-sequence stars have had their rotation rates measured, their ages are not well-constrained. Resultingly the evolution of rotation with age is also not well-constrained. Observations of young open clusters' main-sequence surface rotation from the *Kepler* mission suggest that angular momentum transport over a star's lifetime is consistent between clusters - the distribution of rotational periods of stars has considerable overlap between clusters (Spina et al., 2020; Curtis et al., 2020). Figure 1.3 shows the distribution of rotation rates of some open clusters. In this Figure, we can observe some significant aspects of the evolution of angular momentum in stars.

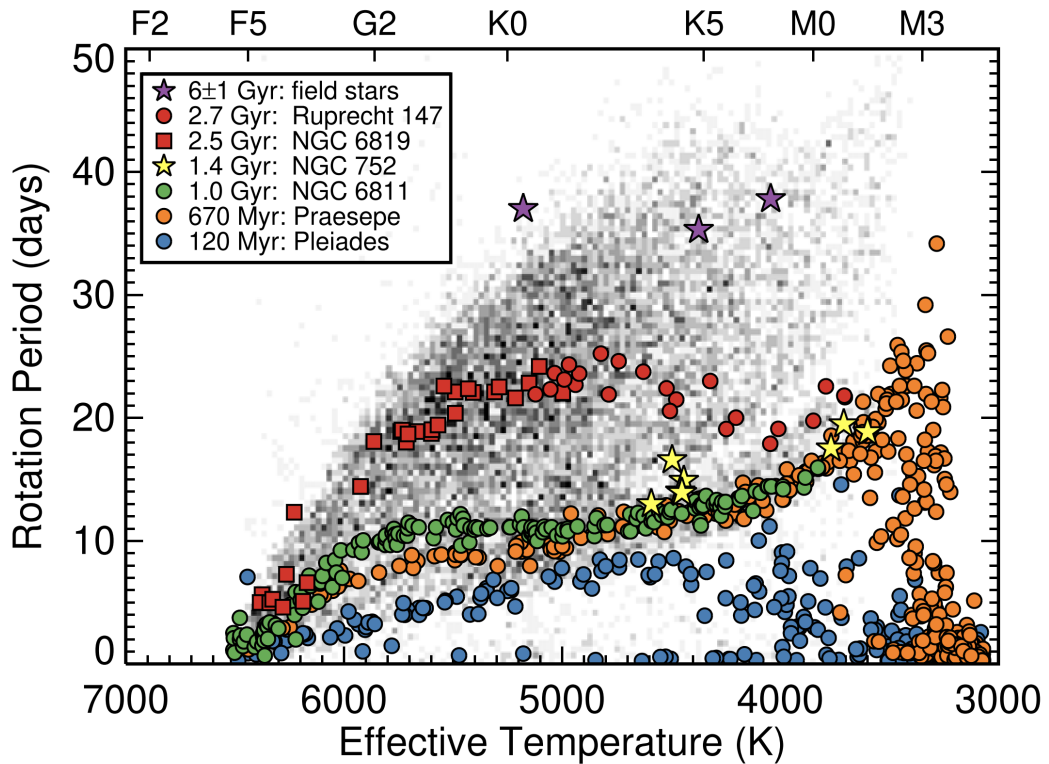


FIGURE 1.3: Scatter plot of various cluster rotational periods against effective temperature overlayed on the *Kepler* McQuillan et al. (2014) rotational period sample. The agreement between low mass Praesepe and NGC6811 periods implies mass dependent core-envelope coupling for young (<1 Gyr) stars. Sourced from Top left panel of Figure 7 in Curtis et al. (2020)

The surface rotational period increases over time for stars between $<1.1 M_{\odot}$. Within this range of masses, angular momentum is lost from the convective surface through mass loss and interactions of the star's magnetic field and the lost ionised material through stellar winds - magnetic braking. Through observations of the Pleiades, Ursa Major, and Hyades stars and the Sun, Skumanich (1972) derived the proportional relation between the rotational rate of stars and the inverse square of their age - $\omega(t) \propto t^{-1/2}$. This

proportionality forms the standard for expected rotational evolution and for what is known as gyrochronology - measuring the ages of stars from their rotational rate.

Outside the ~ 0.4 and $1.1 M_{\odot}$ range, the rotation period also decreases, albeit slower, with much more complex relationships with time. Above $\sim 1.1 M_{\odot}$, known as the Kraft break, stars have shallower convective envelopes and are believed to have less efficient magnetic dynamos - which induce strong magnetic fields. Resultingly, the magnetic braking in these stars is less efficient, and these stars continue to rotate rapidly throughout most of their main-sequence lifetimes. Below $0.4 M_{\odot}$ stars are fully convective. Angular momentum is efficiently transported throughout the star. A greater amount of angular momentum needs to be removed to slow the star's rotational rate, compared to stars that are not fully convective. The main-sequence rotational evolution of stars with mass $>1.3 M_{\odot}$ is unprobed. Above this mass, stars have no convective envelope, and thus, they do not express stellar spots nor solar-like oscillations that can be used to probe the surface rotation rate. Theoretical modelling of the rotational evolution of high-mass stars is a substantial area of research in which observations of stellar parameters such as chemical abundances must independently constrain angular momentum transport rather than observations of stellar rotation. As this work has a stronger focus on observing the rotation of stars, these results will not be discussed here. For more information, we suggest reviews of astrophysical models of high-mass stellar rotational evolution, e.g. [Heger \(1998\)](#); [Maeder & Meynet \(2000\)](#); [Maeder \(2009\)](#).

Until recently, it was assumed that there was little to no angular momentum transport between the radiative core and convective surface of main-sequence stars in the 0.4 - $1.1 M_{\odot}$ range. Helioseismic observations of the Sun suggest that only the stellar surface undergoes rotational braking, and the core remains rotating rapidly - suggesting minimal angular momentum transport between the core and the surface on the main sequence. However, open cluster rotation period observations suggest that Skaumanich-like rotational evolution alone does not explain the observed distributions of rotation periods with mass.

[Spada & Lanza \(2020\)](#) proposed that mass-dependent angular momentum transport between the core and the surface was required to explain observations of young (< 1 Gyr) open cluster rotation period distributions. In their work, they argue that clusters contain two sequences of stars: a sequence of relatively slower rotators, following the expected

coherent slowing of rotation rate following the Skaumanich relation, and a sequence of lower mass stars that appear to have a constant rotation rate between clusters of different ages. They compared the observations of the \sim 700-Myr old Praesepe and the 1-Gyr old NGC 6811 clusters. Figure 1 in [Spada & Lanzafame \(2020\)](#) compares the rotation period distribution of the Pleiades (120 Myr), Praesepe (670 Myr), and NGC 6811 (1 Gyr). Comparing observed rotation periods, they find that higher mass stars ($> 1 M_{\odot}$) that are on the slow rotator sequence of the older NGC 6811 have longer periods than their counterparts in the younger Praesepe, as Skaumanich rotational evolution suggests. On the other hand, the two clusters' rotational periods are indistinguishable at lower masses ($< 0.8 M_{\odot}$). In other words, low-mass stars have not been spinning down at all in the intervening 300 Myr. They argue that behaviour manifests mass-dependent core-envelope coupling - angular momentum transport between the core and the surface - briefly compensating for the loss of angular momentum due to wind braking at the surface. They develop a semi-analytical model of the rotational period's evolution with a star's age and mass tuned with the observations of stellar cluster rotational period distributions. This notably improves the accuracy of gyrochronology compared to the Skaumanich relation, especially for younger low-mass stars.

On the other hand the slow spin down rates of fast rotating stars could be related to saturation of the angular momentum loss due to stellar winds for fast rotating stars ([Johnstone et al., 2015a,b](#); [Gallet & Bouvier, 2013](#)). This is motivated by the saturation of magnetic field indicators for fast rotation rates - or rather low Rossby numbers ([Wright et al., 2011](#)). This could explain the slower observed spin-down of young rapidly rotating stars. Both of these prescriptions neglect each other: ([Spada & Lanzafame, 2020](#)) includes a simple stellar wind prescription that does not consider the saturated regime, while ([Gallet & Bouvier, 2013](#)) does not consider mass dependent angular momentum transport within the star.

Another phenomenon not well explained by Skaumanich-like rotational evolution is the observed intermediate period gap. [McQuillan et al. \(2014\)](#) calculated the rotation periods of 30000 stars in the *Kepler* sample from photometric oscillations of surface brightness from stellar spots. The distribution of the log of the rotational periods from this sample against their colour is shown in Figure 1.4. Following increasing rotation period as a proxy for time, this Figure highlights the overabundance of observations

followed, temporally, by a dearth of observations of particular rotational periods - the position of which varies with mass.

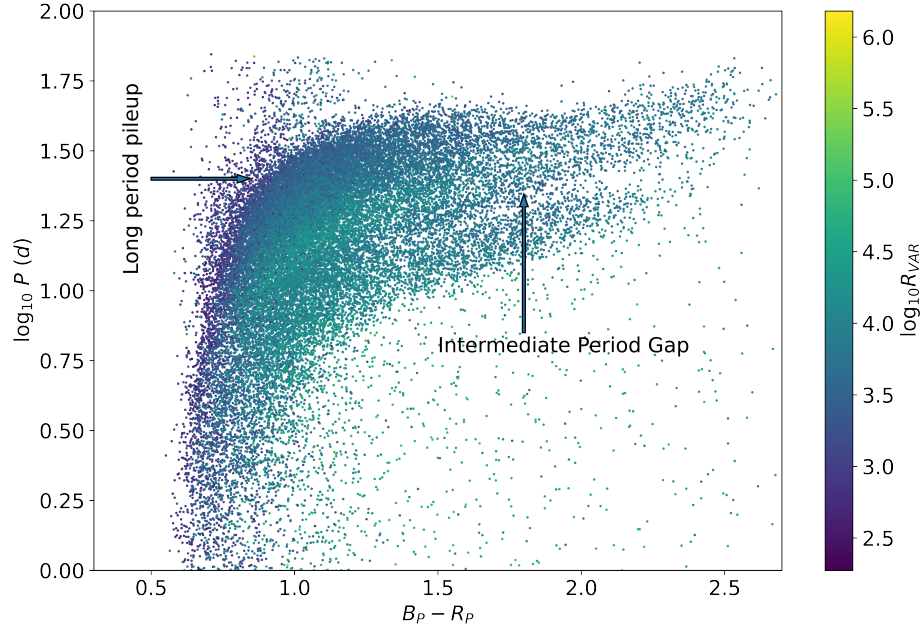


FIGURE 1.4: Scatter plot $Gaia B_P - R_P$ colour against log of the rotational period of the *Kepler* [McQuillan et al. \(2014\)](#) rotational period sample coloured by the log of the photometric variation (R_{var}). R_{var} decreased towards the gap from above and below, suggesting the intermediate period gap is representative of a minimum of observability of rotation period. Highlighted by arrows in this Figure are two features that we discuss in more detail in this Section: the intermediate period gap and the long-period pile-up.

Since identifying the gap, several explanations have been presented for this phenomenon. [McQuillan et al. \(2014\)](#); [Davenport \(2017\)](#) first proposed that rather than the gap being the result of modified angular momentum transport, the gap is the artifact of a recent period of bursty star formation in the *Kepler* field - resulting in a young (< 50 Myr), fast rotating, population and older, background slowly rotating, population. [Davenport \(2017\)](#) further find that the fast and slow rotators in his sample also exhibit a different distribution of the proper motion. Two kinematically separate groups favour the explanation of two epochs of star formation in the *Kepler* field. This explanation is further supported by the work of [Davenport & Covey \(2018\)](#), who showed that the gap appears to correlate with Galactic height, which is assumed to be related to stellar age.

The recent bursty star formation hypothesis accounts for the overpopulation of observations below the gap. In contrast, the dearth of observations represents the background

observation rate of rotational periods within this period range. [Gordon et al. \(2021\)](#) provided evidence against this hypothesis through analysis of *K2* data. They found that the intermediate period gap is present in the multiple pointings of the *K2* mission - suggesting that recent bursty star formation is isotropic - and that clusters with different ages contain stars that have crossed the gap.

The former suggests that all clusters universally went through a period of bursty star formation \sim 50 Myr ago. [Angus et al. \(2020\)](#) observed that the velocity dispersions of stars increase smoothly across the gap. Given that the two populations - above and below the gap - do not substantially differ in other spectroscopic and photometric observations, this scenario remains theoretically possible but unlikely. The latter requires slightly more thought. Comparing Figures 1.3 and of 1.4, the gap has a sharper slope than the sequences associated with constant age populations from Praesepe ([Douglas et al., 2017, 2019](#)), NGC 6811 ([Curtis et al., 2019](#)) and Ruprecht 147 ([Curtis et al., 2020](#)). If the bimodal star formation scenario explained the gap, the gap should have the same shape and position for each cluster and the entire *K2/Kepler* sample.

Before exploring possible explanations for the intermediate period gap, it is worth identifying where the rotational period gap occurs in the stars' evolution. [Reinhold et al. \(2019\)](#) first suggested that the gap aligns with a rotational isochrone at \sim 800Myr. With [Spada et al. \(2016\)](#) modifications to Skaumanich spin down for low-mass star to reflect the rotational distribution of clusters of known age, updated the proposed age to 750 Myr ([Reinhold et al., 2019](#)). Contrary to the hypothesis that the gap aligns itself with a certain isochrone, [Curtis et al. \(2020\)](#) identified that the open cluster Ruprecht 147 contains stars above and below the gap - as well as one star that appeared to be within the gap. This suggests that the gap does not align itself with a particular age. Instead, they argued that the gap aligns itself with a line of constant Rossby number¹⁰ = 0.5. The Rossby number is associated with the magnetic dynamo, e.g. [Noyes et al. \(1984\)](#); [Montesinos et al. \(2001\)](#); [Augustson et al. \(2019\)](#). To simplify, a star can be thought of as a volume of charged particles. As a star rotates, so do the charged particles within it. Moving charged particles induce a magnetic field - creating a magnetic dynamo. As the star rotationally evolves, so does the magnetic dynamo.

¹⁰Defined as the ratio of the rotational period to the convective turnover timescale ($Ro = P_{rot}/\tau_{conv}$) - which itself is dependent on mass and is approximately constant for a star's main-sequence lifetime

Given that the gap appears to line up with a line of constant Rossby number, this may suggest that the gap is instead caused by an event in the evolution of the magnetic dynamo rather than an event in time. This is a notable result because the magnetic dynamo is associated with a number of stellar phenomena - such as magnetorotational instabilities (angular momentum transport processes associated with the magnetic field) or stellar spots.

Other prospective hypotheses for the intermediate period gap can be broken down into two categories: (1) modified angular momentum transport and (2) decreased observability of rotation periods.

Let us consider the first hypothesis: the gap results from modifications to angular momentum transport. [Lu et al. \(2022\)](#) have shown that the gap is most apparent for stars less massive than $1.3 M_{\odot}$ and more massive than $0.4 M_{\odot}$. If we look closely at Figure 1.5 we can see that for the ZTF sample (black dots) the intermediate period gap is most apparent for stars $1.5 < B_P - R_P < 2.5$ and closes for low mass ($B_P - R_P > 2.5$) stars. Stars redder than $B_P - R_P > 2.5$ are fully convective ([Amard et al., 2019](#)), suggesting that the gap may be another phenomenon related to the interplay between angular momentum transport between the radiative core and convective surface and surface rotational braking along the main sequence.

[McQuillan et al. \(2014\)](#) first proposed that the gap is the result of two variations to Skaumanich rotational evolution. First, stars below the gap undergo a period of stalled spindown, resulting in the observed overdensity of stars along the lower branch, followed by a period of accelerated spindown, resulting in the dearth of stars in the gap¹¹.

The proposed mechanism underlying this scenario is the mass-dependent decoupling and recoupling of the core and the envelope proposed in [Lanzafame & Spada \(2015\)](#) and [Spada & Lanzafame \(2020\)](#), discussed earlier in this work. [Angus et al. \(2020\)](#) suggest that the core envelope decoupling and recoupling may explain the period gap as a break between a "younger" pile-up regime ($\text{Ro} < 0.6$) in which surface rotation periods are relatively constant with time from core-surface angular momentum transport and increase with decreasing mass from an "older" ($\text{Ro} > 0.6$) regime with the gap representing a period of relatively fast spin evolution during the transition between the two. Proponents

¹¹The authors disfavoured the hypothesis favouring the bimodal star formation hypothesis discussed earlier in this work.

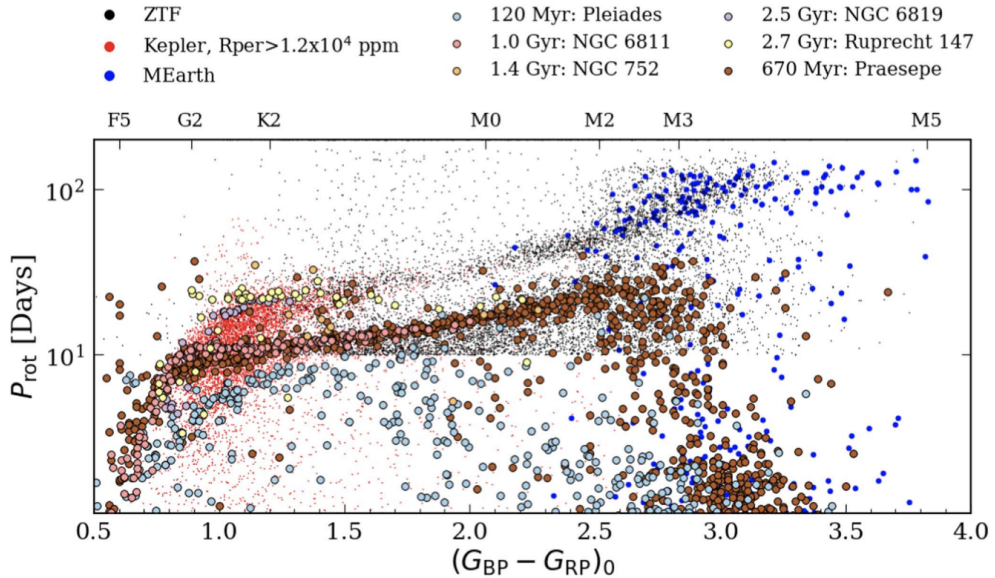


FIGURE 1.5: Rotation period against $Gaia B_P - R_P$ from *Kepler*, *ZTF* overlayed with various open cluster measurements. Highlighted by this Figure is the disappearance of the intermediate period gap above $B_P - R_P = 2.5$ - the fully convective star boundary. This suggests that the rotational period gap is related to the coupling of the core and surface of low mass stars ($0.4 M_{\odot} < M < 1.3 M_{\odot}$). Sourced from the top panel of Figure 8 in (Lu et al., 2022).

of this hypothesis suggest that the gap results from a period of enhanced spindown following core and surface recoupling where stars "jump" the gap before resuming Skumanich spindown, as is observed for older clusters. Models of - and physical mechanisms underlying - rotational evolution that reflect the proposed rapid spindown are yet to be identified. Under this model, the gap reflects an under the density of stars but would not be empty. There should be a small number of stars with $Ro \approx 0.6$, irrespective of our ability to measure their rotational periods. Curtis et al. (2020) found five Ruprecht 147 stars in or just beneath the gap yet to be thoroughly investigated.

Now let us discuss the second hypothesis: the gap results from a lack of observations of rotational periods. The rotational period of *Kepler* stars requires that stars express photometric oscillations from stellar spots. Starspots are regions of intense magnetic activity on a star's surface from magnetic flux tubes in the convection zone. These flux tubes are thought to be stretched and curled by the differential rotation of the convective region. As a result, convection is inhibited, limiting plasma flow to the surface in these tubes. This results in lower-temperature material within the tube, which looks like a darker spot on the star's surface. Stellar spots have bright perimeters surrounding the cooler internal regions of spots, known as faculae.

Stellar spots can both increase or decrease stars' bolometric luminosity. Reinhold & Reiners (2013) and Reinhold et al. (2019) propose that the gap represents the transition in stellar spot structure from spot to faculae dominance in the photosphere. Following their explanation, the gap corresponds to a transition where the increase in bolometric luminosity from the faculae negates the decrease from the internal, cooler region of the stellar spots. In the McQuillan et al. (2014) sample, stellar rotational periods are measured from the period of brightness variability due to the brightness variability introduced by stellar spots¹². Suppose the bolometric flux does not vary due to stellar spots in the gap region. In that case, the amplitude of periodic variability would decrease within this region. Reinhold et al. (2019) suggests that the gap is full of stars and represents a minimum in the detectability of rotation periods.

Supporting this hypothesis, in both the *Kepler* and *K2* fields, the variability amplitude (R_{var}) decreases towards the gap from both lower and higher rotational periods. This can be seen in Figure 1.4, which is coloured by the log of R_{var} . On the other hand, while there is evidence that stars undergo spot-to-faculae dominance, e.g. the Vaughan-Preston gap (Vaughan & Preston, 1980), this occurs much later in a star's lifetime at $Ro \sim 1$. Further, there is evidence that stars above and below the gap are both spot-dominated (Lockwood et al., 2007; Reinhold et al., 2019). Reinhold et al. (2019) speculate that activity cycles that vary the spot-to-faculae brightness contributions on rotational timescales could be the process underlying the rotational period gap. As of writing, there is no evidence to support this hypothesis.

Recent works have attempted to identify the fractional spot coverage of cluster members from their spectra (Cao & Pinsonneault, 2022). They do this by assuming the spectra of stars can be broken down into spot and ambient components that vary in temperature but are consistent in other stellar parameters. They find that the fractional spot coverage of stars is related to the Rossby number. Within this work, they observe a population of spot-coverage-enhanced stars that deviate from the relations they present.

In a follow-up work (Cao et al., 2023) they combine the angular momentum transport and decreased observation hypothesis by proposing that star spot measurements in the Praesepe open cluster are strongly enhanced only for stars that depart Skumanich rotational evolution. They suggest that a decoupling of the core and the surface explain

¹²this technique is discussed in more detail in Section ??

both observations. In their model, angular momentum transport between the core and the surface slows the increase of the rotational period. The resultant shears enhance the magnetic dynamo and, thus, stellar spot activity. Stars enhanced in stellar spot coverage are expected to have decreased observed effective temperatures. Spot-dominated, as opposed to faculae-dominated, stellar spots are cooler than the ambient temperature of the star. As a result, stars with enhanced stellar spot coverage have a decreased observed effective temperature. They then speculate that the rotational period gap is thus the result of a bias in observed effective temperature rather than a lack of observations of the rotational periods of stars in the gap.

Observations of open cluster rotational distributions beyond the gap suggest that stars $< 1M_{\odot}$ that have crossed the gap ($\text{Ro} > 0.6$) continue to spin down and follow the Skumanich-like rotational evolution until they leave the main sequence. On the other hand, there is an apparent overabundance of stars at critical rotation periods (dependent on their mass). Above this is a lack of observations of rotation periods for stars $> 5500\text{K}$. Stars with higher masses also appear to have lower rotation periods on the pile-up than their less massive counterparts. This results in what is known as the long-period pile-up, as noted in Figure 1.4. The long-period pile-up aligns itself in the [McQuillan et al. \(2014\)](#) period distribution with Rossby number ($\text{Ro} = 2.08$) ([van Saders et al., 2019](#)).

[van Saders et al. \(2019\)](#) suggest that the long-period pile-up could result from decreased magnetic braking or a lack of observations of stars beyond this Rossby number. Under the former scenario, stars stop spinning down when they reach this Rossby number as a result of weakened magnetic braking. This results in the overdensity of stars and a lack of observations of larger rotational periods. In the latter, they propose that the error in observed periods can smooth out the overdensity of stars and, in fact the lack of rotational periods is because of variations to the stellar spot activity (See above discussion of speculative explanations for decreased observation of rotational periods within the rotational period gap). Further supporting this explanation [David et al. \(2022\)](#) found that photometric variability decreases above the gap. Suggesting an unobserved population of stars with longer rotation periods.

Under the weakened magnetic braking model [David et al. \(2022\)](#) suggest that stars in this temperature regime $1M_{\odot} < M < 1.3M_{\odot}$ may spend half of their main-sequence lifetimes at the long period pile-up with only modest variances to their rotational period.

Below this mass regime, stars appear to continue to lose angular momentum through wind braking following the Skumanich relation. This results in stars with large rotational periods when they enter the post-main-sequence.

1.2.2 Post-main-sequence

For low mass ($1.1 - 1.5 M_{\odot}$) stars during the post-main-sequence, the information provided to angular momentum transport by each star can be greater than during the main sequence. While surface rotation rate can still be measured through stellar spot photometric oscillations, within this regime, the core and surface can also be simultaneously constrained through asteroseismology (at different points in evolution). This results from a combination of the expression of mixed modes, shorter mode lifetimes, and increased core rotation rates. During the main sequence, g-modes are trapped within the radiative core and thus do not introduce brightness variations (oscillations) to the stellar surface. Some g-modes can couple with p-modes in the surface convective cavity during the post-main-sequence and are known as "mixed modes". The rotational splittings of the mixed modes allow us to infer the rotation rate in the radiative region and deep core. ([Metcalfe et al., 2010](#); [Bedding et al., 2011](#)) Where, precisely, the mixed modes probe is dependent on where in the post-main-sequence the star is observed. For example, sub-giant stars express p-modes and mixed modes that can probe both the core and the surface, whereas red giant branch (RGB) stars mainly express mixed modes that can only probe the star's core. While stellar spot surface rotation periods can be measured for post-main-sequence stars [McQuillan et al. \(2014\)](#); [Ceillier et al. \(2017\)](#), asteroseismic inference of core and surface rates is the standard for probing rotation evolution in this evolutionary regime ([Deheuvels et al., 2014](#); [Gehan et al., 2018](#); [Deheuvels et al., 2020](#); [Fellay et al., 2021](#)).

Measuring the core and surface rotation rates simultaneously provides much more information to angular momentum transport than either of these quantities alone. For example, during the main-sequence, the over-abundance of stars along the lower branch of the Kepler rotation period gap could simultaneously be explained by diminished wind braking for the surface or by core-envelope recoupling. Measuring the core rotation rates would break this degeneracy. This asteroseismic quirk is useful as it allows us to directly investigate angular momentum transport more efficiently.

However, the constraints to the rotation profile of stars by asteroseismology, even in the post-main sequence, are limited. Indeed the core and surface rotation rates of subgiants can simultaneously be probed. However, where in a star the rotation can be probed depends on the observed oscillation modes, which depend on the stellar structure. The rotation rates obtained by asteroseismology are kernel-based averages of the rotation profile in regions that the observed oscillation modes probe. For example, subgiants' core and surface rotation rates are the kernel-based average rotation rates of the innermost $r/R \leq 0.05$ and outermost $r/R > 0.9$ regions (on average). Between these regions, the rotation profile is not constrained. As a result, the shape of the rotation profile, which can be fingerprints of specific angular momentum transport mechanisms at play, is also not constrained.

Asteroseismic inference of rotation rates can also be imprecise. This can be seen when comparing the surface rotation periods from asteroseismology and stellar spot photometric oscillations in [Hall et al. \(2021\)](#). This is because: a) state-of-the-art measurements of rotational splittings - the quantity that constrains the rotation profile - are low SNR and are often also imprecise, and b) the observed rotational splittings are a finite subset of the infinite number of rotational splittings that would be required to accurately and precisely constrain the entire rotation profile. With these limitations in mind, we now discuss the observed evolution of rotation of post-main-sequence stars.

Following the main-sequence, low-mass stellar rotation varies with the evolutionary phase. Models of rotating stellar evolution (e.g. [Maeder & Meynet, 2000](#); [Heger et al., 2000](#)) predict the following qualitative evolutionary pathway. Towards the end of the main sequence the rotation profile is largely flat. Assuming conservation of angular momentum as hydrogen core burning stops, pressure in the core drops, resulting in core contraction while the convective surface region expands. Resultingly the core is spun-up while the surface is spun-down. The core should continue to spin down as the core contracts along the RGB until entering the red clump (low-mass core He burning). The core burning reintroduces core pressure, and the resulting expansion of the core decreases the core rotation rate. When core He burning ceases, the core pressure drops again, resulting in a spun-up white dwarf (relative to the core rotation rate of red clump stars). We highlight the qualitative rotation evolution of post-main-sequence stars in Figure 1.6. Observations suggest that low-mass stars follow this pathway ([Mosser et al.,](#)

2012; Deheuvels et al., 2014, 2015; Hermes et al., 2017; Gehan et al., 2018; Deheuvels et al., 2020).

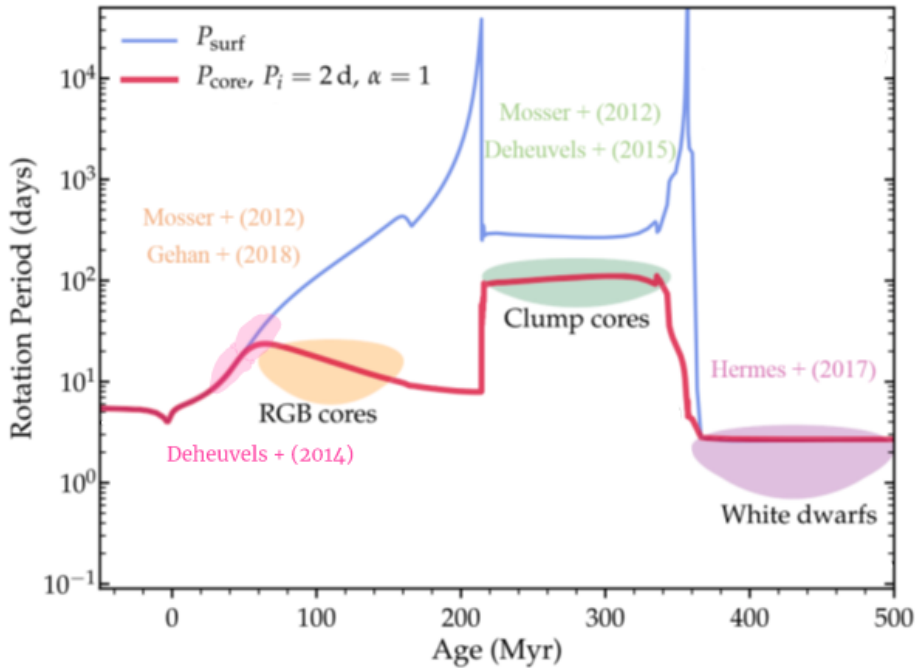


FIGURE 1.6: Core (red) and surface (blue) rotation rates with additional angular momentum transport following the prescription of Spada et al. (2016). Coloured sections denote evolutionary milestones and the works that have provided constraints to these milestones. **Pink:** subgiant core and surface rotation, **Orange:** red giant branch cores, **Green:** clump core rotation rates, and **Purple:** white dwarf rotation rates. Adapted from Figure 3 in Fuller et al. (2019)

Measuring the core and the surface rotation rates of post-main-sequence stars allows us to place constraints on the radial differential rotation of stellar interiors and quantitatively probe the evolution of angular momentum transport. Observations of young subgiants suggest that terminal age main sequence stars' rotation profiles are relatively flat (Deheuvels et al., 2020). However, observations of older post-main-sequence stars have raised more questions than they have answered (Beck et al., 2012). To summarise: angular momentum transport during the post-main-sequence must be greater than state-of-the-art models currently predict.

Deheuvels et al. (2014) measured the core and surface rotation rates of 6 subgiants/young red giants. The observed core to surface rotation ratio of subgiants and the core rotation rates of red giant branch stars suggest that additional angular momentum transport is unaccounted for in state-of-the-art models of rotating stellar evolution (Deheuvels et al., 2014; Spada et al., 2016; Moyano et al., 2022). The scale of the core-to-surface rotation

rate ratio of subgiants (Ω_c/Ω_s) is one to two orders of magnitude smaller than models predict (Fuller et al., 2015; Spada et al., 2016; Ouazzani et al., 2018; Eggenberger et al., 2019). While core rotation rates were first believed to decrease along the red giant branch¹³ (Mosser et al., 2012) revised measurements and a larger sample size revealed that the core rotation rates of red giant branch stars appear constant with evolution when the contraction of the core should spin them up. (Mosser et al., 2012; Gehan et al., 2018; Moyano et al., 2022). The core rotation rates of early red giant branch and red clump stars suggest a continued excess angular momentum transport during this phase of evolution (Cantiello et al., 2014; Moyano et al., 2022). On the other hand, observed white dwarf rotation rates can be recovered from the observed core rotation of clump stars assuming conservation of angular momentum. (Cantiello et al., 2014; den Hartogh et al., 2019) Cantiello et al. (2014) suggests that this feature may be owing to the short evolutionary timescale between the red clump and white dwarf phases rather than indicative of a decrease in the excess angular momentum transport.

The physical mechanism underlying the excess angular momentum transport is currently unidentified. Several notable relations with mass and evolutionary state have been determined by calculating the excess angular momentum transport required to match observations. Spada et al. (2016) quantified the increased angular momentum transport required to match the observed subgiant core and surface rotation rates measured in Deheuvels et al. (2014). They introduced an additive angular momentum diffusion coefficient to the transport of angular momentum equation in the radiative zone, which obeys an advection-diffusion equation:

$$\rho \frac{d}{dt} (r^2 \Omega(r)) = \frac{1}{5r^2} \frac{\partial}{\partial r} (\rho r^4 \Omega(r) U(r)) + \frac{1}{r^2} \frac{\partial}{\partial r} \left(\rho (D_{\text{shear}} + v_{\text{add}}) r^4 \frac{\partial \Omega(r)}{\partial r} \right), \quad (1.1)$$

(Zahn, 1992; Maeder & Zahn, 1998; Eggenberger et al., 2008) where r and ρ are the characteristic radius and density on an isobar. $\Omega(r)$ is the mean rotational rate and $U(r)$ is the velocity of meridional currents in the radial direction. D_{shear} is the diffusion coefficient for the angular momentum shear instability (See Equation 10 in Eggenberger et al. (2010)) and v_{add} is the additional viscosity corresponding to the excess angular momentum transport. Their results suggest that the additional angular momentum

¹³Indeed when core rotation rates of red giants are plotted against $\log g$, a proxy for evolution, they do appear to decrease with evolution. When plotted against the more appropriate scale of mixed mode coupling (See Equation 10 in Gehan et al. (2018) and compare Figures 12 and 13 in this work), they are constant with evolution.

transport decreases as stars ascend the subgiant branch and increases with mass. The suggested scale of excess angular momentum transport they propose is on the order of $10^3 - 10^4 \text{ cm}^2 \text{s}^{-1}$. Which is similar to D_{shear} close to the convective envelope but rapidly decreases to the order of $10^1 \text{ cm}^2 \text{s}^{-1}$ in the stellar core. Comparing Figures 1.7 and 1.8 we see that the introduction of the additional viscosity to the model term results agreement with the core to surface rotation fraction in the [Deheuvels et al. \(2014\)](#) sample.

[Moyano et al. \(2022\)](#) performed a similar analysis but with the core rotation rates of red giant branch and red clump stars measured in ([Mosser et al., 2012](#)) and [Gehan et al. \(2018\)](#). They found that the same order of magnitude additional viscosity term was required to explain the approximately constant core rotation rates of red giant and red clump stars. Qualitatively they found that the additional angular momentum transport becomes stronger when the star evolves up the red giant branch through shell hydrogen burning. Angular momentum must be redistributed between two to three orders of magnitude more efficiently for red clump stars than for red giants closer to the main-sequence turn-off consistent with [den Hartogh et al. \(2019\)](#). Figures 1.9 and 1.8 highlight that models of red-giant evolution with the additional viscosity introduced in this work now agree with the observed core rotation rates observed in [Gehan et al. \(2018\)](#).

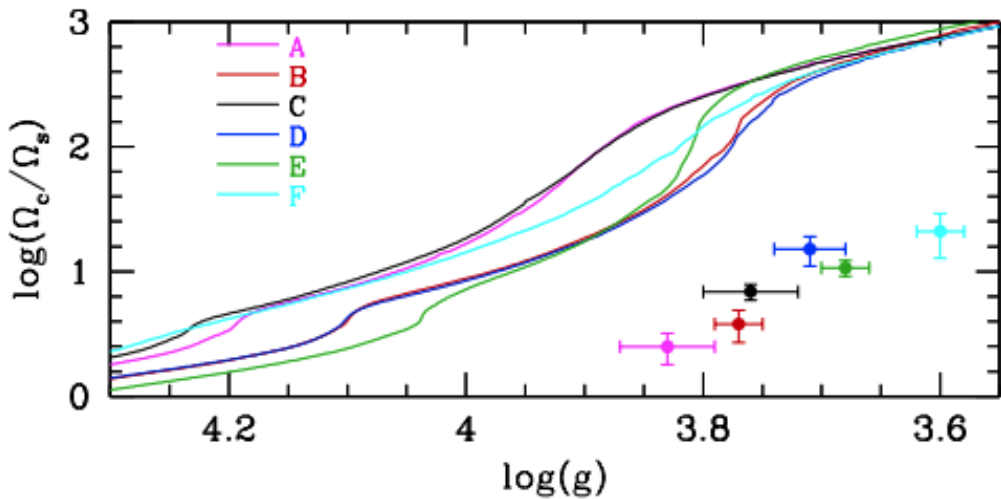


FIGURE 1.7: log of core to surface rotation rate against $\log g$. **Dots:** Observed core to surface rotation rates of the six subgiants measured in the [Deheuvels et al. \(2014\)](#) sample (A,B,C,D,E,F). **Lines:** rotating models of the stars in that sample without additional angular momentum transport ([Eggenberger et al., 2019](#)). The observed core-to-surface rotation rates are much smaller than models predict. This implies additional angular momentum transport than is currently accounted for models. Sourced from Figure 2 in ([Eggenberger et al., 2019](#)).

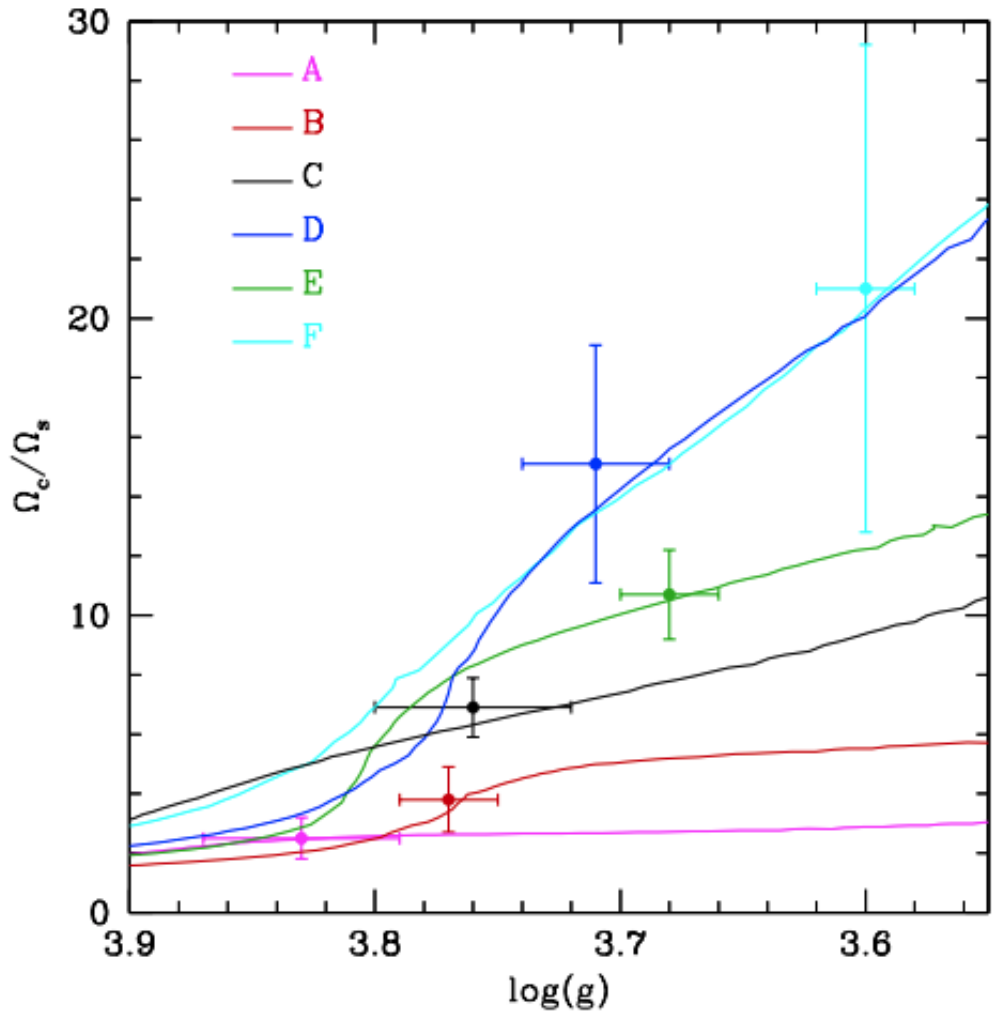


FIGURE 1.8: Same as Figure 1.7 but with additional angular momentum transport introduced for the models to reflect the observations. Sourced from Figure 3 in ([Eggenberger et al., 2019](#)).

Several modes of excess angular momentum transport have been suggested to explain the disparity between models and observations. [Barker et al. \(2019, 2020\)](#) studied the role of the Goldreich-Schuber-Fricke (GSF) instability (([Goldreich & Schubert, 1967](#); [Fricke, 1967](#)) and its role in angular momentum transport for post-main-sequence stars. They suggest that the GSF instability can introduce additional viscosity up to $10^4 \text{ cm}^2 \text{s}^{-1}$ for low-mass stars but is two orders of magnitude too small to reflect the rotation of higher mass stars not discussed in this work.

Magnetorotational instabilities constitute another candidate to explain the internal rotation of evolved stars. Two potential candidates are azimuthal magnetic rotational instabilities (AMRI) ([Ruediger et al., 2014](#); [Rüdiger et al., 2015](#)) and the Tayler-Spruit

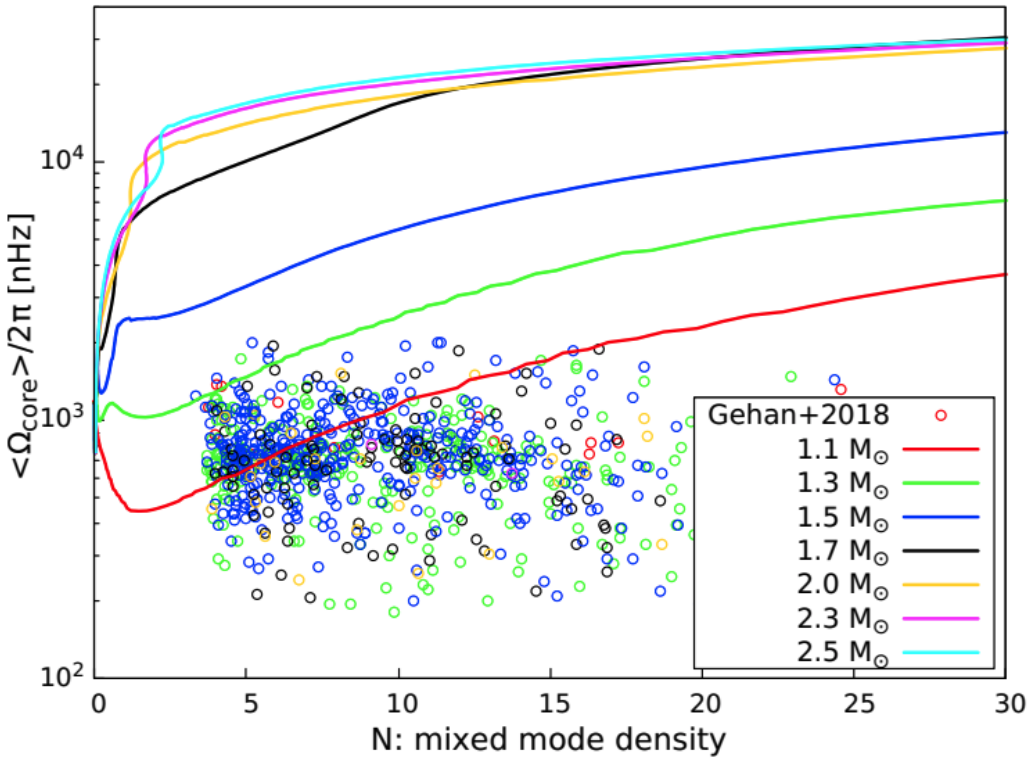


FIGURE 1.9: Average core rotation rates of red giants against mixed mode density (a proxy for evolution) **Dots:** Observed core rotation rates from Gehan et al. (2018) **Lines:** rotating models of the stars in that sample without additional angular momentum transport (Moyano et al., 2022). The observed core rates are much smaller than models predict. Implying excess angular momentum transport is required for the models to reflect the observations. Sourced from Figure 6 in (Moyano et al., 2022).

instability (Spruit, 2002) (See Section 1.3.3). Rüdiger et al. (2015) suggest AMRIs can increase molecular viscosity to the magnitude required to explain observations. On the other hand, there is no evidence to suggest that this instability reflects the trends with mass and evolution. The Tayler instability does introduce excess angular momentum transport in the post-main-sequence (Fuller et al., 2019), however, it cannot simultaneously reflect the observations of both subgiants and red giants (Eggenberger et al., 2019; den Hartogh et al., 2019).

Spada et al. (2016) propose the efficiency of angular momentum transport may be related to the core to surface rotation rate to some power - $(\Omega_c/\Omega_s)^\alpha$ - which can be related to magnetorotational instabilities. This work suggests that $\alpha = 3$ reflects the core rotation rates of red giants claimed in (Mosser et al., 2012). Moyano et al. (2022) revisited this prescription and found that $\alpha = 3$ more accurately reflects the approximately constant rotation core rotation rates of red giants observed by Gehan et al. (2018). Spada

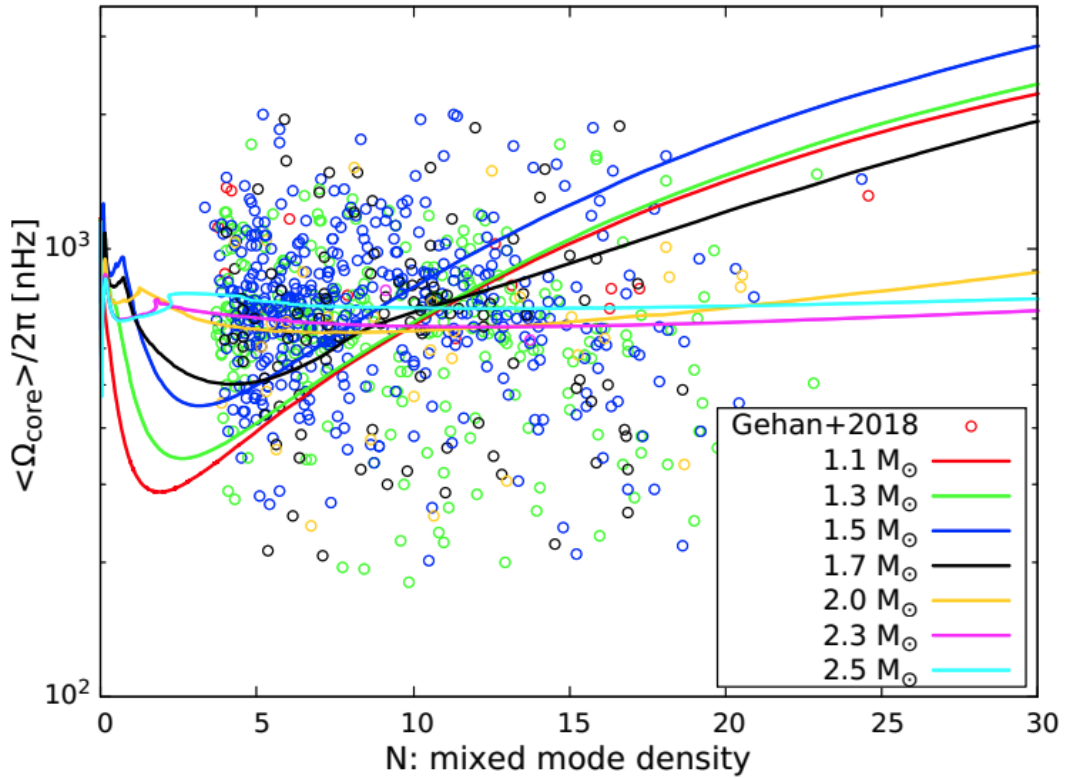


FIGURE 1.10: Same as Figure 1.9 but with additional angular momentum transport introduced for the models to reflect the observations. Sourced from Figure 7 in (Moyano et al., 2022).

et al. (2016) was limited to a single model with mass = $1.25 M_\odot$. No parameterisation with mass was therefore performed.

Other physical mechanisms have been suggested to have a role in excess angular momentum transport, such as angular momentum transport by internal gravity waves (Pinçon et al., 2017) or mixed-modes (Belkacem et al., 2015). However, the scale of their introduced additional viscosity is yet to be investigated. Disentangling each of these proposed mechanisms' relative importance to the additional angular momentum transport required to explain the observations requires much more data.

We speculate that the simultaneous measurement of subgiants' core and surface rotation rates may be the best probes for constraining the excess angular momentum transport. A few pathways exist to further probe the mechanism underlying excess angular momentum transport through asteroseismology alone. Either: a) more stars need to have their core and surface rotation rates measured through asteroseismology (which we will denote ensemble fitting), or b) stronger constraints must be placed on the rotation profile

between the core and the surface (single star constraints).

On the former, if more stars have their core and surface rotation rates observed, then more measurements of the excess angular momentum transport required for state-of-the-art models to match the observations are made. The excess angular momentum transport required to match observations appears mass and evolutionary-dependent. Stronger constraints to the dependency of the excess angular momentum transport on these quantities provide information about the underlying mechanism. The Kepler asteroseismic data currently available suggests that the efficiency of the excess angular momentum transport increases with the star's mass (Eggenberger et al., 2019). However, the efficiency of angular momentum transport decreases with evolution during the subgiant phase. Consequently, a transport process with efficiency dependent on the angular momentum gradient between the core and the surface cannot be at play in subgiants. Identifying with more precision the dependency of excess angular momentum transport on stellar quantities would provide evidence for or discredit proposed mechanisms.

On the latter, the internal shape of the rotation profile of subgiants reflects the underlying mechanism that created it. Therefore, evidence for or against particular shape of rotation profiles is illuminating to proposed mechanisms. A strong gradient in the rotation profile in the core of a subgiant, for example, is incompatible with angular momentum transport through deep fossil magnetic fields (Gough & Thompson, 1990) as they would likely smooth out sharp features. This is because differential rotation is expected to be damped along poloidal field lines (Garaud, 2002; Strugarek et al., 2011). Internal gravity waves, on the other hand, are expected to be efficient during the advanced phases of stellar evolution (Charbonnel & Talon, 2008). Internal gravity waves can give birth to localised weak gradients in the rotation profile as a result of extraction and deposit of angular momentum (Charbonnel & Talon, 2005). A sharp rotational gradient could also potentially trigger magneto-rotational instabilities that would transport angular momentum (Balbus & Hawley, 1994; Arlt et al., 2003; Menou & Mer, 2006; Fuller et al., 2015, 2019; Moyano et al., 2022). Evidence of a strong angular momentum gradient towards the core of a sub-giants quickly constrains the number of possible angular momentum transport mechanisms to solve the angular momentum transport problem.

Two obvious problems impede the single-star pathway. These are the need for observations of high SNR higher degree modes and the results of methods used to measure rotation profiles being unstable to high-resolution inversions. Constraints on the rotation profile in intermediate points between the core and surface require the observations of oscillation modes of $l \approx 10$ ([Ahlborn et al., 2020](#)). For reliable measurements of such oscillations, much longer observation periods, longer than *CoRoT* and *Kepler*, of sub-giants are required.

Both of these pathways require much more asteroseismic data than is currently available. For ensemble fitting to be viable many subgiants would need to be observed over long baselines with short cadence observations. If the Kepler mission is exemplary, then the baseline required for high-SNR asteroseismic observations is on the order of 4 years per star.

At the time of writing, 30 subgiants show evidence of rotational splittings ([Li et al., 2020b,a](#)), though the rotational splitting data is yet to be released and analysed. The results will be undoubtedly informative, though we will not speculate exactly how much they will solve the subgiant excess angular momentum transport problem. [Hatt et al. \(2023\)](#) suggests that there is ~ 4000 stars in the TESS - short cadence catalogue with observable solar-like oscillation features. The measured frequency of peak oscillation power ν_{\max} of stars in these sample suggests that some of these stars are subgiants. While no rotational splittings of these stars have been reported some of these stars may lay in the continuous viewing zone. This means their observation periods are approaching 4 years at time of writing and these stars may soon offer a separate sample of subgiants with observations of asteroseismic rotational splittings. While we may speculate about future asteroseismic focussed missions, it will be some time before any new asteroseismic rotation signals in subgiants are made.

Independent constraints can also be placed on the evolution of the surface rotation of subgiants. [Santos et al. \(2021\)](#) measured the surface rotation of 4500 subgiants using photometric oscillations from stellar spots. The measured rotational periods against their effective temperature are shown in Figure 1.11. Within this Figure, there are a few notable features. While subgiants are definitionally older than their main-sequence counterparts, there is a sample of fast-rotating stars coincident with the fast rotators on the main sequence. This could be explained by most of the stars in this sample being a

higher mass than the Kraft break. They have passed through the main sequence with fast rotating surfaces, entering the subgiant phase; their effective temperatures decrease and are shifted to the right in this diagram relative to their main-sequence counterparts. The high density of fast-rotating stars could also result from an observational bias. Long rotational periods require longer baselines to recover and thus have a decreased observed fraction. Among the sample is a group of slow-rotating (Period > 60 days) targets with Teff between 5000 and 6000 K. These are consistent with more evolved subgiants as the slowest of these targets are located close to the red giant branch. This work also suggests that the decreased observation of rotation periods >60 days, the strong upper edge of the [McQuillan et al. \(2014\)](#) rotational period distribution, is the result of a lack of observations of main-sequence stars rather than an inherent lack of long period probing power by *Kepler*. Whether the upper edge results from angular momentum transport or decreased photometric variability is unknown. The final feature that is not commented on in their work is an apparent dearth of observations coincident with the intermediate period gap. Whether this is real or a result of noise is an interesting avenue of research in further understanding the underlying mechanism of the intermediate period gap for main sequence stars.

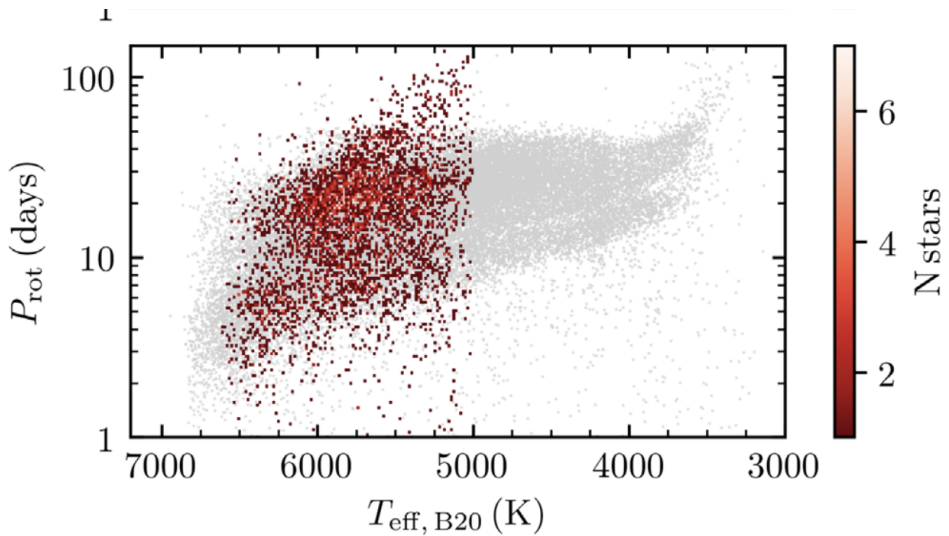


FIGURE 1.11: Surface rotation period against effective temperature of subgiants in the [Santos et al. \(2021\)](#) sample overlayed over the *Kepler* [McQuillan et al. \(2014\)](#) sample. Sourced from the bottom panel of Figure 5 in ([Santos et al., 2021](#)).

[Ceillier et al. \(2017\)](#) measured the surface rotation periods of 361 red giants from stellar spot photometric variability. The measured rotational periods against their mass are shown in Figure 1.12. Expectedly, comparative to the subgiant analysis of [Santos](#)

et al. (2021) the surface rotation period of red giant stars is greater than their subgiant counterparts. They suggest that the surfaces of these stars rotate faster than models suggest (Tayar et al., 2015). They conclude that the large percentage of rapid rotators must result from interactions of red giants with other bodies. This work, however, is older than the revised excess angular momentum transport research discussed earlier in this work. Their results need to be reexamined within the context of excess angular momentum transport.

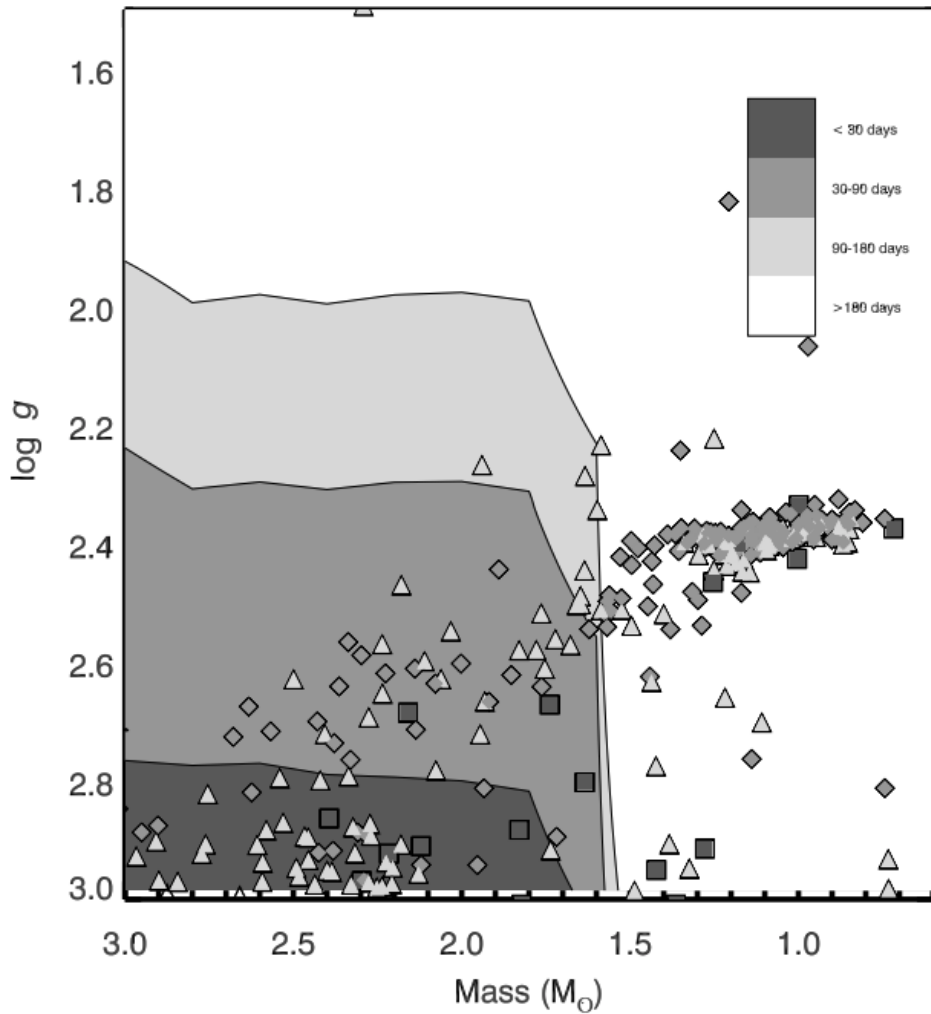


FIGURE 1.12: Surface rotation period against mass of red giant stars from Ceillier et al. (2017). Sourced from the top panel of Figure 7 in (Ceillier et al., 2017).

Finally, we discuss the rotating remnants of low-mass post-main-sequence evolution: white dwarfs. White dwarfs do not evolve rotationally, though their observed rotation rates constrain angular momentum during the red clump phase. Hermes et al. (2017) suggest that the rotation periods of white dwarfs decrease with the progenitor's mass.

As previously discussed, the surface rotation rates of white dwarfs are consistent with angular momentum conservation following the red clump ([den Hartogh et al., 2019](#); [Cantiello et al., 2014](#)). This is because the time scale of angular momentum transport is longer than the timescale of evolution from red clump star to a white dwarf. [den Hartogh et al. \(2019\)](#) suggest that mass-dependent angular momentum transport must decrease with evolution along the red clump such that the angular momentum of terminal red clump rotation cores agree with the angular momentum of white dwarf stars.

1.3 Effects of rotation

Within the previous Section, we discussed the evolution of rotation from birth to remnants of evolution. While we now have an understanding of this evolution, we still need to clarify the effects of rotation on stellar evolution.

1.3.1 Hydrostatic effects

The effects of rotation on stellar evolution are varied and complex. In general, the hydrostatic effects of rotation have only minimal effects on the internal evolution of stars ([Kippenhahn et al., 1970](#); [Maeder & Meynet, 2000](#)). Especially the low-mass, slowly rotating stars we consider in this work. In this Section, we review how some of these effects are treated in current models of stellar evolution, the resulting changes to stellar evolution brought about by these effects and their observable consequences. We will begin by discussing the effects of stellar rotation on hydrostatic equilibrium.

As a star rotates, its equilibrium configuration deviates from the non-rotating hydrostatic equilibrium due to centrifugal forces. Rotation-induced centrifugal forces induce deviations from spherical symmetry. Only if the rotation energy of a star approaches a significant fraction of the gravitational potential energy will observable triaxial deformation occurs. Low-mass stars usually rotate slowly, so these effects are rarely seen.

The four equations of stellar structure need to account for this change to the equilibrium configuration. [Kippenhahn & Thomas \(1970\)](#) devised the method to account for this where a conservative potential exists. In this method, they replace the notion of spherical stratification of non-rotating stars with a rotationally deformed shellular stratification

where the structural variables - e.g. pressure (P), density (ρ), temperature (T), chemical abundances - are constant on an equipotential. The equipotential in this prescription is defined as $\Psi = \Phi + \frac{1}{2}\Omega^2 r^2 \sin^2 \theta$, the non-rotating gravitational potential modulated by the centrifugal force, where Φ is the gravitational potential, θ the latitude relative to the rotational axis and Ω the angular rotation rate. This method applies only when a conservative potential exists, i.e. when the angular velocity distribution is cylindrically symmetric (Tassoul, 1978). The internal rotation generally evolves towards rotation laws that are non-conservative. For example, Zahn (1992) suggests that turbulence is anisotropic, with a stronger transport horizontally than vertically. This results in a constant rotation rate on isobars and does not fall into the conservative case. Maeder & Meynet (1996) revise Kippenhahn (1974)'s method and prescribe a consistent description of shellular rotation on isobars which is valid for slow rotation. On these isobars, the non-rotating stellar variables and angular momentum are constant. This allows models of rotating stellar evolution to be kept one-dimensional.

The equations of stellar structure are mainly affected by rotation through a few key concepts. Centrifugal forces reduce effective gravity for all points in the star that are not on the axis of rotation. The centrifugal forces vary with radial distance and latitude, resulting in equipotentials closer together along the rotational axis than the equatorial axis. Radiative flux varies with local effective gravity (von Zeipel, 1924). This results in gravitational darkening (von Zeipel, 1924; Kippenhahn, 1977) - stars are higher temperature and have larger temperature and radiation flux along the rotational axis compared to the equatorial axis. Gravity darkening of slowly rotating stars (rotation rates much slower than the break-up velocity like those considered in this work) is very small - $<<0.1\%$ variation in luminosity and temperature across their surfaces. Stars close to critical rotation rate should be treated with care (Kippenhahn, 1977; Maeder, 1999; Heger et al., 2000).

1.3.2 Increased mixing in stars

Rotation can extend the mixing regions in stars - allowing mixing between the radiative core and convective envelope - and increase the mixing efficiency through meridional circulation and rotational instabilities.

For convenience, throughout the following Section, we make use of the following gradients:

$$\nabla_{\text{ad}} := \left(\frac{\partial \ln T}{\partial \ln P} \right)_{\text{ad}}, \quad \nabla_\mu := \frac{d \ln \mu}{d \ln P}, \quad \nabla := \frac{d \ln T}{d \ln P} \quad (1.2)$$

$$\delta := - \left(\frac{\partial \ln \rho}{\partial \ln T} \right)_{\mu, P}, \quad \varphi := \left(\frac{\partial \ln \rho}{\partial \ln \mu} \right)_{P, T}, \quad (1.3)$$

where μ is the mean molecular weight at a given position in a star. The subscript "ad" refers to the gradient if we adiabatically transported a fluid element along a path. ∇ is simply the temperature gradient relative to the pressure gradient, ∇_{ad} is our temperature gradient relative to the pressure gradient along an adiabat, that is, the temperature gradient that arises from adiabatically transporting fluid elements along P , ∇_μ is the composition gradient with relative to the changing pressure, δ is the density gradient relative to the temperature along paths of constant μ and P and φ is the density gradient relative to the mean molecular weight along paths of constant P and T .

In non-rotating stars, mixing can be simplified by whether a region in a star is convective, semi-convective, radiative or undergoing thermohaline mixing (These concepts will not be discussed at length in this work. See [Maeder & Meynet, 2000](#); [Tassoul, 2000](#), for good overviews of these concepts.) Convective regions are well mixed and have no chemical gradients, as convection acts on local dynamical time scales, while radiative regions are not well mixed and are generally chemically stratified. Semi-convective regions are thermally unstable regions stabilised against convection by a gradient in composition. Thermohaline mixing arises when an unstable gradient in composition (mean molecular weight) is only partially stabilised by thermal stability. Semi-convection and thermohaline mixing act on longer time scales than convection; their effective diffusion coefficient is smaller. The conditions required for semi-convection and thermohaline mixing are well discussed in the works referenced above. Here we will focus on convective and radiative regions for simplicity. Whether a region is convective or radiative is defined by whether the Brunt-Väisälä frequency, the characteristic oscillation frequency of a displaced particle of fluid in a stratified density medium is positive or negative.

$$N^2 = \frac{g\delta}{H_P} \left(\nabla_{\text{ad}} - \nabla + \frac{\varphi}{\delta} \nabla_\mu \right), \quad (1.4)$$

where H_P is the local pressure scale height ($H_P = \frac{P}{\rho g}$ in hydrostatic equilibrium, where P is local pressure, ρ is local density and g local effective gravity). Rotation can

overcome the pressure, density and mean molecular weight gradients to push mixing into previously stable regions through rotational instabilities.

When we discuss the Brunt-Väisälä frequency, it is worth thinking of the characteristic oscillations of mass parcels. When the Brunt-Väisälä frequency is negative, the oscillations grow exponentially, leading to enhanced mixing. The mixing process is treated as essentially instantaneous in models. When it is positive, the oscillations are bounded, and mixing does not occur. On the other hand, when the Brunt-Väisälä frequency is negative but very close to zero, the oscillations grow slower than in the case of convection. While some instabilities act on dynamical time scales, we do not treat diffusion due to instabilities as if they were convective. In that way, we separate the effect of instabilities by their contribution to the total effective diffusion at every point in a star.

Here we will briefly discuss a non-exhaustive list of rotational instabilities and how they impact the mixing of stars. Most of these instabilities are not expected to arise during the low-mass ($<8M_{sol}$) main-sequence evolution due to the small angular momentum gradients of main-sequence stars, as discussed in the previous Section. However, they are influential during evolutionary periods where strong rotational gradients arise: during the post-main-sequence or core envelope decoupling as suggested in some models of young-main sequence evolution ([Heger et al., 2000](#)).

We separate the instabilities by the timescale. They act upon dynamic and secular instabilities. We expect secular instabilities to act on during the main sequence when rotational gradients are small and evolutionary times scales are long. On the other hand, strong rotational gradients arise during the post-main-sequence. Dynamical instabilities also act on shorter timescales than evolutionary timescales in the post-main-sequence. As a result, dynamical instabilities are mainly expected to play a role during the post-main-sequence.

1.3.2.1 Dynamical shear instability

The dynamical shear instability arises when the energy that can be gained from a shear flow (a rotational gradient) is comparable to the work that must be done to displace a mass element adiabatically. This means the instability is inhibited by density gradients

but is very effective along isobars (Endal & Sofia, 1978; Pinsonneault et al., 1989; Heger, 1998), supporting the shellular isobaric representation of rotation in stellar models.

The condition for stability is dependent on the local rotational gradient modulating the Brunt-Väisälä frequency:

$$Ri = \frac{g\delta}{H_P} \left(\nabla_{ad} - \nabla + \frac{\varphi}{\delta} \nabla_\mu \right) \left(g \frac{d \ln r}{d\Omega} \right)^2 > Ri_C, \quad (1.5)$$

where ω is the angular rotation rate and Ri_C is the critical Richardson number = 1/4 (Zahn, 1974). The region is considered stable if $Ri > Ri_C$, and the diffusion coefficient is 0. When unstable, the diffusion coefficient is proportional to the extent to which the rotational gradient overcomes the chemical and temperature gradients, Ri/Ri_C , the spatial extent of the unstable region, and the local dynamical timescale.

1.3.2.2 Solberg-Høiland instability

The Solberg-Høiland instability occurs when introducing the centrifugal force to the net force on an adiabatically displaced mass element overcomes the thermal and chemical gradient stabilities. The condition for stability is given by:

$$R_{SH} = \frac{g\delta}{H_P} \left[\nabla_{ad} - \nabla + \frac{\varphi}{\delta} \nabla_\mu \right] + \frac{1}{r^3} \frac{d}{dr} (r^2 \Omega)^2 \geq 0, \quad (1.6)$$

The second term in the equation accounts for the introduction of rotation, where the specific angular momentum (j) is $r^2\Omega$ (Tassoul, 1978; Kippenhahn & Weigert, 1990; Heger et al., 2000). Under no rotation (or no angular momentum gradient), we recover the Brunt-Väisälä frequency.

For the Solberg-Høiland instability to occur, the second term in the equation must be negative and, therefore, only occurs in regions of decreasing angular momentum (a negative rotation gradient with respect to radius). The diffusion coefficient associated with this instability increases with R_{SH} - the more the angular momentum gradient overcomes the thermal stability, the greater the mixing effect -the spatial extent of the unstable region, the local dynamical timescale.

1.3.2.3 Secular shear instability

When thermal dissipation is significant, the restoring force of buoyancy is reduced, and the strict criteria for the dynamical shear instability to act can be relaxed. Due to this process requiring thermal dissipation, it operates on the relatively slower (secular) thermal-time scale, hence its name.

[Endal & Sofia \(1978\)](#) suggest two stability conditions against secular shear instability. The first is a modulation to the thermal stability component of the Brunt-Väisälä frequency by a product of the Reynolds number - a dimensionless fluid flow number - and Prandtl number (P_E):

$$R_{is,1} = P_E \frac{g\delta}{H_P} (\nabla_{ad} - \nabla) \left(g \frac{d \ln r}{d\Omega} \right)^2 > Ri_C, \quad (1.7)$$

where $P_E = \frac{Pr R_{e,c}}{8}$. $R_{e,c}$ is the critical Reynolds number of the flow of material, and Pr is the Prandtl number, the ratio of the thermal diffusion timescale to the angular momentum diffusion timescale (See [Tassoul, 1978](#); [Heger, 1998](#), and references therein for a more thorough explanation of these quantities and their implementation in models of stellar rotation).

The second condition is the mean molecular weight component of the dynamical shear instability, which is not affected by the relaxation of thermal adjustment

$$R_{is,2} = \nabla_\mu \frac{g\varphi}{H_P} \left(g \frac{d \ln r}{d\Omega} \right)^2 > Ri_C. \quad (1.8)$$

The need for the inclusion of this term is debated, however.

[Endal & Sofia \(1978\)](#) suggest that the diffusion coefficient scales with the characteristic velocity of the secular shear instability, the characteristic scale height - the combination of which provides the characteristic timescale - and either $R_{is,1}$ and $R_{is,2}$ whichever violates the criteria more.

Many works have shown that the molecular gradient inhibits mixing by up two orders of magnitude than observations suggest. Those who include the term include a factor on ∇_μ of order <0.05 to account for this ([Charbonnel et al., 1994](#); [Heger et al., 2000](#)).

[Maeder & Meynet \(1997\)](#) argues that the regions where molecular gradients are strong enough to inhibit mixing from the secular shear instability, near the core, are generally semi-convective and experience some mixing/turbulence already. They suggest that in a semi-convection region (or in any zone with other sources of turbulence), some fraction of the local energy excess in the shear is degraded by turbulence to change the local entropy gradient. They hypothesise that this turbulence will affect the shear energy and molecular gradient and calculate a diffusion coefficient under this assumption. They find that the diffusion coefficient is consistent with the semi-convective diffusion coefficient when turbulence overcomes the shear and towards $K/R_{is,1}$ when semi-convection is negligible (Consistent with the results of [Zahn, 1992](#)). [Talon & Zahn \(1997\)](#), on the other hand, account for the mixing effect of horizontal diffusion from semi-convection on the restoring force produced by the molecular gradient, which reduces its stabilising effect. Both works result in the diffusion of elements consistent with observations without adding new factors.

1.3.2.4 Meridional circulation

Meridional circulation ([Eddington, 1925](#)) arises from gravity darkening. Excess flux along the rotational axis heats material more than along the equator. This drives the large-scale circulation of material from the pole to the equator. This results in angular momentum transport and chemical transport. Early theoretical considerations of meridional circulation were not physically consistent. They predict inverse circulation (from the equator to the axis of rotation) close to the surface, and they did not conserve angular momentum ([Sweet, 1950; Mestel, 1953; Mestel & Spitzer, 1956; Kippenhahn & Weigert, 1990](#)).

Meridional circulation can be treated differently for the transport of elements and the transport of angular momentum. [Endal & Sofia \(1978\)](#) derived a In this prescription, the diffusion coefficient scales with the Eddington-Sweet velocity and the extent of the region where the process is in effect (See [Kippenhahn, 1974; Endal & Sofia, 1978; Heger et al., 2000](#)).

On the other hand, [Zahn \(1992\)](#) determined that energy conservation, gravity and angular momentum must be calculated simultaneously for a self-consistent and physically possible solution to be found. [Chaboyer & Zahn \(1992\)](#) showed that if the horizontal

component of turbulence is large, the effects of meridional circulation on the transport of elements is equivalent to a diffusion process with diffusion coefficient D_{mr} .

$$D_{\text{mr}} = \frac{|rU(r)|^2}{30D_h} \quad (1.9)$$

D_h is the coefficient of horizontal turbulence, $U(r)$ is the vertical component of the meridional circulation velocity, and r is the radius at which the components are calculated. While diffusion from horizontal turbulence is required for meridional circulation to be treated as a diffusive process, it is also inhibited.

Measurements of the Lithium-7 abundance in the sun support this prescription. The difference between the derived diffusion coefficients from Kippenhahn (1974); Endal & Sofia (1978); Heger et al. (2000) and Chaboyer & Zahn (1992) prescriptions is approximately a factor of 30 scaling. Pinsonneault et al. (1989) found that a scaling of 0.046 ($\sim 1/30$) of the Kippenhahn (1974) diffusion coefficient is required to reproduce the observed Lithium-7 abundances. Indeed the two prescriptions are appropriate with sufficient scaling.

Prescriptions for horizontal diffusivity (D_h) are lacking in physical motivation. Zahn (1992) suggests $|rU(r)|$ is an adequate prescription. Maeder (2003) derived an expression with respect to energy considerations, while Mathis & Zahn (2004) adapted a prescription from laboratory experiments. Mathis et al. (2018) suggest that the anisotropy of turbulent transport scales as $N^4\tau^2/(2\omega^2)$, where N and ω are the Brunt-Väisälä and rotation frequencies and τ the time scale characterising the source of the turbulence. Their results all generally agree though this does not suggest that they are the correct formalisation of horizontal diffusion.

Angular momentum transport by meridional circulation can be treated as an advective or diffusive process. Consider the path of a fluid element along a meridional eddy. Meridional circulation describes a rise of material along the rotational axis, descending at the equator. This results in the transport of angular momentum *against* the angular momentum gradient. On the other hand, implementing angular momentum transport as a wholly diffusive process is numerically simpler (Endal & Sofia, 1978; Pinsonneault et al., 1989; Heger et al., 2000). The two implementations may deviate in regions where meridional circulation dominates. The two implementations obtain similar results along

the main-sequence ([Talon & Zahn, 1997](#); [Heger et al., 2000](#)) where the evolutionary timescale is long enough for meridional circulation to be impactful.

[Zahn \(1992\)](#) derived the radial component of the velocity of meridional circulation ($U(r)$) under the effects of thermal and molecular weight gradients.

$$U(r) = \frac{1}{H_P C_P T [\nabla_{\text{ad}} - \nabla + (\varphi/\delta) \nabla_\mu]} \left(\frac{L}{M} (E_\Omega + E_\mu) \right), \quad (1.10)$$

where C_P is the specific heat and E_Ω and E_μ are terms dependent on up to the third order derivatives of the rotational distribution and molecular mass distribution (See [Maeder & Zahn, 1998](#)). This prescription for meridional circulation resolves the inverse circulation of earlier prescriptions and conserves angular momentum.

1.3.2.5 Goldreich-Shubert-Fricke instability

The Goldreich-Shubert-Fricke (GSF) instability arises when a fluid is unstable to axisymmetric displacements ([Goldreich & Schubert, 1967](#); [Fricke, 1967](#)). Stars tend to be inviscid, $P_R \ll 1$. Under this assumption [Kippenhahn et al. \(1970\)](#) derives two conditions for stability. The first is the secular analogue of the Solberg-Høiland condition for stability under the assumption that the stability from the temperature gradient is removed by thermal conduction

$$\frac{\partial j}{\partial r} \geq 0. \quad (1.11)$$

The second is an analogue to the Taylor-Proudman theorem for slowly rotating incompressible fluid [Kippenhahn \(1974\)](#); [Tassoul \(1978\)](#); [Heger et al. \(2000\)](#).

$$\frac{\partial \Omega}{\partial z} = 0, \quad (1.12)$$

where z is the distance along the rotational axis. Fluids are well mixed along equipotentials. As discussed concerning the Von-Zeipal effect, equipotentials are closer along the rotational axis. Along an equipotential, if the rotation rate gradient is non-zero, then fluid will be mixed along said equipotential until the rotation profile is conservative. Stability favours uniform rotation on equipotentials, which is incompatible with shellular rotation except under solid-body rotation. The GSF instability, therefore, tends to enforce uniform rotation on thermal timescales ([Endal & Sofia, 1978](#)).

The GSF instability demands mixing from meridional circulation and thus, like meridional circulation, acts on the circularisation timescale.

1.3.3 Magneto-rotational instabilities

The role of magneto-rotational instabilities in the rotation of stars is debated. In this Section, we will discuss the theory behind a few of these instabilities and their effects in reference to the post-main-sequence rotational evolution.

Models of post-main-sequence rotational evolution with magnetorotational angular momentum transport suggest that the rotational profile of stars that have undergone significant angular momentum transport track include a strong rotational gradient following the H-burning shell (Fuller et al., 2019; Moyano et al., 2022).

1.3.3.1 Tayler instability and the Spruit Dynamo

The Tayler instability arises from the interaction between rotation and magnetic fields in a conducting fluid. If the magnetic field is aligned with the rotation axis, the Coriolis force tends to twist the field lines into a helical shape. This can lead to a buildup of tension in the field lines, which can trigger a series of instabilities that amplify the magnetic field. The end result is a complex pattern of magnetic fields that can drive large-scale flows in the fluid.

The Spruit dynamo, on the other hand, arises from the interaction between rotation and shear flows in a rotating fluid (Spruit, 2002). A radial gradient in the rotation rate can generate a shearing motion that can stretch and amplify the magnetic field lines. This process can lead to the buildup of magnetic energy and the generation of large-scale magnetic fields.

Combining these two mechanisms can lead to forming a self-sustaining magnetic dynamo in rotating stars (Spruit, 1999). The Tayler instability can amplify the magnetic field on small scales, while the Spruit dynamo can amplify the magnetic field on large scales. The resulting magnetic fields can drive large-scale flows in the fluid, which in turn can modify the rotation rate and generate new instabilities (Fuller et al., 2015, 2019)

The instability could be effective even if the initial field strength is small (Spruit & Phinney, 1998). Unfortunately, little is known about the initial field's strength and the efficiency of instabilities in amplifying the magnetic field. Fuller et al. (2019) suggests that the Tayler-Spruit instability could play a role in the post-main-sequence angular momentum transport problem discussed in Section 1.2.

1.3.3.2 Azimuthal Magnetorotational instability

The azimuthal magnetorotational instability (AMRI) is a type of instability that can arise in rotating, magnetised plasmas (Hollerbach et al., 2010). It is a variation of the more well-known magnetorotational instability (MRI), which occurs when a weak magnetic field is present in a rotating fluid or plasma.

The AMRI occurs when the magnetic field is not aligned with the rotation axis but is instead perpendicular to it. This can happen in astrophysical systems where the magnetic field is generated by a dynamo mechanism or is inherited from the system's initial conditions. In such cases, the AMRI can become the dominant instability, driving large-scale fluid motions and enhancing the transport of angular momentum (Mishra et al., 2021; Moyano et al., 2022).

The basic idea behind the AMRI is that the magnetic field can act as a free energy source that fluid motions can tap. If the magnetic field is perpendicular to the rotation axis, it can introduce a new length scale into the system, leading to a wider range of unstable modes. This can result in the growth of perturbations not present in the MRI, leading to more complex dynamics.

The AMRI's strength depends on a star's internal degree of differential rotation. Moyano et al. (2022) has discussed the role of the AMRI in relation to the post-main-sequence angular momentum transport problem. They suggest that a consistent prescription of the AMRI dependent on the degree of internal differential rotation could explain the observed core and surface rotation rates of subgiants and red giants that have not reached the red giant bump.

1.3.4 Other angular momentum transport mechanisms

Here we describe other angular momentum transport mechanisms that are not instabilities but may play a role in the evolution of stellar rotation.

One of these mechanisms is angular momentum transport by internal gravity waves (IGWs) (Pantillon et al., 2007; Kim & MacGregor, 2000; Talon & Charbonnel, 2005; Charbonnel & Talon, 2008) IGWs are internal propagation waves that can carry angular momentum from the core to the surface of stars.

Buoyancy forces in a stratified fluid drive internal gravity waves. In a rotating fluid, these waves can become distorted by the Coriolis force, leading to the angular momentum transfer between different fluid layers. The wave motion can induce a net angular momentum flux, leading to changes in the rotation rate (Zahn, 1975).

One key aspect of this theory is the identification of the so-called "critical layers", which are regions where the wave frequency matches the local rotation frequency. These layers can lead to a resonance between the wave and the rotation, leading to enhanced transport of angular momentum (Charbonnel & Talon, 2005).

The characteristic rotation profile that would suggest IGWs are at play is a strong rotational gradient tracking the H-burning shell (Balbus & Hawley, 1994; Menou & Mer, 2006).

Another mechanism that may play a role in post-main-sequence angular momentum transport is the transport of material by mixed modes (Belkacem et al., 2015). Comparative to the main sequence, post-main sequence stars express mixed modes when only pressure (p) waves propagate in the surface (convective) region. Mixed modes are gravity (g) modes that are usually constrained to the radiative core that have coupled with p modes.

Belkacem et al. (2015) suggests this process can extract angular momentum from the core of subgiants and red giants.

The efficiency of this angular momentum transport mechanism grows with the radial differential rotation gradient within stars and is thus strongest for red giants. Their results of this work suggest that while this mechanism may be at play, it is not strong enough to account for the observed core and surface rotation rates of subgiants.

1.3.5 Implementation of diffusive processes in models of rotating stellar evolution

1.3.5.1 Transport of Angular momentum

Angular momentum is transported by convection, mixing by instabilities and meridional circulation. The equation for the transport of angular momentum between shells, as an advective process, is

$$\rho \frac{d}{dt} (r^2 \Omega(r))_{M_r} = \frac{1}{5r^2} \frac{\partial}{\partial r} (\rho r^4 \Omega(r) U(r)) + \frac{1}{r^2} \frac{\partial}{\partial r} \left(\rho (D_{\text{tot}}) r^4 \frac{\partial \Omega(r)}{\partial r} \right), \quad (1.13)$$

where subscript M_r is the mass coordinate at a radius (r), ρ is the local density, $U(r)$ is given by Equation 1.10, $r^2 \omega$ is the angular momentum, and D_{tot} is the sum of the diffusion coefficients from the various diffusion processes discussed in the previous Section. The factor of 1/5 comes from the integration with respect to latitude (Zahn, 1992; Maeder & Zahn, 1998; Maeder & Meynet, 2000; Eggenberger et al., 2008).

The first term on the right-hand side accounts for angular momentum transport by meridional circulation. The second accounts for the transport of angular momentum by mixing processes. If meridional circulation is treated as a diffusive process then the first term is lost and the sum of the diffusion coefficients gains a meridional circulation term from Equation 1.9.

Equation 1.13 is subject to the boundary conditions at a star's core and surface. The core is subject to the boundary condition that $\frac{\partial \omega}{\partial r} = 0$ (Talon & Zahn, 1997; Denissenkov et al., 2010). The surface boundary condition can be treated in several ways. One way is to treat the boundary condition the same as the core, where no angular momentum is lost from the surface. On the other hand, the surface can be treated as an angular momentum sink. Mass loss by winds and the coupling of the mass loss to the magnetic field transport angular momentum away from the surface of a star. In the latter scenario

$$\rho \frac{d}{dt} (r^2 \Omega(r))_{\text{surf.}} = j_{\text{winds}}. \quad (1.14)$$

The rotation profile of a star is not chosen. Generally speaking, the initial condition is a flat rotation profile at the zero-age-main-sequence, which can evolve with time

due to angular momentum transport by meridional circulation, diffusive processes, and contraction or expansion. These processes' rotation profile changes are then accounted for by the angular momentum transport mechanisms - which are dependent on the rotation profile. As a result, a self-consistent solution for the evolution of the rotation profile is created.

1.3.5.2 Transport of Elements

Unlike angular momentum transport, the transport of elements can be treated as a diffusive process ([Endal & Sofia, 1978](#); [Heger et al., 2000](#))

Under this assumption, change in mass fraction X_i of chemical species i is

$$\left(\frac{dX_i}{dt} \right)_{M_r} = \left(\frac{\partial}{\partial M_r} \right)_t \left[(4\pi r^2 \rho)^2 D_{chem} \left(\frac{\partial X_i}{\partial M_r} \right)_t \right] + \left(\frac{dX_i}{dt} \right)_{nuc}, \quad (1.15)$$

where subscripts denote where each component is calculated, M_r is the mass coordinate at a radius (r), ρ is the local density, D_{chem} is the total mixing coefficient from turbulent diffusion processes and the effective diffusion coefficient from meridional circulation ($D_{chem} = D_{tot} + D_{MR}$).

The first term reflects the mixing of elements, and the second accounts for the change in elemental abundances from nuclear reactions.

1.3.6 Stellar Winds

Mass loss can significantly affect the evolution of stars, especially in massive stars. Rotation enhances the loss of mass through stellar winds of stars. [Friend & Abbott \(1986\)](#); [Langer \(1991\)](#); [Heger \(1998\)](#) suggest that the mass loss rate of rotating stars scales with rotation rate according to

$$\dot{M}(\Omega) := \dot{M}(\Omega = 0) \left(\frac{1}{1 - \nu_{frac}} \right)^\xi, \quad (1.16)$$

where $\xi \approx 0.43$,

$$\nu_{frac} := \frac{\nu}{\nu_{crit}}, \quad (1.17)$$

is the ratio of the equatorial surface rotation rate to the critical (break-up) rotation rate

$$\nu_{\text{crit}}^2 := \frac{Gm}{r} (1 - \Gamma), \quad (1.18)$$

for a body with mass m at radius r . G is the gravitational constant and

$$\Gamma := \frac{\kappa L}{4\pi c G m}, \quad (1.19)$$

is the Eddington factor where κ is the opacity, L is the luminosity of the object, and c is the speed of light.

Under this prescription, the effect of rotation on mass loss for low-mass and slowly rotating stars is negligible and requires a separate prescription for mass loss without rotation.

Massive stars ($>1.3 M_\odot$) do not have convective surfaces. A convective surface is required for a strong surface magnetic dynamo. The stellar winds of massive stars do not, therefore, coupled with a magnetic field and the angular momentum loss by stellar winds is simply

$$\dot{J} = \dot{M} j_{\text{surf}} = \dot{M} \Omega(R) R^2, \quad (1.20)$$

where j_{surf} is the specific surface angular momentum, $\Omega(R)$ is the rotation rate at the surface of the star, and R is the surface radius.

Stars with convective surfaces do have a surface magnetic dynamo. Surface angular momentum loss must be treated with slightly more care. [Parker \(1958\); Schatzman \(1962\)](#) recognised that a rotating magnetised star that loses mass through ionised winds will lose more angular momentum through winds than a non-magnetised star. The enhanced spin-down results from the material in the wind having a larger specific angular momentum than the material in the star. This is because of the angular momentum contained in the stresses of the magnetic field [Weber & Davis \(1967\)](#). As the ionised wind propagates from the surface of the star, the angular momentum held in the magnetic field is transferred to the gas, removing angular momentum from the system.

One could also consider this process relative to Equation 1.20. Within that model, the specific angular momentum of the wind at the equator is $\Omega(R)R^2$. In the presence of a magnetic field, the wind torque is equivalent to what it would be if the material along

the equator was held in corotation with the surface of the star to the Alfvén radius, R_A , and then released. In this case, the angular momentum per unit mass lost in the wind in the equatorial plane is ΩR_A^2 . $R_A > R$, and as a result, angular momentum loss is enhanced.

The rate of a star's loss of angular momentum depends on several factors, including the magnetic field, wind mass loss rate, mass and radius of the star, and angular velocity. There are difficulties in relating wind torque to these factors, and many models have used a formula by Kawaler that has limitations. A more realistic formula was proposed by (Matt et al., 2012), based on 2D magnetohydrodynamic wind models that solve Alfvén surface self-consistently.

In the absence of internal angular momentum transport the spin-down rate of a star is given by

$$\frac{d\Omega}{dt} = \frac{1}{I} \left(\tau_w - \frac{dJ}{dt} \Omega \right), \quad (1.21)$$

where I is the moment of inertia of a star, $\tau_w = dJ/dt$ is the torque on the star by the stellar wind and J is the star's angular momentum.

Matt et al. (2012) prescribe the torque by winds based upon the 2D magnetohydrodynamic simulations. They find that the torque is related to the mass (M), radius (R), equatorial surface rotation rate (Ω), equatorial magnetic dipole field strength (B_{dip}) and mass loss rate (\dot{M}) of a star as

$$\tau = K_1^2 B_{\text{dip}}^{4m} \dot{M}^{1-2m} R^{4m+2} \frac{\Omega}{(K_2^2 \nu_{\text{esc}}^2 + \Omega^2 R^2)^m}, \quad (1.22)$$

where $K_1 = 1.3$, $K_2 = 0.0506$, and $m = 0.21777$ are tuned parameters obtained in their work, and ν_{esc} is the surface escape velocity ($\nu_{\text{esc}} = \sqrt{2GM/R}$).

Johnstone et al. (2015a) suggest that the dipole magnetic field strength and mass loss rate can be highly uncertain and are not well constrained by observations. They introduce a free parameter scaling to τ by setting

$$\tau_w = K_\tau \tau. \quad (1.23)$$

They found that $K_\tau = 11$ was required to match observations of the spin-down of the sun.

The use of Equation 1.22 requires a prescription of the mass loss rate and equatorial dipole magnetic field strength. Matt et al. (2012); Gallet & Bouvier (2013); Johnstone et al. (2015a) suggest that the mass loss and magnetic field strength must saturate below a certain Rossby number ($Ro = 0.1$). Observations of other magnetic activity indicators support this: coronal emission (Pizzolato et al., 2003; Wright et al., 2011; Núñez et al., 2022) as well as chromospheric diagnostics (Soderblom et al., 1993; Fang et al., 2018; Fritzevski et al., 2021).

They argue that the wind torque's dependence on rotation rate in the saturated regime must be weaker than in the unsaturated regime. They tune their angular momentum loss to open cluster rotation distribution measurements in the unsaturated regime. They find mass loss increases with increased rotation rate and decreases with mass: $\dot{M} \propto \Omega^{1.33} M^{-3.36}$. In the saturated regime \dot{M} scales with mass and takes the value of \dot{M} at the saturating Ω . They also assume that B_{dip} scales with the Rossby number and find that, in the unsaturated regime, $B_{\text{dip}} \propto (\Omega \tau_{\text{conv}})^{1.32}$, where τ_{conv} is the convective turnover timescale which varies with mass. In the saturated regime, the dipole field strength remains at the strength at the saturating Ω .

Under these assumptions, and assuming $R \propto M^{0.8}$ then the mass dependence in the unsaturated regime disappears, and the wind torque is prescribed relative to solar wind torque by

$$\tau_w = \tau_{w,\odot} \left(\frac{\Omega}{\Omega_\odot} \right)^{2.89}, \quad (1.24)$$

where $\tau_{w,\odot} = -7.15 \times 10^{30} \text{ erg s}^{-1}$ is the current solar wind torque. In the saturated regime, the mass dependence remains and is prescribed as

$$\tau_w = \tau_{w,\odot} 15^{1.89} \left(\frac{\Omega}{\Omega_\odot} \right) \left(\frac{M}{M_\odot} \right)^{4.42}. \quad (1.25)$$

Under these prescriptions, and a constant internal angular momentum transport from the core to the surface, this prescription qualitatively agrees with the rotational distributions of young clusters. The wind dependence decreases for unsaturated, slower rotating, older stars, and the rotational rate evolution is consistent with the observed Skumanich relation (Skumanich, 1972). That being said, our understanding of the evolution of stellar winds on the main sequence is still being determined, primarily because of limited knowledge about stellar winds and the wide range of rotation rates observed

at young ages. Without strong prescriptions of stellar winds, comparing observations with internal angular momentum transport models lose their informative value.

1.3.7 Summary - Effects of rotation on low-mass evolution

In this Section, we will summarise the observable features of rotation on low-mass stellar evolution. Comparative to high-mass rotating stellar evolution, the indicators of low-mass rotating stellar evolution are minimal (See [Heger et al., 2000; Maeder & Meynet, 2000](#)). The rotation rate is the main observable property of the evolution of rotation in stars. As this was discussed in length in Section 1.2 we will focus here on the impact of rotation on other observable quantities and a star's evolution.

1.3.7.1 Pre-main sequence

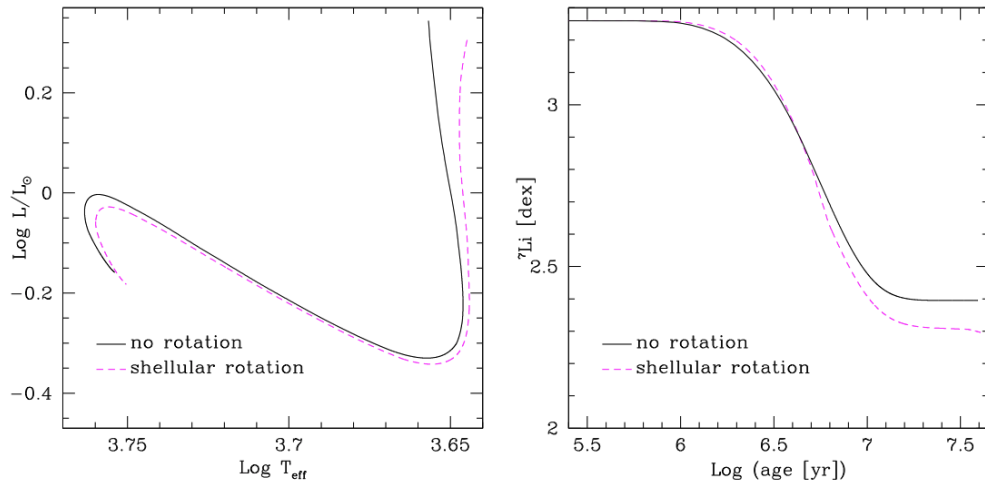


FIGURE 1.13: Left: PMS HR diagram tracks of $1 M_\odot$ solar metallicity models with and without rotation. The continuous line corresponds to a non-rotating model, while the dashed line corresponds to a rotating model with $\Omega = 20\Omega_\odot$. The tracks end when the ZAMS is reached. Right: Surface lithium abundance with time during the PMS for the same models. Sourced from Figure 1 in [Eggenberger \(2013\)](#)

Figure 1.13 (left) compares the evolutionary track of a rotating solar-type, $1M_\odot$, solar metallicity, star rotating with $20\Omega_\odot$ (twenty times the mean solar surface rotation rate) against a non-rotating model of the same mass and metallicity. Because of the introduction of the centrifugal force, the HR path is slightly shifted towards lower effective temperatures and luminosities than a non-rotating star.

During the pre-main sequence, both the changes to the rotation impact the observed lithium abundances, which are dependent on the treatment of angular momentum transport (Dumont et al., 2021). Figure 1.13 (right) displays the evolution of surface lithium abundance during the PMS phase for rotating and non-rotating models. The zero-age-main-sequence (ZAMS) surface lithium abundance of the rotating model is lower than that of the non-rotating model, indicating that including rotational effects increases lithium depletion during the PMS. However, during the beginning of the lithium depletion phase, the rotating model shows a slightly higher lithium content than the non-rotating one due to the centrifugal force lowering the temperature at the base of the convective envelope.

As the star develops a radiative zone at its centre, rotational mixing becomes the dominant factor in transporting lithium to deeper and hotter regions, where it is efficiently destroyed. This leads to a lower surface lithium abundance for the rotating model on the ZAMS compared to the non-rotating model due to the increase in differential rotation in the stellar interior during the PMS.

The duration of the disc-locking phase, which enhances differential rotation in the radiative zone, significantly impacts the sensitivity of the lithium content in rotating models. Longer disc lifetimes lead to lower surface lithium abundances on the ZAMS due to increased angular velocity gradients below the convective envelope, which enhance rotational mixing (Eggenberger et al., 2012). Moreover, as the star loses more angular momentum during the longer disc-locking phase, it reaches the ZAMS with a lower surface rotational velocity, resulting in lower lithium abundance. Therefore, a correlation between the surface velocity and lithium abundance on the ZAMS exists: stars with lower rotation rates on the ZAMS are expected to be more depleted in lithium than fast rotators on the ZAMS.

1.3.7.2 Main sequence

During the main sequence, rotational mixing begins to play a key role by changing the global stellar properties. This is illustrated in Figure 1.14 (left), which shows the main-sequence evolution for two $1 M_{\odot}$, solar metallicity models computed with and without rotation. The rotating model has an initial surface velocity of 50 km s^{-1}

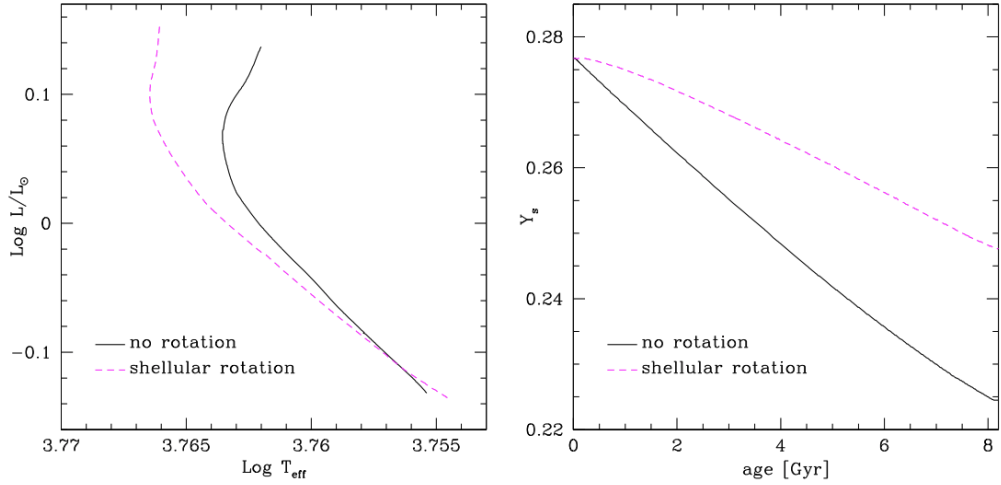


FIGURE 1.14: Left: MS HR diagram tracks of $1 M_\odot$ solar metallicity models with and without rotation. The continuous line corresponds to a non-rotating model, while the dashed line corresponds to a rotating model with ZAMS surface velocity = 50 km/s. The tracks end when the ZAMS is reached. Right: Surface helium abundance with time during the MS for the same models. Sourced from Figure 3 in Eggenberger (2013)

The rotating model is, like the PMS model, characterised by higher effective temperatures and slightly higher luminosities than the non-rotating model.

Figure 1.14 (right) highlights that the presence of rotational mixing counteracts the impact of atomic diffusion in the star's outer layers. This leads to higher helium surface abundances for the rotating model than the non-rotating model. Consequently, the opacity in the external layers of the rotating model decreases, causing a shift towards the blue region of the HR diagram, as illustrated in Figure 1.14 (left). The differences in helium content between rotating and non-rotating stars become increasingly pronounced during the main sequence, resulting in significant distinctions in the HR diagram.

Furthermore, the inclusion of rotation affects the properties of the central layers of the star. As a result of rotational mixing, fresh hydrogen fuel is transported to the central core, leading to a higher central hydrogen mass fraction for rotating models than for models without rotation at a given age. This leads to an increase in the main-sequence lifetime.

1.3.7.3 Post-main sequence

Within the post-main sequence, the rotation effects are similar to the main sequence. When rotational effects are considered, the core helium-burning phase is shifted to higher

luminosity values. These changes are due to rotational mixing, which brings fresh hydrogen fuel into the convective core and transports helium and other H-burning products in the radiative zone.

There are no other significant enhancements in chemical abundances (See Table 2. in [Lagarde et al., 2012](#)). Rotation can, however, substantially affect the asteroseismic properties of low-mass red-giant stars [Lagarde et al. \(2012\)](#); [Eggenberger et al. \(2010\)](#). In particular, rotation decreases the derived stellar mass and increases the age. Observation and identification of non-radial oscillation modes for red giants with moderate surface rotational velocities may be complicated due to non-negligible values of rotational splitting, which can be reached depending on the assumed rotation law in the convective envelope and the star's initial velocity.

[\(Eggenberger et al., 2010; Lagarde et al., 2012\)](#) also illustrates that the HR evolution of rotating stars can be qualitatively reproduced with enhancements to the core overshooting parameter. This highlights that rotation increases the size of the convective core and changes the chemical composition of the radiative zone.

1.4 Todo

Write section on ways that observations of rotation are made - precise techniques.

- Rotation period from light curves - acf method and periodogram
- Doppler broadening spectroscopy
- Asteroseismic inference of rotation rate - OLA techniques + Forward modelling

Chapter 2

Constraining the Rotation Profile in a Low-Luminosity Subgiant with a Surface Rotation Measurement

Preamble

This chapter was originally published as:

[Wilson et al. \(2023\)](#)

Constraining the rotation profile in a low-luminosity subgiant with a surface rotation measurement

Tanner A. Wilson^{1,2}★ Andrew R. Casey^{1,2} Ilya Mandel^{1,3} Warrick H. Ball^{1,4} Earl P. Bellinger^{1,5,6} and Guy Davies^{4,6}

¹School of Physics & Astronomy, Monash University, Victoria, 3800, Australia

²Center of Excellence for Astrophysics in Three Dimensions (ASTRO-3D), Australia

³The ARC Center of Excellence for Gravitational Wave Discovery – OzGrav, Australia

⁴School of Physics and Astronomy, University of Birmingham, Edgbaston, B15 2TT, UK

⁵Max Planck Institute for Astrophysics, Garching, 85748, Germany

⁶Stellar Astrophysics Centre (SAC), Department of Physics and Astronomy, Aarhus University, Aarhus C, DK-8000, Denmark

Accepted 2023 March 10. Received 2023 March 7; in original form 2023 February 3

Downloaded from https://academic.oup.com/mnras/article/521/3/4122/7080167 by Monash University user on 11 July 2023

ABSTRACT

Rotationally induced mode splitting frequencies of low-luminosity subgiants suggest that angular momentum transport mechanisms are 1–2 orders of magnitude more efficient in these stars than predicted by theory. Constraints on the rotation profile of low-luminosity subgiants could be used to identify the dominant mechanism for angular momentum transport. We develop a forward model for the rotation profile given observed rotational splittings, assuming a step-like rotation profile. We identify a consistent degeneracy between the position of the profile discontinuity and the surface rotation rate. We perform mock experiments that show the discontinuity position can be better constrained with a prior on the surface rotation rate, which is informed by star spot modulations. We finally apply this approach to KIC 12508433, a well-studied low-luminosity subgiant, as an example case. With the observed surface rotation prior, we obtain a factor of 2 increase in precision of the position of strong rotation gradient. We recover the literature values of the core and surface rotation rates and find the highest support for a discontinuity in the radiative zone. Auxiliary measurements of surface rotation could substantially improve inferences on the rotation profile of low-luminosity subgiants with already available data.

Key words: asteroseismology – stars: rotation.

1 INTRODUCTION

All stars rotate. The rotation rate and distribution of angular momentum throughout a star evolves with time. The effects of rotation on the structure and evolution of a star are substantial (e.g. Heger 1998; Maeder & Meynet 2000), and accurate prescriptions of rotation in stellar models are important to reproduce observations, particularly asteroseismic measurements of oscillation modes.

Low-mass subgiants and low-luminosity red giants pulsate in mixed modes, which are sensitive to structure in both the core and envelope. Mixed modes result from the near-surface convection, which drives the oscillation modes to amplitudes that are detectable in space-based photometry missions like *CoRoT* (Baglin 2003) and *Kepler* (Borucki et al. 2010). Rotation lifts the degeneracy of oscillation modes of the same angular degree and azimuthal order. The change to the frequency of rotationally split modes is related to the rotation profile. For this reason, measuring rotational splittings allows us to constrain the rotation profile.

Current measurements of rotational splittings place low precision constraints on the core and surface rotation rates [≈ 10 per cent and 30 per cent, respectively (e.g. Deheuvels et al. 2014; Fellay et al.

2021)] and have little capability to constrain the shape of the rotation profile connecting the core and the surface. These observations, however, present some notable results. Subgiants demonstrate solid-body rotation early in their transition off the main-sequence (MS), like their MS counterparts (Deheuvels et al. 2020; Noll, Deheuvels & Ballot 2021). However, later in their post-MS evolution, the cores of more evolved subgiants and low-luminosity red giant branch (RGB) stars rotate much faster than their envelope. The core-to-surface rotation ratio can grow to ≈ 20 for stars leaving the subgiant phase (Deheuvels et al. 2014; Gehan et al. 2018; Eggenberger et al. 2019).

Stellar models predict differential rotation between the core and the surface to be two to three orders of magnitude greater than observations suggest (Eggenberger, Montalbán & Miglio 2012; Cantiello et al. 2014). The surface rotation rates of white dwarfs agree well with the core rotation rates of RGB stars (Gough 2015; Hermes et al. 2017), suggesting an angular momentum transport mechanism that is much more efficient throughout the first ascent of the RGB, and nowhere else (Eggenberger et al. 2012; Ceillier et al. 2013; Marques et al. 2013; Fuller et al. 2015; Spada et al. 2016; Ouazzani et al. 2018).

The angular momentum transport mechanism sets the rotation profile. The core-to-surface rotation ratio and the position and strength of the gradient of rotation rate can characterize the rotation profile. Fellay et al. (2021) suggest that tighter constraints can be

* E-mail: tanner.wilson@monash.edu

made on angular momentum transport mechanisms through more precise measures of the core-to-surface rotation ratios of post-MS stars (Deheuvels et al. 2014), and of the position and strength of a rotation rate gradient (Di Mauro et al. 2018). For example, a rotation profile with a constant rotation rate internal to the base of the convective zone (BCZ), and a decreased rotation rate that is inversely dependent on radius in the BCZ, could be indicative of angular momentum transport from deep fossil magnetic fields (Gough & Thompson 1990; Kissin & Thompson 2015; Takahashi & Langer 2021). This results from differential rotation being damped along poloidal field lines (Garaud 2002; Strugarek, Brun & Zahn 2011). On the other hand, a steep rotational gradient near the H-burning shell of a subgiant would indicate turbulent angular momentum transport. This could be in the form of internal gravity waves (Pinçon et al. 2017), leading to localized shallow gradients in the profile (Charbonnel & Talon 2005) or through magneto-rotational instabilities that arise from steep angular momentum gradients (Balbus & Hawley 1994; Arlt, Hollerbach & Rüdiger 2003; Menou & Mer 2006; Spada et al. 2016). The gradient of the rotation profile of subgiants is not well constrained through current asteroseismic data (Deheuvels et al. 2014).

In this work, we consider the constraints to the position of a steep rotational gradient, where we show that $\ell = 1, 2$ rotational splittings may be sufficient to make valuable inferences about the rotation profiles of low-luminosity subgiants if a precise auxiliary measure of surface rotation rate is available. We specifically investigate the impact of employing surface rotation periods from photometric variability owing to stellar spots (e.g. those measured in Garcia et al. 2014; McQuillan, Mazeh & Aigrain 2014; Santos et al. 2021). In adopting these values, we utilize a data set that overlaps with the subset used to measure asteroseismic rotational splittings. We deem it appropriate to employ both constraints simultaneously due to the distinct methods of measuring these quantities.

In Section 2, we describe a forward model to infer rotation profile parameters given observed rotational splittings, assuming a step rotation profile. We perform tests using mock data generated by three hypothetical profiles to show the differences in constraining the rotation profile with realistic independent measures of surface rotation rate from stellar spot brightness modulations. Finally, we perform inference on the observed rotational splittings of KIC 12508433 with different priors and compare the constraints on the rotation profile. The implications are discussed in Section 4 and summarized in Section 5.

2 METHOD AND RESULTS

2.1 Rotational splittings

Stellar oscillations can be decomposed into oscillating spherical harmonic modes. Individual modes frequencies ($v_{n,\ell,m}$) are characterized by their radial order (n), angular degree (ℓ), and azimuthal order (m). Low-luminosity subgiants have much longer rotation periods [of order 10^4 d (Deheuvels et al. 2014)] in the fast rotating core than the average oscillation period (on the order of hours; Aerts, Christensen-Dalsgaard & Kurtz 2010). We can therefore treat rotation as perturbative to the structure. The effect of stellar rotation on oscillation mode frequencies can be approximated as perturbations to the non-rotating mode frequencies from $m = 0$ to $m = -\ell$ and $m = \ell$. This is a widely employed approximation in the field of asteroseismic inversions of rotation (e.g. Deheuvels et al. 2014, 2015; Fellay et al. 2021). For more detail on this approach,

see Unno et al. (1989) and Aerts et al. (2010). To first order, the rotationally split oscillation frequencies are

$$v_{n,\ell,m} = v_{n,\ell,0} + \delta v_{n,\ell,m} \quad (1)$$

$$= v_{n,\ell,0} + m \delta v_{n,\ell}, \quad (2)$$

where $v_{n,\ell,m}$ is the frequency of the n, ℓ, m mode, $v_{n,\ell,0}$ is the frequency in the non-rotating case, and $\delta v_{n,\ell,m}$ is the change in oscillation frequency due to rotation, known as the rotational splitting. The difference between the $m = 0$ and $m \neq 0$ mode frequency is the m th multiple of the $\delta v_{n,\ell}$ rotational splitting. In practice, we are usually only able to observe $\ell = 1$ and $\ell = 2$ modes with $m = 1$ and $m = -1$ rotational splittings in low-luminosity subgiants from photometric time series data (Benomar et al. 2013; Deheuvels et al. 2014).

Rotational splittings are scaled averages of the rotation profile. The scaling is different for each oscillation mode and is quantified using a so-called rotational kernel. The rotational kernels are inherent to the thermodynamic structure of a star (see Aerts et al. 2010 for a derivation of these kernels). Assuming spherical symmetry, the n, ℓ rotational splitting is given by

$$\delta v_{n,\ell}(\Omega) = \beta_{n,\ell} \int_0^R K_{n,\ell}(r) \Omega(r) dr, \quad (3)$$

where $K_{n,\ell}$ is the rotational kernel of the n, ℓ mode (determined from a stellar model), $\Omega(r)$ is the scaled average, with respect to the polar axis, 1D rotation profile along the radial axis, $\beta_{n,\ell}$ is a normalization constant, and R is the outermost radius of the star. The rotational kernel, and thus scaled averaged frequency shift, changes with each oscillation mode. Changes to the rotation profile therefore result in distinct variances for each rotational splitting. Some rotation profiles are more likely to result in measurable rotational splittings than others. As a result we are able to use forward modelling to determine the set of likely rotation profiles given some observed rotational splittings.

2.2 Forward model

A forward model requires a set of rotation kernels to predict rotational splittings given some profile. In this work, we use rotational kernels of the low-luminosity subgiant KIC 12508433, a well-studied asteroseismic target (e.g. Deheuvels et al. 2014). Models of KIC 12508433 indicate that it is early in its evolution off the MS, which is supported by a relatively low core-to-surface rotation ratio. It is the earliest star known in its post-MS evolution with evidence of differential rotation.

We were provided with a model of KIC 12508433 from Ball & Gizon (2017) generated using the ASTERO module of the Modules for Experiments in Stellar Astrophysics (MESA) evolutionary code (r7624; Paxton et al. 2010, 2013, 2015, 2019). The model was found by simultaneously matching the non-seismic properties of KIC 12508433 (T_{eff} , $\log g$, and [Fe/H] in Table 1), the global seismic quantities – the frequency where peak power of the Gaussian asteroseismic power envelope occurs, v_{\max} , and the frequency spacing between consecutive radial order modes with the same angular degree, Δv – and the observed mode frequencies (see tables 1 and 3 in Deheuvels et al. 2014) to those predicted by the model. Mode frequencies were calculated using ADIPLS (Christensen-Dalsgaard 2008), with combined surface effect corrections to the frequencies (Ball & Gizon 2014, 2017).

Most of the observed and best-fit model quantities agree to within 1σ . The exceptions are T_{eff} and L where the agreement is within

Table 1. Measured properties of KIC 12508433 (Deheuvels et al. 2014), and those of the best-fitting stellar model from which the rotation kernels are generated.

	KIC 12508433	Model
$M (M_{\odot})$	1.20 ± 0.16	1.293
$R (R_{\odot})$	2.20 ± 0.10	2.277
$L (L_{\odot})$	3.25 ± 0.45	4.065
$\log g (\text{cm s}^{-2})$	3.83 ± 0.04	3.834
$T_{\text{eff, spec}} (\text{K})$	5248 ± 130	5434
[Fe/H] (dex)	0.25 ± 0.23	0.06

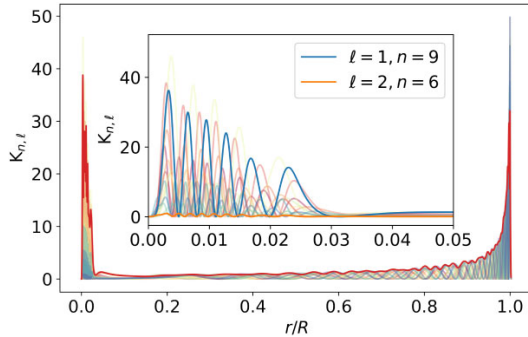


Figure 1. Rotational kernels for the best-fitting model of KIC 12508433. The red curve shows three times the local standard deviation of the set of observed kernels (kernel deviation). Regions with large kernel deviation are expected to be sensitive to the rotation profile following forward modelling. In this model, these regions can be seen in the H-burning shell core ($r/R < 0.05$) and nearing the surface ($r/R > 0.8$). The inset shows the same kernels with two modes highlighted: the $\ell = 1, n = 9$ mode (blue) is sensitive to core rotation and the $\ell = 2, n = 6$ (orange) is sensitive to surface rotation.

2σ . Our model T_{eff} is closer to the reported T_{eff} from the infrared flux method (Casagrande et al. 2010; 5302 ± 124 K from Deheuvels et al. 2014), but fully consistent with the spectroscopic effective temperature. L is not included in the χ^2 fitting of the model (M , R , and L are outputs of the model) and the value from Deheuvels et al. (2014) was estimated from scaling relations. This level of deviation varies with surface modelling assumptions (Ball & Gizon 2017), is consistent with previous works (e.g. Deheuvels et al. 2014; Li et al. 2020), and while rotational inversions of subgiants can be dependent on model uncertainties (Schunker, Schou & Ball 2016); this discrepancy is unlikely to affect the results of this work.

We used this model of KIC 12508433 to calculate the rotational kernels for all observable rotational splittings. Radial positions with both high kernel magnitude and inter-kernel variance (represented by the standard deviation of kernel magnitudes, shown in red in Fig. 1) are most sensitive to the rotation profile. For KIC 12508433, these regions are near the core and at $r/R > 0.8$.

Deheuvels et al. (2014) concluded that it is difficult to distinguish between smooth and discontinuous rotation profiles of low-luminosity subgiants using current data. Consequently, we assume a simple form of a rotation profile $\Omega(r)$ using three parameters of the following form:

$$\Omega(r) = \begin{cases} \Omega_c & r/R \leq p \\ \Omega_s & r/R > p \end{cases}, \quad (4)$$

where Ω_c and Ω_s describe the core and surface rotation rates, respectively, and p is the position of the step (in units of r/R). We

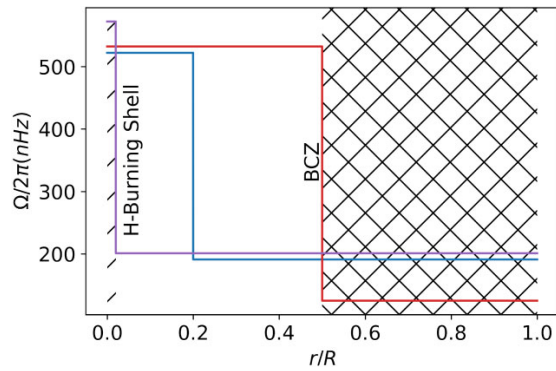


Figure 2. Three rotation profiles used in the mock data experiments. These profiles represent the extreme consequences of different angular momentum transport mechanisms in low-luminosity post-MS stars. Cross-hatching represents the convective surface region and diagonal-hatching represents the H-burning shell. See Section 3.1 for descriptions of each profile.

discuss the implications of the assumed step-function form of the rotation profile further in Section 4. Initially, we will assume weak uninformed, uniform priors on the core and surface rotation rate and a uniform prior on p :

$$p \sim \mathcal{U}(0, 1), \quad (5)$$

$$\Omega_s/2\pi \sim \mathcal{U}(0, 600) \text{ nHz}, \quad (6)$$

$$\Omega_c/2\pi \sim \mathcal{U}(0, 1000) \text{ nHz}, \quad (7)$$

where $\mathcal{U}(x, y)$ denotes a uniform prior between x and y . We calculate the expected rotational splitting frequencies $\delta\nu_{n,l}$ for all observable $\{n, l\}$ modes given a model $\Omega(r)$ and the rotational kernels $K_{n,l}(r)$ using equation (3), and assume the observed splitting frequencies are normally distributed with a log-likelihood

$$\ln \mathcal{L}(\delta\nu | \Omega_c, \Omega_s, p, \mathbf{K}(r), \boldsymbol{\sigma}_{\delta\nu}) \propto -\frac{1}{2} \sum_{n,l} \left(\frac{\delta\nu_{n,l} - \delta\nu_{\text{obs } n,l}}{\sigma_{\delta\nu_{n,l}}} \right)^2, \quad (8)$$

where $\delta\nu_{\text{obs } n,l}$ is the observed rotational splitting frequency for mode n and l , and its associated uncertainty is $\sigma_{\delta\nu_{n,l}}$. The vector-valued symbols $\delta\nu$, $\mathbf{K}(r)$, and $\boldsymbol{\sigma}_{\delta\nu}$ indicate that the log-likelihood depends on the corresponding values for all of the observed rotational splittings. We constructed this model using PyMC3 (Salvatier, Wiecki & Fonnesbeck 2016) and used the ‘No U-Turn Sampler’ (Hoffman & Gelman 2011) to draw samples from the posterior.

3 RESULTS

3.1 Mock data experiments with three hypothetical rotation profiles

We begin by generating mock data with our forward model to test the impact of independent measures of surface rotation rate. We chose three rotation profiles with extreme differences in the position of a strong rotational gradient, which represent hypothetical angular momentum transport mechanisms that could result in step-like rotation profiles. The three step positions are: in the H-burning shell (purple); in the radiative zone (blue); and at the base of the BCZ (red) as shown in Fig. 2. The mock rotation profiles are motivated by, but not representative of, various angular momentum transport

processes. The BCZ step rotation profile (red) is a signature of angular momentum transport by fossil magnetic fields, which results in solid body rotation in the radiative region and inverse rotation rate on radius in the convective region (Kissin & Thompson 2015; Takahashi & Langer 2021). The H-burning step rotation profile (purple) is indicative of turbulent angular momentum transport through internal gravity waves (Pinçon et al. 2017) or magnetorotational instabilities (Balbus & Hawley 1994; Arlt et al. 2003; Menou & Mer 2006; Spada et al. 2016) which result in a strong gradient in rotation rate close to the core. The radiative zone step profile (blue) corresponds to delocalized angular momentum transport from the core into the radiative zone and is not indicative of a specific angular momentum transport process.

The core and surface rotation rates will be realistically different for each profile/angular momentum transport process. To account for this for each profile, we fixed the step position and evaluated the log-likelihood (given the observed splittings of KIC 12508433) at each combination of (Ω_c, Ω_s) and set the rotation rates to those with the maximum log-likelihood. The resulting rotation profiles are shown in Fig. 2: radiative-zone step (blue: $p = 0.2$), a BCZ step (red: $p = 0.5$), and the H-burning shell step (purple: $p = 0.05$). The rotational splitting frequencies of these profiles were then calculated using (equation 3). We adopted uncertainties on those expected values given the precision of mode frequencies measured in KIC 12508433 (table 3 of Deheuvels et al. 2014). This provides us with three mock data sets to consider the rotation profile's effect on the observations.

We treated the mock data generated by each step profile as if it were real data and performed inference using the model and sampler described in Section 2.2. We performed inference twice: first with a flat prior on surface rotation and then with a Gaussian prior on surface rotation with mean equal to the injected surface rotation rate, and a standard deviation 10 per cent of the mean value. Here, we have chosen 10 per cent as representative of the average uncertainty on state-of-the-art measurements of MS and subgiant stellar rotation from photometric variation (Santos et al. 2021). We discuss this choice further in Section 4. We drew 20 000 posterior samples in each case. The 1D marginalized posterior samples with a flat and informed prior are compared in Fig. 3. The full posteriors are shown in the Appendix (Figs A1–A6).

When sampling with a uniform prior on surface rotation (Figs A1–A3), we identify multi-modality and a strong correlation between Ω_s and p : smaller Ω_s values tend to coincide with higher p values. The inferred step position p is very uncertain in all three cases, showing nearly uniform probability throughout the domain.

The impact of an auxiliary surface rotation rate measure on the posterior distributions is evident when comparing the normalized posterior density when using an uninformed prior (thin dashed) to the informed prior (thick solid) in Fig. 3. When the informed prior is introduced, the degeneracy between surface rotation rate and p is broken and the surface rotation rate and p are better recovered. In the H Shell step (purple) and radiative step (blue) experiments, the prior has collapsed support for $p > 0.4$. The introduction of the prior does not, however, allow us to differentiate between rotation profiles deeper in the star. We find that for profiles where $p \lesssim 0.2$, multimodality remains and the introduction of the prior on Ω_s increased support for p closer to the core (and closer to the true value). Indeed, the introduction of the informed prior for the H shell and radiative step experiments has constrained the posterior on p , but the 1σ range on these values overlaps significantly. We could not differentiate between these profiles using this method and state-of-the-art data. This is not the case for the BCZ mock data experiment. Introducing the informed surface rotation prior allows us to place

more significant constraints on p . The posterior on p was flat with an uninformed prior and the BCZ step. In contrast, with a surface rotation rate prior, the posterior is now a single peak centred at the injected value with a percentage standard deviation of the median value of about 18 per cent. This illustrates the constraining power on p of the independent measures of Ω_s in specific circumstances.

3.2 KIC 12508433

Our mock data experiments confirm that a realistic measure of surface rotation rate, treated as a prior during inference can better constrain the internal rotation profile. We now apply this method to observed rotational splittings of KIC 12508433 (Deheuvels et al. 2014). First with a uniform prior on surface rotation between 0 and 600 nHz, and then with an independent surface rotation rate (measured by Garcia et al. 2014, from photometry) treated as a Gaussian prior on the surface rotation rate with mean 172 nHz and standard deviation 21 nHz. The posteriors are shown in Figs 4 and 5. The best-fitting values and credible intervals of the rotation profile parameters for each prior are shown in Table 2 and are compared to the results of optimally localized average (OLA) inversions performed in Deheuvels et al. (2014).

With a uniformed prior, the median of the posterior on the core and surface rotation rates and corresponding 16th and 84th percentile credible intervals are $\Omega_c/2\pi = 524^{+36}_{-34}$ nHz and $\Omega_s/2\pi = 141^{+51}_{-79}$ nHz, with the maximum a posteriori or MAP point at $\Omega_c/2\pi \approx 520$ nHz and $\Omega_s/2\pi \approx 170$ nHz. With the informed surface rotation rate prior the 16th and 84th percentile credible intervals are $\Omega_c/2\pi = 525^{+39}_{-35}$ nHz and $\Omega_s/2\pi = 175^{+19}_{-21}$ nHz. The inferences agree with each other, as well as the inversions performed in Deheuvels et al. (2014). Those authors use OLA to estimate the mean rotation rate in the g-mode cavity to be $\langle \Omega_g \rangle/2\pi = 532 \pm 79$ nHz and the mean rotation rate in the p-mode cavity to be $\langle \Omega_p \rangle/2\pi = 213 \pm 26$ nHz. Taking their Ω_g and Ω_p as analogues for Ω_c and Ω_s , respectively, both sets of quantities agree within about one joint standard deviation, without considering that the *mode* of the Ω_s posteriors are closer to $\langle \Omega_p \rangle$ than the median of Ω_s .

Like in the mock data experiments, the independent surface rotation measure removed support for discontinuities close to the BCZ (comparing Figs 4 and 5), but two peaks remain: $p \approx 0.25$ (closest to the median posterior value and a peak in the posterior when considering a flat prior on Ω_s) and a much smaller peak closer to the core. Rotation profiles with a discontinuity located $p > 0.4$ for KIC 12508433 is strongly disfavoured, and a discontinuity in the radiative region $0.2 r/R$ is favoured. Comparing the confidence intervals when applying a flat and informed prior, we obtain a factor of approximately two increase in measurement accuracy on p .

4 DISCUSSION

We find that a surface rotation rate measured from star spot modulations can substantially improve inferences on the rotation profiles of low-luminosity subgiants. This takes advantage of a degeneracy between Ω_s and p , found by performing inference using mock experiments with different discontinuity positions.

Including an independent measure of surface rotation as a prior in the analysis of KIC 12508433 yields increased support for step-like profiles with rotational gradients in the radiative zone and decreased support for step-like rotation profiles with $p \gtrsim 0.4$.

In our mock data tests, we proposed that a step-like rotation profile with a rotational gradient at 0.5 r/R (BCZ profile) is motivated by, but not representative of, angular momentum transport by fossil

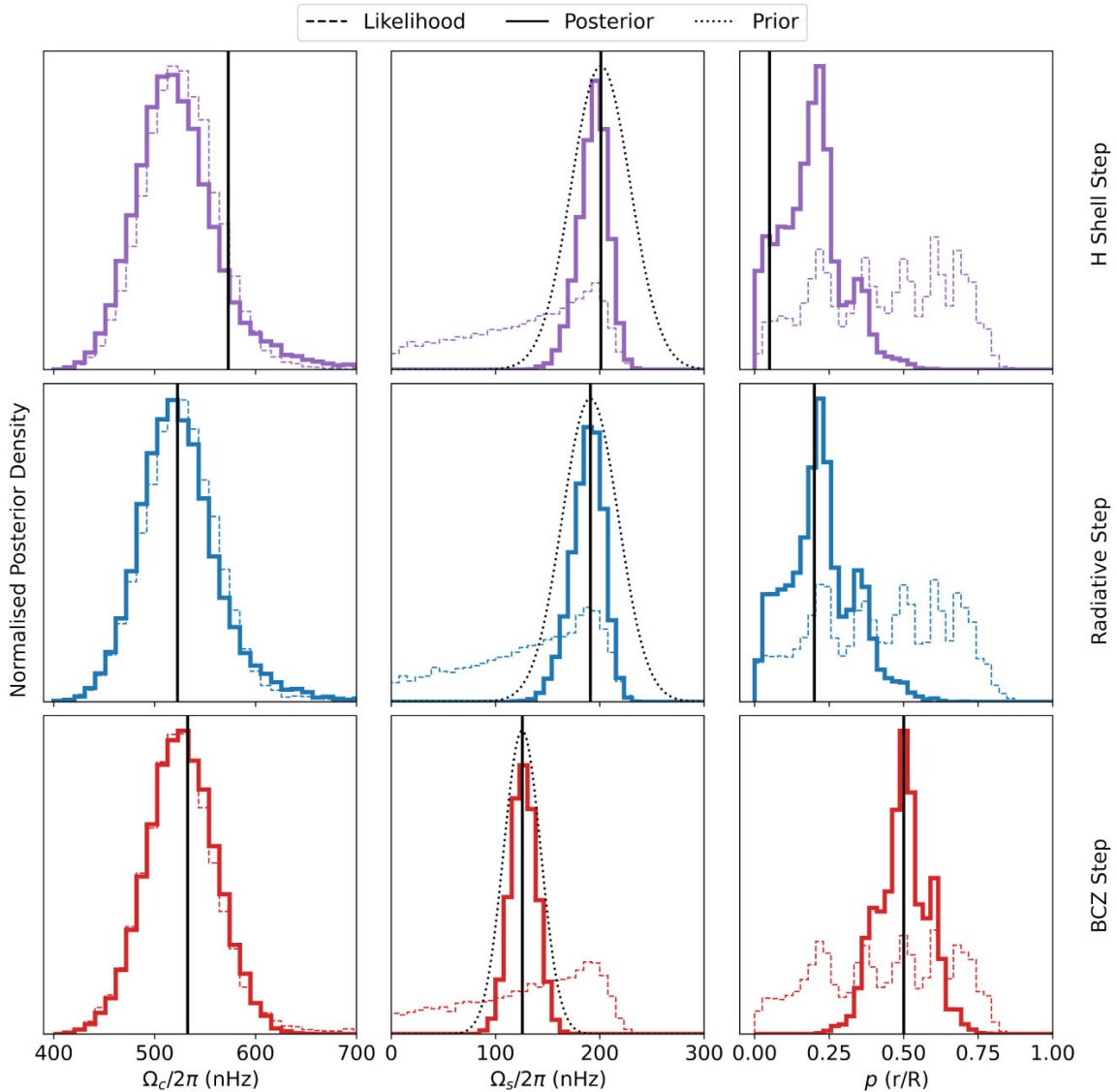


Figure 3. Normalized posterior density following sampling for each *mock* rotational splitting experiment. From left to right, the normalized posterior density of each of the parameters of the rotation profile model are shown: surface rotation rate ($\Omega_s/2\pi$), core rotation rate ($\Omega_c/2\pi$), and position of rotational gradient (p). Thin coloured dashed lines are samples with no prior on the surface rotation rate, thin dotted black lines correspond to the introduced prior on surface rotation rate, and thick coloured lines correspond to samples when the informed surface rotation prior was introduced. Vertical black lines correspond to the input values for each of the rotation profile parameters used to generate the mock rotational splittings. From top to bottom, each row displays the result of sampling a different set of rotational splittings with the same colours as the rotation profiles used to generate the mock data in Fig. 2: the H-burning shell step (purple), radiative zone step (blue), and base of BCZ step (red).

magnetic fields. However, the simplified step rotation profile does not accurately recreate the inverse dependency of rotation rate with radius beyond the BCZ indicative of this angular momentum transport process. Further, the signature rotation profile becomes most apparent in the red giant branch (Fellay et al. 2021; Takahashi & Langer 2021). Therefore, we are not proposing a lack of support for eliminating fossil magnetic fields as a possible explanation for the subgiant angular momentum transport problem.

The auxiliary measure of surface rotation we adopt as a surface rotation rate prior requires some discussion. The ‘data’ we use are

rotational splitting frequencies measured from a Fourier transform of a photometric time series. The measured surface rotation rate from Garcia et al. (2014) also uses some subset of the same photometric time series data. The two sets of measurements are not strictly statistically independent, such that there is a risk that we are ‘stealing information’. The two approaches do use subsets of the same data set, but the methods are sufficiently distinct that we consider it reasonable to use the surface rotation rate here.

Santos et al. (2021) suggest that the average percentage uncertainty on photometric surface rotation measurements is ~ 10 per cent

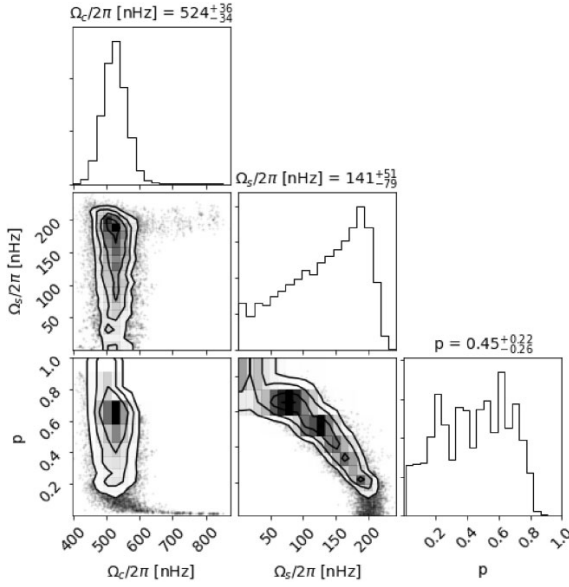


Figure 4. Posterior distributions of the core rotation rate Ω_c , the surface rotation rate Ω_s , and the discontinuity position p (equation 4) given the observed $l = \{1, 2\}$ rotational splittings of KIC 12508433 and assuming a rotation profile with a step function.

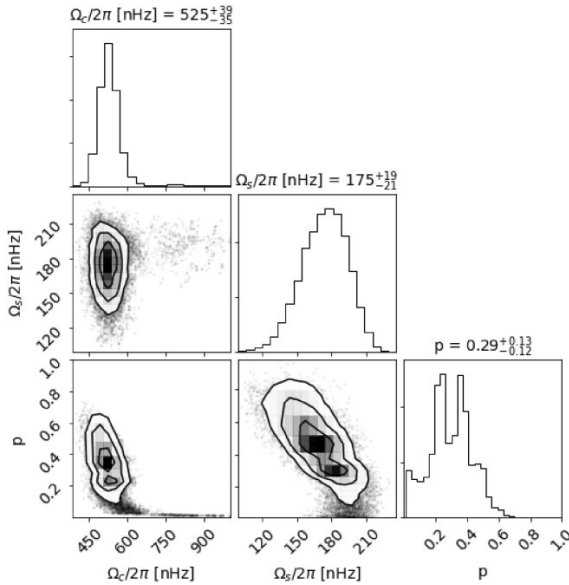


Figure 5. Posteriors on step profile parameters given the rotational splittings of KIC 12508433 and informed prior on surface rotation rate from (Garcia et al. 2014).

for MS and subgiant stars. The precision varies with temperature, and peaks around 6000 K (the Kraft break). Those authors also concluded that only about 20 per cent of subgiants with long and precise photometric observations from *Kepler* have measurable rotation periods. Subgiants may express smaller, shorter-lived active regions, which, when combined with long rotation periods, would present a smaller observable fraction and less precise measures of

Table 2. Best-fitting rotation profile parameters given observed $\ell = 1$ and 2 rotational splittings of KIC 12508433 from optimally localized averages (OLA; Deheuvels et al. 2014) and forward modelling with flat and informed ($\Omega_s/2\pi = 172 \pm 21$ nHz) priors. OLA does not place constraints on the rotation profile outside the g- and p-mode cavities in the core and at the star's surface, respectively. p is more precisely measured with the introduction of the informed prior when forward modelling.

	$\Omega_c/2\pi$ (nHz)	$\Omega_s/2\pi$ (nHz)	$p (r/R)$
Deheuvels et al. (2014) (OLA)	532 ± 79	213 ± 26	–
Sampling – flat Ω_s , Prior	524^{+36}_{-34}	141^{+51}_{-79}	$0.45^{+0.22}_{-0.26}$
Sampling – informed Ω_s Prior	525^{+39}_{-35}	175^{+19}_{-21}	$0.29^{+0.13}_{-0.12}$

the surface rotation rate when compared to MS counterparts. On the other hand, observing rotational splittings in subgiants requires a long observation time, which may lend itself to a higher fraction with measurable surface rotation rates.

It's difficult to precisely measure the surface rotation rate without using photometry. Rotational velocity ($v\sin i$) only requires a single high-resolution spectrum, but requires an estimate of the inclination angle and the star's radius, which is quickly changing in the post-MS and is strongly model dependent.

We assumed a step-like (discontinuous) function for the rotation profile, consistent with other works (e.g. Fellay et al. 2021). Realistically, this may not reflect the true shape of the rotation profile of any low-luminosity subgiant. Asteroseismic forward modelling of the stellar rotation profile is an ill-posed problem. The observed rotational splittings alone do not uniquely determine the shape of a star's rotation profile. An assumption of the rotation profile's shape is necessary for the rotational splittings to constrain the range of possible rotation profile parameters. A much more flexible model than the step-like rotation profile could be employed. However, the inferences must be interpreted in the context of the realistic evolution of angular momentum transport. Ultimately, our work exemplifies that introducing an informed surface rotation prior further reduces the potential rotation profiles already constrained by asteroseismic data. Combining state-of-the-art asteroseismic and surface rotation data is a practical method to obtain more substantial constraints to the evolution of rotation from already available data.

In this work, we take KIC 12508433 as an example of a low-luminosity giant with asteroseismic observations. It is not yet clear whether the degeneracy between surface rotation and step position generalises across all subgiants of different masses, metallicities, and ages. Very few subgiants are known to have mode measurements suitable for this kind of inference. Further work is needed.

5 CONCLUSIONS

We investigate the impact of independent surface rotation rate priors on inference of the rotation profile of subgiant stars. We perform forward modelling of the rotation profile given observations of rotational splittings assuming a step function rotation profile. Under these assumptions, we identify a degeneracy between the surface rotation rate and the position of the strong gradient. Mock experiments show that the introduction of a prior on surface rotation breaks the degeneracy, allowing us to place stronger constraints on the position of the gradient.

We introduce an independent measure of surface rotation from star spot photometric modulations as a prior when performing inference on the rotation profile of KIC 12508433. We find that introducing the independent measure of surface rotation increases the measurement precision on the position of the rotational gradient by a factor of 2 and

that the data strongly disfavours discontinuities outside $r/R = 0.4$ in KIC 12508433. Including auxiliary surface rotation measurements when performing asteroseismic forward modelling of the rotation profile is a simple way of extending what we can learn from each star with existing data.

ACKNOWLEDGEMENTS

We thank the anonymous referee for their thorough review of this work and for their helpful suggestions. ARC is supported in part by the Australian Research Council through a Discovery Early Career Researcher Award (DE190100656). Parts of this research were supported by the Australian Research Council Centre of Excellence for All Sky Astrophysics in 3 Dimensions (ASTRO 3D), through project number CE170100013. IM acknowledges support from the Australian Research Council Centre of Excellence for Gravitational Wave Discovery (OzGrav), through project number CE170100004. IM is a recipient of the Australian Research Council Future Fellowship FT190100574. WHB thanks the UK Science and Technology Facilities Council (STFC) for support under grant ST/R0023297/1. This work has received funding from the European Research Council (ERC) under the European Union's Horizon 2020 research and innovation programme (CartographY GA 804752). Funding for the Stellar Astrophysics Centre is provided by The Danish National Research Foundation (grant agreement no. DNRF106).

DATA AVAILABILITY

The data and models underlying this article are available upon request to the corresponding author.

REFERENCES

- Aerts C., Christensen-Dalsgaard J., Kurtz D. W., 2010, *Asteroseismology*. Springer, Dordrecht
- Arlt R., Hollerbach R., Rüdiger G., 2003, *A&A*, 401, 1087
- Baglin A., 2003, *Adv. Space Res.*, 31, 2,345
- Balbus S., Hawley J., 1994, *MNRAS*, 266
- Ball W. H., Gizon L., 2014, *A&A*, 568, A123
- Ball W. H., Gizon L., 2017, *A&A*, 600, A128
- Benomar O. et al., 2013, *ApJ*, 767, 158
- Borucki W. J. et al., 2010, *Science*, 327, 977
- Cantiello M., Mankovich C., Bildsten L., Christensen-Dalsgaard J., Paxton B., 2014, *ApJ*, 788, 93
- Casagrande L., Ramirez I., Melendez J., Bessell M., Asplund M., 2010, *A&A*, 512, A54
- Ceillier T., Eggenberger P., García R. A., Mathis S., 2013, *A&A*, 555, A54
- Charbonnel C., Talon S., 2005, *Science*, 309, 2189
- Christensen-Dalsgaard J., 2008, *Astrophys. Space Sci.*, 316, 113
- Deheuvels S. et al., 2014, *A&A*, 564, A27
- Deheuvels S., Ballot J., Beck P. G., Mosser B., Østensen R., García R. A., Goupil M. J., 2015, *A&A*, 580, A96
- Deheuvels S., Ballot J., Eggenberger P., Spada F., Noll A., Hartogh J. W. d., 2020, *A&A*, 641, A117
- Di Mauro M. P., Ventura R., Corsaro E., Moura B. L. D., 2018, *ApJ*, 862, 9
- Eggenberger P., Montalbán J., Miglio A., 2012, *A&A*, 544, L4
- Eggenberger P. et al., 2019, *A&A*, 621, A66
- Fellay L., Buldgen G., Eggenberger P., Khan S., Salmon S. J. A. J., Miglio A., Montalbán J., 2021, *A&A*, 654, A133
- Fuller J., Cantiello M., Stello D., Garcia R. A., Bildsten L., 2015, *Science*, 350, 423
- Garaud P., 2002, *MNRAS*, 335, 707
- Garcia R. A. et al., 2014, *A&A*, 572, A34
- Gehan C., Mosser B., Michel E., Samadi R., Kallinger T., 2018, *A&A*, 616, A24
- Gough D. O., 2015, *Space Sci. Rev.*, 196, 15
- Gough D. O., Thompson M. J., 1990, *MNRAS*, 242, 25
- Heger A., 1998, PhD thesis, Technical University of Munich
- Hermes J. J., Kawaler S. D., Bischoff-Kim A., Provencal J. L., Dunlap B. H., Clemens J. C., 2017, *ApJ*, 835, 277
- Hoffman M. D., Gelman A., 2011, arXiv e-prints, [arXiv:1111.4246](https://arxiv.org/abs/1111.4246)
- Kissin Y., Thompson C., 2015, *ApJ*, 808, 35
- Li Y., Bedding T. R., Li T., Bi S., Stello D., Zhou Y., White T. R., 2020, *MNRAS*, 495, 2363
- Maeder A., Meynet G., 2000, *Ann. Rev. Astron. Astrophys.*, 38, 143
- Marques J. P. et al., 2013, *A&A*, 549, A74
- McQuillan A., Mazeh T., Aigrain S., 2014, *ApJS*, 211, 24
- Menou K., Mer J. L., 2006, *ApJ*, 650, 1208
- Noll A., Deheuvels S., Ballot J., 2021, A187 *A&A*, 647
- Ouazzani R.-M., Marques J. P., Goupil M.-J., Christophe S., Antoci V., Salmon S. J. A. J., 2019, *A&A*, 626, A121
- Paxton B., Bildsten L., Dotter A., Herwig F., Lesaffre P., Timmes F., 2010, *ApJS*, 192, 3
- Paxton B. et al., 2013, *ApJS*, 208, 4
- Paxton B. et al., 2015, *ApJS*, 220, 15
- Paxton B. et al., 2019, *ApJS*, 243, 10
- Pinçon C., Belkacem K., Goupil M. J., Marques J. P., 2017, *A&A*, 605, A31
- Salvatier J., Wiecki T. V., Fonnesbeck C., 2016, *PeerJ Comput. Sci.*, 2, e55
- Santos A. R. G., Breton S. N., Mathur S., García R. A., 2021, *ApJS*, 255, 17
- Schunker H., Schou J., Ball W. H., 2016, *A&A*, 586, A24
- Spada F., Gellert M., Arlt R., Deheuvels S., 2016, *A&A*, 589, A23
- Strugarek A., Brun S., Zahn J., 2011, *A&A*, 532, A34
- Takahashi K., Langer N., 2021, *A&A*, 646, A19
- Unno W., Osaki Y., Ando H., Saio H., Shibahashi H., 1989, Nonradial Oscillations of Stars, <https://ui.adsabs.harvard.edu/abs/1989nos.book....U>

APPENDIX A: SAMPLING RESULTS

Here, we provide the posteriors following sampling of each set of rotational splittings.

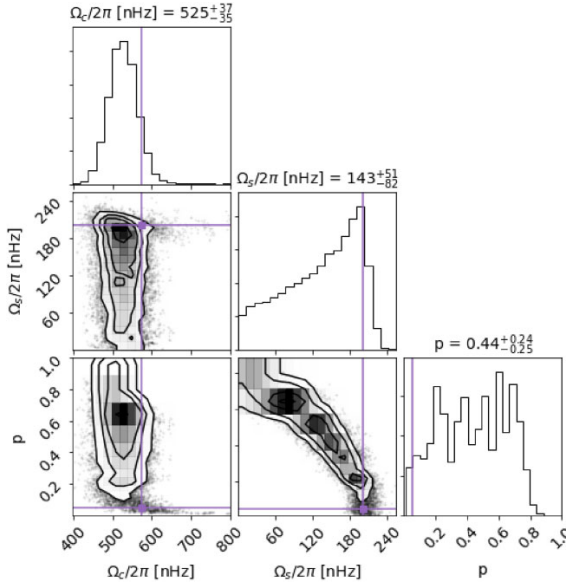


Figure A1. Posterior distributions using mock data generated with a step function aligned with the H burning shell ($r/R = 0.05$, purple profile in Fig. 2). True values are indicated in purple. There is considerable multimodality and degeneracy present.

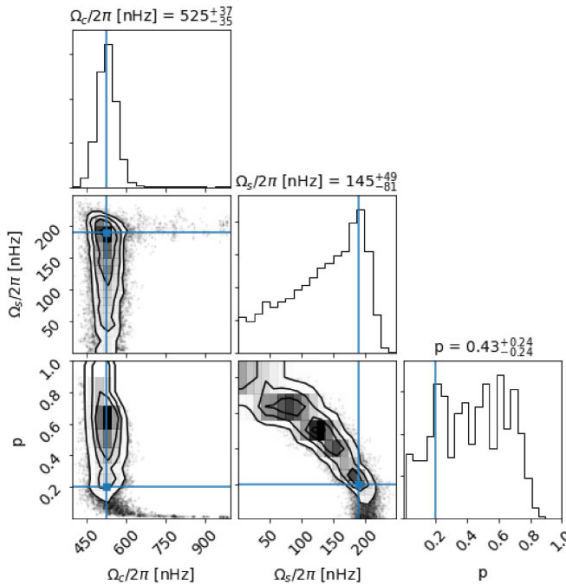


Figure A2. Posterior distributions using mock data generated with a step function in the radiative region ($r/R = 0.2$, blue profile in Fig. 2) and realistic uncertainties. True values in blue.

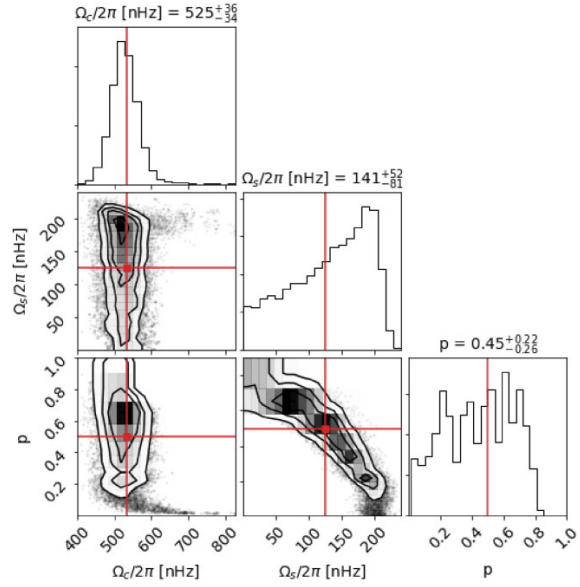


Figure A3. Posterior distributions using mock data generated with a step function at the BCZ ($r/R = 0.5$; red profile in Fig. 2), and realistic uncertainties. True values in red.

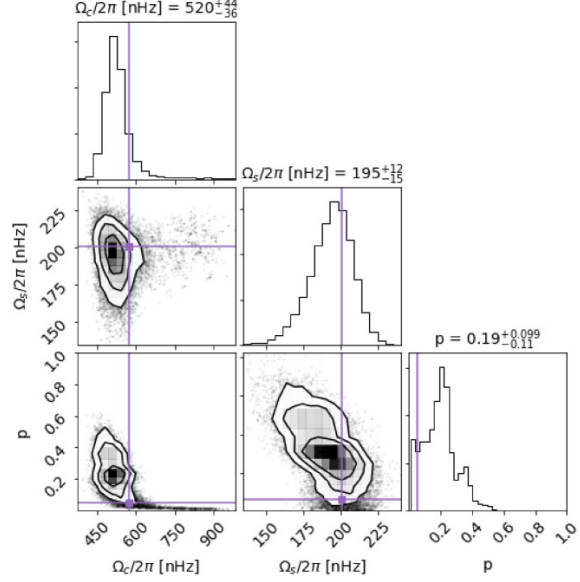


Figure A4. Posterior distributions using mock data generated with a step profile at the g-mode cavity ($r/R = 0.05$; purple profile in Fig. 2), with realistic uncertainties, and a 10 per cent prior on surface rotation Ω_s . There is still degeneracy between p and the rotation parameters (e.g. Fig. A1), but the prior has collapsed all other modes.

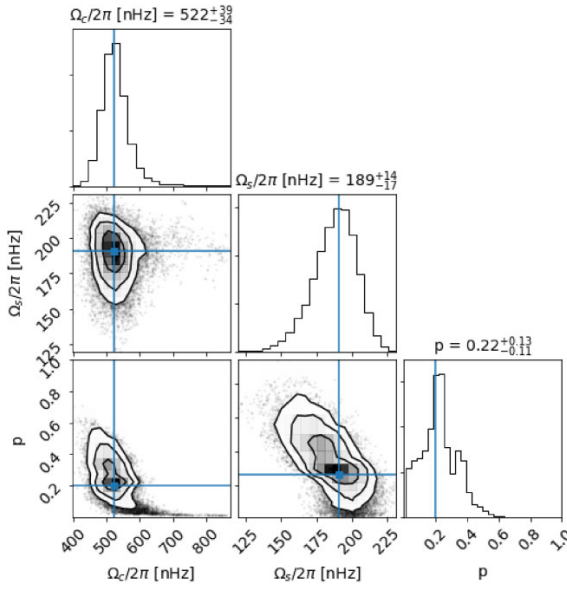


Figure A5. Posterior distributions using mock data generated with a step profile in the radiative region ($r/R = 0.20$; blue profile in Fig. 2), with realistic uncertainties, and a 10 per cent prior on surface rotation Ω_s (compare with Fig. A2).

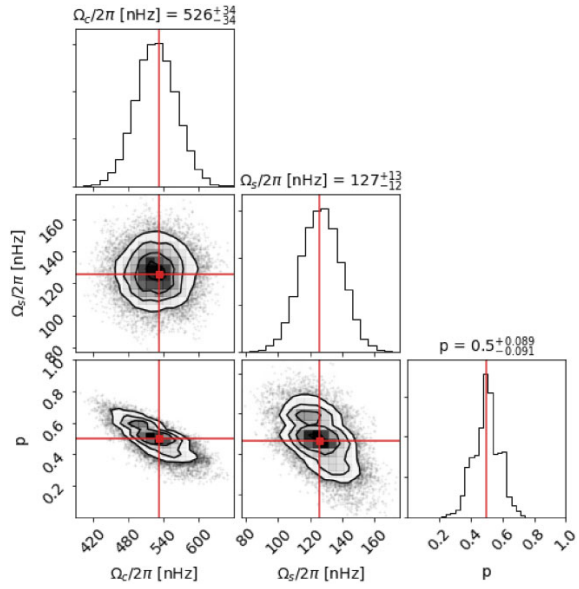


Figure A6. Posterior distributions using mock data generated with a step profile at the BCZ ($r/R = 0.50$; red profile in Fig. 2), with realistic uncertainties, and a 10 per cent prior on surface rotation Ω_s (compare with Fig. A3).

This paper has been typeset from a $\text{\TeX}/\text{\LaTeX}$ file prepared by the author.

Chapter 3

Stellar spots cause measurable variations in atmospheric metallicity

Preamble

This chapter was originally published as:

[Wilson & Casey \(2023\)](#)

Stellar spots cause measurable variations in atmospheric metallicity

Tanner A. Wilson ^{1,2*} and Andrew R. Casey ^{1,2}

¹School of Physics & Astronomy, Monash University, Clayton, 3800, Victoria, Australia

²Center of Excellence for Astrophysics in Three Dimensions (ASTRO-3D), Australia

Accepted 2023 June 19. Received 2023 June 19; in original form 2023 May 21

ABSTRACT

To accurately measure a star’s atmospheric parameters and chemical abundances, it is crucial to have high-quality spectra. Analysing the detailed chemical abundances of groups of stars can help us better understand nucleosynthesis, galactic chemical enrichment, and stellar evolution. In this study, we explored whether stellar spots can affect a star’s inferred metallicity and, if so, where the impact is the strongest. To investigate this, we created synthetic infrared spectra that included stellar spots for a sample of main-sequence stars younger than the sun. We then applied two models to the data: one that accounted for spots and the other that did not. From this, we can determine the bias introduced when fitting spotted spectra with a non-spotted model and how this bias varies with different parameters. Our findings revealed that fitting spotted spectra with a non-spotted model can introduce a scatter of up to 0.05 dex in the inferred metallicity, especially for stars with high levels of spot coverage. This bias is similar in magnitude to other relevant effects, such as atomic diffusion, radiative levitation, or non-local thermodynamic equilibrium. We also found that the effect is most pronounced in young stars and decreases with age. These results suggest that stellar spots can introduce a systematic uncertainty in metallicity that is not currently accounted for in spectroscopic analysis. This could potentially limit scientific inferences for population-level studies of young stars and differential abundance analyses.

Key words: stars: abundances – stars: rotation – star-spots.

1 INTRODUCTION

It is widely assumed that the elemental abundances in a star’s atmosphere accurately reflect the abundances of the material from which the star formed (Gibson et al. 2003; Pagel 2009; Salaris & Cassisi 2017). This assumption is critical for chemical tagging (Anders et al. 2016; Randich et al. 2022), understanding galactic formation (Gibson et al. 2003), and the synthesis of elements across cosmic time (McWilliam & Rauch 2004; Johnson, Fields & Thompson 2020). Precise measurements of elemental abundances are essential in many areas of astrophysics. For example, chemical tagging allows us to track the history of the Galaxy, which would be impossible with biased measures of abundance. Differential abundance techniques (Önehag et al. 2011; Meléndez et al. 2014; Reggiani et al. 2016; Maia et al. 2019; Liu et al. 2020; Nissen et al. 2020; Spina et al. 2021) – employed for solar twins and planet-hosting stars – claim very precise abundance measurements, which are essential for probing planet formation (Tayar et al. 2022). Similarly, when determining cluster ages (Bensby, Feltzing & Lundström 2004; Pont & Eyer 2004), the turn-off age of a star is particularly useful for this purpose because a small change in colour/magnitude, which depends on metallicity, indicates a relatively large change in age compared to the main sequence (MS).

Recognising that surface abundances may change over a star’s evolution is important. The surface abundances can change due to numerous processes. Atomic diffusion and radiative levitation introduce surface abundance variations on the scale of 0.05 dex, with

a magnitude and bias that depends on the element and the stellar effective temperature (Önehag, Gustafsson & Korn 2014). Enhanced mixing can also cycle material to the surface. Nuclear reactions, such as lithium depletion (Pinsonneault et al. 2002) or CNO cycling (Crowther 2007) enhance and deplete specific surface abundances and isotopic ratios. Accretion can enhance surface metallicity and vary particular elemental abundances for a short time depending on the companion type (Laughlin & Adams 1997; Pasquini et al. 2007; Maldonado et al. 2019). For example, mass-loss can strip away H-rich surface regions in Wolf–Rayet stars (Crowther 2007) – increasing the observed stellar metallicity or carrying away surface metals that will have a small to negligible decrease of surface metals on the main sequence.

These effects are usually ignored when estimating a star’s stellar parameters and chemical abundances. Most spectroscopic analyses usually adopt some simplifying assumptions to make the computation time tractable. For example, we usually assume the stellar photosphere can be represented in one dimension (1D) and that baryonic matter can be described by thermal distributions in small regions (local thermal equilibrium). These assumptions can particularly influence the measured stellar parameters (e.g. Blanco-Cuaresma 2019). Both can lead to an overestimate of the temperature gradient in the atmosphere and an underestimation of the density, which can result in an overestimate of the abundance. We also typically ignore magnetic activity, but recently Spina et al. (2020) showed it has a measurable impact on the chemical abundances of young, fast-rotating stars. While these assumptions simplify inference, it is important to consider their effects when reaching conclusions.

* E-mail: tanner.wilson@monash.edu

Stars have spots, which are important indicators of the rotational rate of stars, especially along the main sequence (McQuillan, Mazeh & Aigrain 2014; Santos et al. 2021). The properties of stellar spots and their effect on the observed properties of a star vary with age, rotation rate, mass, and metallicity (Mathur et al. 2014; Karoff et al. 2018; Nichols-Fleming & Blackman 2020). For example, as the rotation rates of stars decrease with age, the average magnetic activity likewise decreases. This results in smaller short-lived spots that cover only a small fraction of the stellar surface (Cao & Pinsonneault 2022). Spot properties can be generalized by: their coverage across the stellar surface, the temperature difference relative to the surrounding, and the occurrence pattern. Cao & Pinsonneault (2022) recently quantified the spot parameters of stars in the Pleiades and M67. They found that young or fast-rotating stars tend to be more magnetically active and have a greater spot coverage than their older, slower counterparts.

The spotted areas of the star can be thousands of degrees cooler than the surrounding areas – solar spots for example can be 500–2000 K cooler than the surrounding photosphere (Berdyugina 2005; Herbst et al. 2020). A spotted star’s stellar spectra are more complex than their non-spotted counterparts (Morris et al. 2019). Accurate inference of stellar parameters requires a model that reflects the stellar spectra well. In this work, we quantify the effect of fitting spotted spectra with non-spotted models and identify the parts of the main sequence where the effect is most prevalent. In Section 2, we outline the generative model for stellar spectra with spots and describe our choices of stellar parameters before outlining the fitting procedure used. In Section 3, we present the difference in the recovered stellar parameters with the spotted and non-spotted models. We discuss parts of the main sequence where the effect is most prevalent. Finally, in Section 4, we place those results in the context of other significant effects on measured stellar metallicity and provide recommendations for high-precision spectroscopic investigations in specific regions of stellar evolution.

2 METHOD

2.1 Stellar parameters for a population of fake stars

We prepare a sample of stellar spectra that spans the main sequence to estimate the impact that stellar spots can have on the accuracy of inferred stellar parameters. This sample is intended to be indicative of a possible population of main-sequence stars but not intended to represent which stars would, or would not, have spots. We generate 1500 spectra of main-sequence and early post-main-sequence stars with various values of mass, age, metallicity, $v\sin i$, f_{spot} , and x_{spot} across the HR diagram. We drew masses from a Salpeter initial mass function (Salpeter 1955) between 0.5 and 1.5 M_{\odot} with $\alpha = 2.35$. This limits our range of masses to those with a radiative surface and convective core and reaches beyond the Kraft break (Kraft 1967). Metallicity is drawn from a distribution to approximately reflect what is observed in the Milky Way. Specifically, we defined a variable ϕ to be drawn from a Beta distribution

$$\phi \sim \mathcal{B}(\alpha = 10, \beta = 2) \quad (1)$$

and applied a transform from ϕ to [Fe/H] by requiring the metallicities be bounded between $[\text{Fe}/\text{H}]_{\min} = -2$ and $[\text{Fe}/\text{H}]_{\max} = +0.5$. We also required that the mode of ϕ , defined as $\frac{\alpha-1}{\alpha+\beta-2}$ for a Beta distribution, occurs at Solar metallicity. This leads to the transform:

$$[\text{Fe}/\text{H}] = \left([\text{Fe}/\text{H}]_{\max} - [\text{Fe}/\text{H}]_{\min} \right) \left(\phi - \frac{\alpha-1}{\alpha+\beta-2} \right). \quad (2)$$

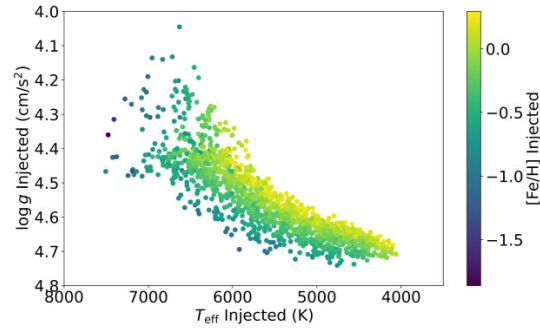


Figure 1. HR diagram of the 1500 sets of stellar parameters drawn from physically motivated distributions of mass, metallicity, and age coloured by [Fe/H].

The stars we generate mock data for in this work span from the zero-age main sequence (ZAMS) to low-luminosity subgiants. We draw equivalent evolutionary phase (EEP) values from a uniform distribution $\text{EEP} \sim \mathcal{U}(200, 450)$, where $\mathcal{U}(x, y)$ denotes a uniform prior between x and y . The bounds of this range (200 and 450) represent the ZAMS and the low-luminosity subgiant phase, respectively. Using the EEP, mass, and metallicity, we interpolate a position along the MIST stellar isochrones (Morton 2015) to calculate the expected T_{eff} and $\log g$ for each random star. We also obtain the star’s age (post-ZAMS) that we can use in conjunction with the other stellar parameters to determine rotational properties (see below). We have limited the age of the stars we consider in this work up to the age of the Sun. This is the range available for rotational rate and convective turnover time-scales from the sources we draw from in this work. This limits the post-MS stars we consider to more massive stars. We briefly discuss bias’ that may introduce in Section 4. In Fig. 1, we show Hertzsprung-Russell diagram of the synthetic sample of stars investigated in this work coloured by their metallicity.

The surface rotation period is interpolated from stellar cluster-tuned rotational isochrones given the stellar age and mass (table A1 in Spada et al. 2016). Rotational broadening $v\sin i$ can then be calculated by combining the rotational period, the radius from the interpolated isochrone model, and an inclination angle. We have drawn inclination from a uniform distribution in $\cos i \sim \mathcal{U}(0, 1)$.

f_{spot} is related to the Rossby number, Ro , which is defined as the ratio of the surface rotational period to the convective turnover time-scale (τ_{conv}). τ_{conv} is interpolated from Table 1 in Landin, Mendes & Vaz (2010) given the stellar age and mass. Combining this value with the rotational period, we obtain Ro . f_{spot} is then calculated from the relationship between f_{spot} and Ro identified in Cao & Pinsonneault (2022) (equation 5):

$$f_{\text{spot}} = \begin{cases} 0.278, & \log Ro \leq -0.729 \\ 0.0623 Ro^{-0.881}, & \log Ro > -0.729 \end{cases}. \quad (3)$$

There is some scatter in f_{spot} that is not accounted for by this relation (see left-hand panel of fig. 7 in Cao & Pinsonneault 2022). For this reason, we add random noise to our calculated f_{spot} that is drawn from a normal distribution with a mean of 0 standard deviation of 0.1.

We assume x_{spot} is drawn from a uniform distribution $x_{\text{spot}} \sim \mathcal{U}(0.8, 1.0)$. This represents the limits set when fitting x_{spot} in Cao & Pinsonneault (2022), which is motivated by temperature bounds which they discuss in more detail in Section 2.2. x_{spot} does not appear to have a clear relationship with other stellar parameters, but it –

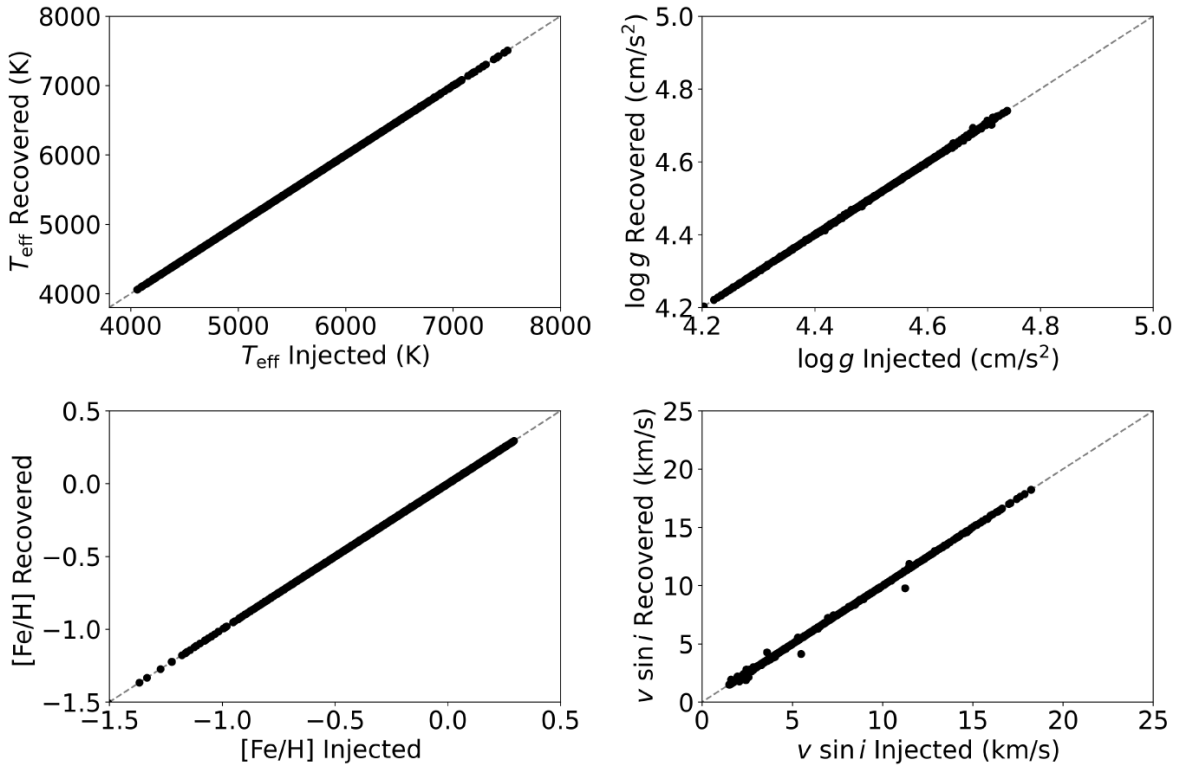


Figure 2. Recovered traditional stellar parameters (T_{eff} , $\log g$, $[\text{Fe}/\text{H}]$, and $v \sin i$) from fitting synthetic spotted spectra with a spotted model of the stellar atmosphere against the corresponding injected parameters. We consistently accurately recover each injected value when a spotted model of the stellar atmosphere is employed to fit the spotted synthetic spectra.

and f_{spot} – may vary on multiple periodic time-scales as they do for the Sun. The stochastic nature of stellar observations – and the admittedly simple nature of the model – means that f_{spot} and x_{spot} are random draws from the possible stellar spot parameters. We will eventually find that x_{spot} has little effect on the bias introduced by fitting spotted spectra with a non-spotted model, so move forward with the knowledge that we have good coverage when modelling over the range of possible parameters.

2.2 Spotted spectrum generative model

We build upon the work of Cao & Pinsonneault (2022), where a forward model is developed to model the effect of star-spots and to estimate the fractional spot coverage of stars in the Pleiades and M67. Their model assumes that the spectrum of a spotted star can be broken into spotted and non-spotted components. These two components have the same $\log g$, $[\text{Fe}/\text{H}]$, microturbulent velocity, and the same surface rotational velocity ($v \sin i$), but the two components vary in temperature. The spot and ambient temperatures (T_{spot} and T_{amb}) are related by $T_{\text{spot}} = x_{\text{spot}} T_{\text{amb}}$, and are coupled to the effective temperature of the star following the approach of Somers & Pinsonneault (2015):

$$T_{\text{eff}} = T_{\text{amb}}(1 - f_{\text{spot}} + f_{\text{spot}}x_{\text{spot}}^4)^{\frac{1}{4}}, \quad (4)$$

where f_{spot} is the fractional surface spot coverage. From these relations, the set $\{T_{\text{eff}}, x_{\text{spot}}, f_{\text{spot}}\}$ define a pair of ambient and spot temperatures that preserve stellar luminosity.

We calculated a grid of synthetic spectra, which we interpolate between to generate the predicted spectra for a spotted or non-spotted model. The list of atomic and molecular transitions is from (Shetrone et al. 2015; Smith et al. 2021). We used a grid of plane-parallel MARCS (Gustafsson et al. 2008) model photospheres that span dimensions in effective temperature, surface gravity, and metallicity.¹ Microturbulence was kept fixed at 1.15 km s^{-1} for main-sequence stars and we assumed that $[\alpha/\text{H}]$ scales with $[\text{Fe}/\text{H}]$ (i.e. the so-called standard composition in MARCS). The abundance dimensions $[\text{C}/\text{M}]$ and $[\text{N}/\text{M}]$ were kept fixed at zero. We used Korg (Wheeler et al. 2022) to synthesize all model spectra at high resolution, which we then convolved and down-sampled to match the (uniform in log) pixel spacing used in the APOGEE data reduction pipeline (Holtzman et al. 2018). The convolution kernel includes two components that enter multiplicatively: one assuming a constant spectral resolution $R = \lambda/\Delta\lambda$ of 22 500, and another representing rotational broadening $v \sin i$. We convolved each spectrum with a grid of $v \sin i$ values that were uniformly spaced in $\log v \sin i$ from 0 to 100 km s^{-1} in order to match the set-up for the APOGEE analysis pipeline. Naturally, for low $v \sin i$ values, the line spread function of the instrument will dominate.

With this grid of spectra and some given spectral parameters $\{T_{\text{eff}}, \log g, [\text{Fe}/\text{H}], \log v \sin i\}$, we interpolate the spotted and ambient

¹We calculated spectra using spherical models as well, but in practice, only spectra from plane-parallel models (i.e. main-sequence stars) are used in this work.

spectra and combine them in a fractional manner with wavelength as if they were separate blackbody spectra in order to produce a flux-preserving combined spectrum:

$$B(T_{\text{eff}}, \lambda) = f_{\text{spot}} B(T_{\text{spot}}, \lambda) + (1 - f_{\text{spot}}) B(T_{\text{amb}}, \lambda). \quad (5)$$

In total, our forward model for predicting spotted spectra includes six parameters: T_{eff} , $\log g$, $[\text{Fe}/\text{H}]$, $\log v \sin i$, x_{spot} , and f_{spot} . This model is equally capable of predicting non-spotted spectra by fixing f_{spot} to zero or x_{spot} to unity.

Using the 1500 sets of parameters outlined in Section 2.1, we generated synthetic spotted stellar spectra. We also apply realistic noise at each pixel from a Gaussian distribution with standard deviation = 0.01, assuming a signal-to-noise ratio of 100. Continuum normalization is performed by assuming a running mean of the spectra, and during fitting, this procedure is applied to the fake spectrum (data) and to the model spectrum.

We now have the tools to determine the effect of fitting spotted spectra with non-spotted models. We do this by finding the best-fitting stellar parameters given the synthetic spectra fitted twice: first with the model described in Section 2.2 and then with a non-spotted model (e.g. f_{spot} fixed at 0 and x_{spot} fixed at 1). Here, we have performed least-squares fitting through the Levenberg–Marquardt algorithm implemented in SCIPY. We found that fitting the spotted parameters can be non-trivial. The likelihood surfaces are multimodal and degenerate, requiring informed choices about the initialization of fitting. To resolve this issue, we performed a coarse evaluation of parameters (on a grid) before starting optimization.

3 RESULTS

We began by confirming that we could accurately recover the injected parameters. The best-fitting parameters following fitting the synthetic spotted spectra with a spotted model are shown in Figs 2 and 3. T_{eff} , $\log g$, $[\text{Fe}/\text{H}]$, and $v \sin i$ are recovered accurately for every injected parameter set. While we identify scatter in recovered f_{spot} this appears not to affect the accuracy of the recovery of the traditional stellar parameters. We move forward confident that any difference in the recovered parameters between fitting with the spotted and non-spotted models results from the model differences rather than the fitting procedure employed in this work.

We now identify systematic effects in the recovered parameters when we fit the spotted spectra with an incorrect model of non-spotted spectra. The difference between the recovered parameters fitted with a spotted and non-spotted model of the stellar atmosphere are shown in Fig. 4. A consistent scatter is introduced on each parameter when a non-spotted model is used to perform inference on a spotted spectrum. We calculate each parameter’s average bias and scatter to quantify the effect. The injected parameters are separated into 10 bins, and we take the median and median absolute deviation of the difference between the spotted and non-spotted model’s inferred parameters for each bin. We take the median as a measure of the average bias and the median absolute deviation as a proxy for the scatter.

In Fig. 5, we show the effect of the injected parameters on the stellar spot spectra through the difference between the recovered spot and non-spot model T_{eff} . Fitting a spotted spectrum with a small x_{spot} with a non-spotted spectrum introduces a consistent bias to the inferred T_{eff} of about -25 K: a non-spotted model tends to underestimate the true effective temperature of a spotted spectrum. A scatter is also introduced T_{eff} on the scale of ~ 50 K for spectra with significant spot coverage (low x_{spot} and large f_{spot}). The other injected parameters do not appear to have any strong correlations or

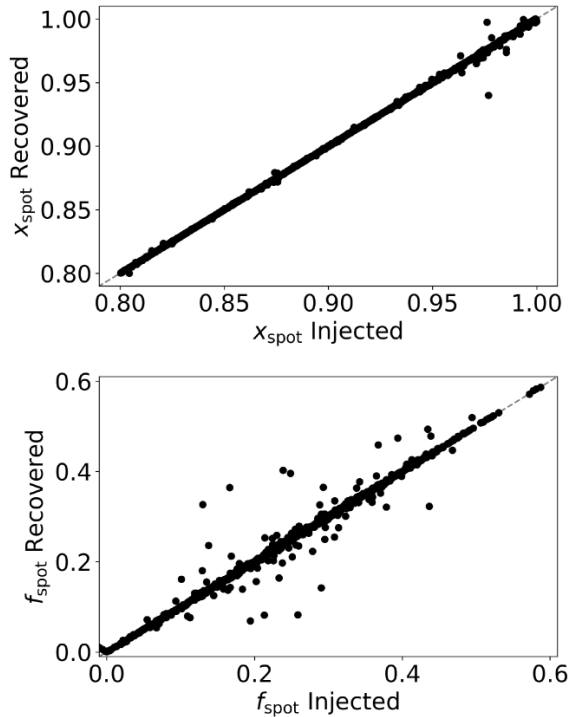


Figure 3. Recovered spot parameters (x_{spot} and f_{spot}) from the synthetic spotted spectra fitted with a spotted model of the stellar spectra against the injected parameters of the synthetic spectra. We identify that the spot parameters are not always accurately recovered through the fitting procedure. The recovered spot parameters are notably more inaccurate as x_{spot} approaches 1.

effects on the recovered non-spot T_{eff} . Their median values are zero, and MAD appears consistent at ~ 25 K.

Fig. 6 shows the effects of fitting spotted spectra with a non-spotted model on $\log g$ (orange) and $\log v \sin i$ (red), respectively. There appears to be no statistically significant bias introduced to both of the inferred parameters as the median of each bin of injected parameters is consistently about zero. However, a consistent scatter is introduced to both parameters. The MAD of $\Delta \log g$ and $\Delta \log v \sin i$ in each injected parameter bin have an average value of ~ 0.025 dex – corresponding to an average scatter on $v \sin i$ of ~ 1 km s $^{-1}$. The scatter peaks for both recovered parameters at ~ 0.05 dex for stars with significant spot coverage – which corresponds to a maximum scatter on $v \sin i$ of ~ 2 km s $^{-1}$. The scatter on recovered $v \sin i$ and $\log g$ is otherwise constant with the other injected parameters.

The effect of fitting spotted spectra with a non-spotted model is significant in the recovery of metallicity. This is seen in Fig. 6 (green), where we compare the recovered $[\text{Fe}/\text{H}]$ with a spotted and non-spotted model of the stellar atmosphere against the injected parameters of our spotted spectra. This process does not introduce a bias to the inferred metallicity of the spectra but does introduce a significant scatter to the recovered value, representing an intrinsic ‘minimum floor’ of systematic uncertainty if the effects of spots are not included (see Section 4).

The scatter introduced to $[\text{Fe}/\text{H}]$ by fitting spotted spectra with a non-spotted model increases with injected f_{spot} . As f_{spot} approaches 1, the MAD of $\Delta [\text{Fe}/\text{H}]$ reaches a maximum of about 0.05 dex. Comparatively, as x_{spot} decreases, so does the MAD of $\Delta [\text{Fe}/\text{H}]$,

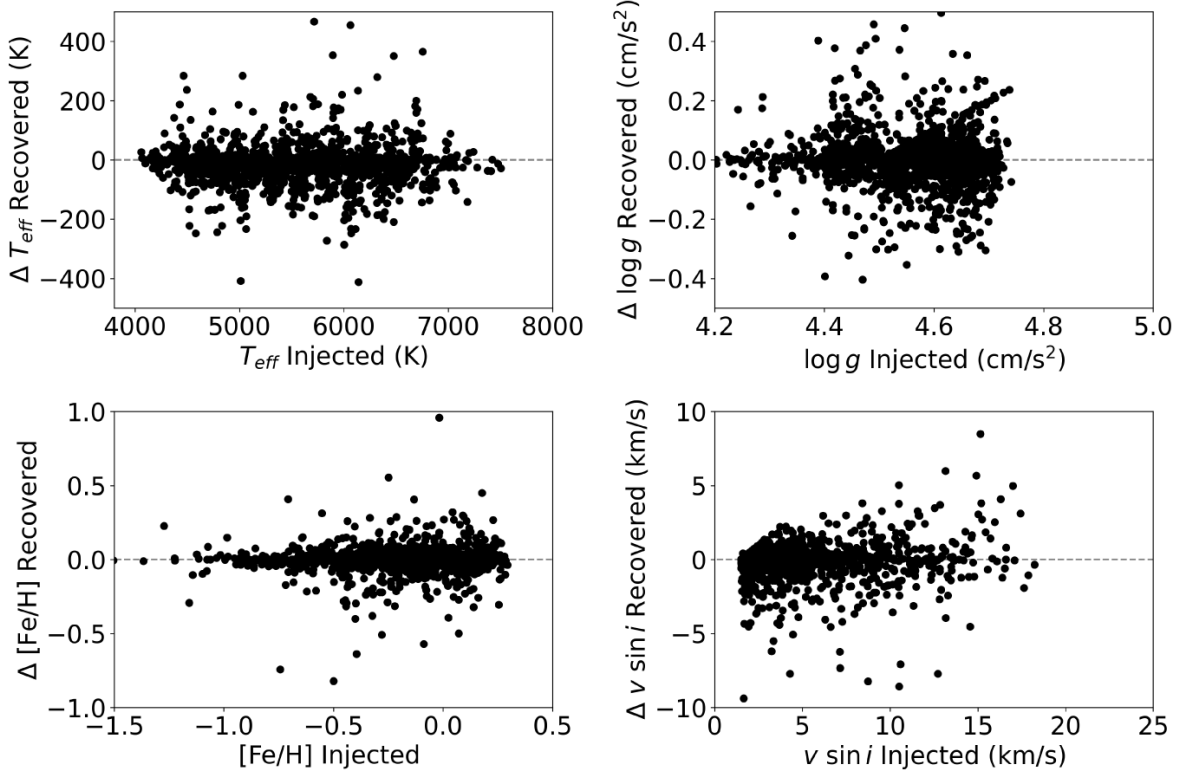


Figure 4. The difference between the recovered traditional stellar spectra parameters (T_{eff} , $\log g$, $[\text{Fe}/\text{H}]$, and $v \sin i$) from the synthetic spotted spectra fitted with both a spotted and non-spotted models of the stellar spectra against the injected parameters of the synthetic spectra (spotted model and non-spotted model recovered parameter). We identify scatter introduced to each of the stellar parameters when fitting spotted spectra with a non-spotted model of the stellar atmosphere.

peaking again at 0.04 dex. As the scatter in the other injected parameters is relatively constant, there is no significant relation between the other spectral parameters and $\Delta[\text{Fe}/\text{H}]$. The introduced scatter in $[\text{Fe}/\text{H}]$ is dominated by the spot parameters of spectra.

4 DISCUSSION

The results in Section 3 indicate that using a non-spotted model to fit spotted stellar spectra introduces a systematic bias of up to -25 K in effective temperature and no substantial bias in other parameters. In their study of fitting a spotted stellar model to APOGEE spectra of members in the Pleiades and M67, Cao & Pinsonneault (2022) find a systematic 0.1 dex enhancement in observed $[\text{Fe}/\text{H}]$. The lack of bias we find here could be attributed to different stellar populations of stars (e.g. some stars are biased in one direction, but in our population, that effect is mitigated by biases in the opposite direction). We find that the effects of model mismatch (i.e. using a non-spotted model to fit a spotted spectrum) can also introduce a scatter (measured by median absolute deviation) of about 50 K in effective temperature and 0.05 dex in other parameters. If we assume that the spot model we adopt is representative of reality, then these scatter values would represent a minimum systematic uncertainty in these parameters if the wrong model (a non-spotted model) is used. These deviations are comparable to the typical random uncertainties reported by the APOGEE survey (150 K, 0.13 dex, and 0.1 dex; Hegedüs et al. 2022), although these random uncertainties will vary with signal to noise.

Systematic uncertainties (like model mismatches) will dominate in high signal-to-noise ratios, and the level of scatter we find in metallicity (0.05 dex) is comparable to the effects of radiative levitation, atomic diffusion (Önehag et al. 2014), and magnetic broadening of absorption lines (Spina et al. 2020). Unlike these effects, which can in part be mitigated through parametrization with other stellar parameters, accounting for stellar spots requires a model that explicitly predicts their contribution to the emergent spectrum. This scatter in $[\text{Fe}/\text{H}]$ is significant as it is of the same order as the precision of spectroscopic inference of metallicity. In particular, a differential analysis of two Solar twins might report abundance uncertainties on the level of 0.01–0.02 dex. While the two stars are selected to be extremely similar in order to mitigate systematic effects, those two stars could have very different coverages of stellar spots, which would introduce a systematic uncertainty floor.

4.1 Imperfect models

The results we show here are limited in their applicability. When generating the mock data, only a fraction of randomly drawn stellar parameters could be used to synthesize spectra, either because of limitations of stellar isochrones, the spectral grid, or limits in the procedure in estimating an appropriate rotational velocity and Rossby number. We also limit the ages of the stellar sample to 4.6 Gyr – the maximum ages of both the models used to determine the convective turnover time-scale and grid of rotational periods set by observations.

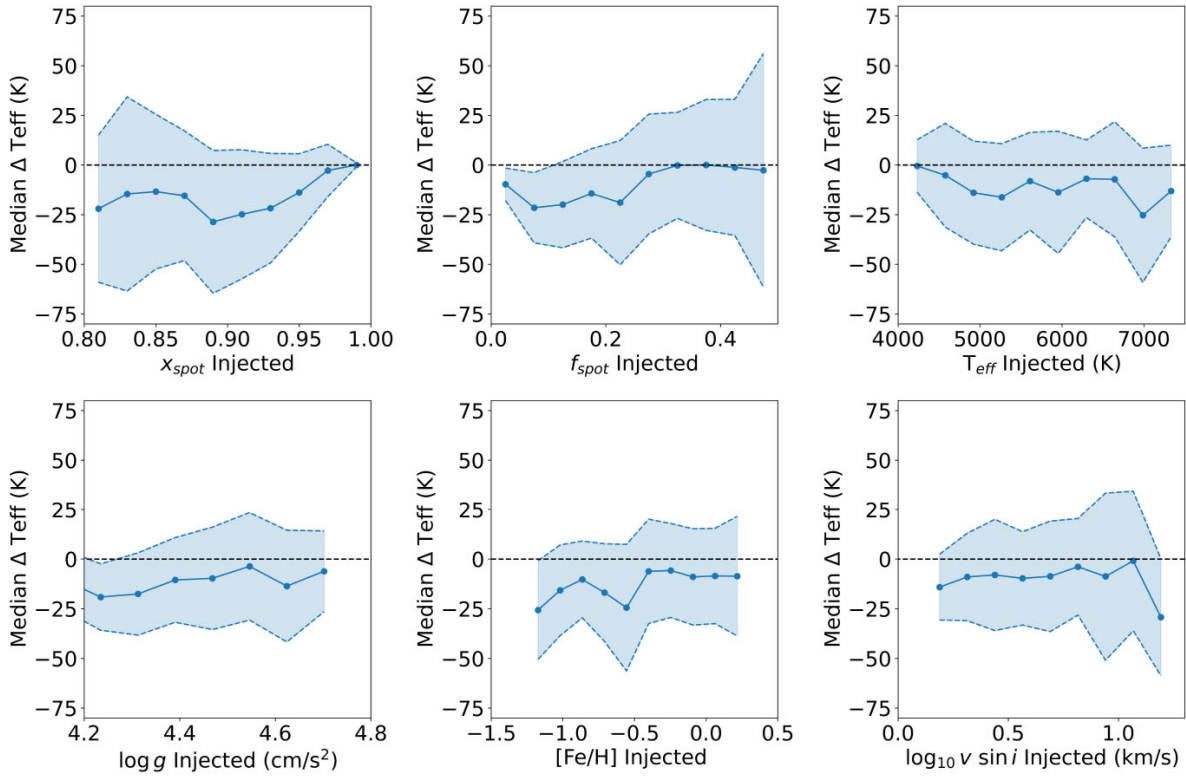


Figure 5. Bias introduced to T_{eff} (blue) when fitting spotted spectra with a non-spotted model against injected parameters of synthetic spectra. Each injected parameter is binned into 10 bins across the range of injected parameters. The median and median absolute deviation of the difference between the spotted and non-spotted recovered T_{eff} (ΔT_{eff}) are then calculated in each bin. Scatter points show the median ΔT_{eff} for each bin in injected parameters. Filled areas show one maximum absolute deviation above and below the median value and dashed lines indicate the edge of this range. Inference of T_{eff} with a non-spotted model injects random scatter on average of the scale of ~ 50 K and introduces a consistent bias of the order of ~ -25 K for spectra with significant spot coverage.

As a result, our sample is limited to relatively young stars, and there are hints of a bias in injected parameters towards higher f_{spot} . We have extensively probed the region where the effect should be most prevalent in terms of the scatter it introduces, but this is not intended to be a complete and representative population of main-sequence stars. The quantitative results may not be perfectly accurate for some regions of the HR diagram, and might vary with photosphere geometry. However, by assuming spots are present everywhere across the main sequence, our analysis shows where the consequential effects are most or least prevalent.

The treatment of stellar spots in this work requires some discussion. Stellar spots are highly complex regions on the surface of stars. The position of spots relative to the observer, their temporal evolution, and the inherent magnetic activity and faculae surrounding stellar spots, would all introduce complexity to the emergent spectra from these regions. The spotted model employed in this work is a first-order approximation of the average effect of spots on stellar spectra. The functional form of the temporal evolution of the stellar spots in stars other than the Sun is not well known. For a given f_{spot} we could assume that x_{spot} varies on some periodic or temporal scale, even if we do not know the functional form of that variability. In this scenario with our model, x_{spot} is drawn from a uniform prior, which implicitly assumes that we are observing the star at some random time. This modelling of x_{spot} is relatively crude since, in principle, x_{spot} could vary as a function of other stellar parameters.

Investigations of the evolution of fractional spot coverage of stars is a developing field. For example, recent works have shown an enhancement in f_{spot} for stars undergoing core-envelope recoupling (Cao, Pinsonneault & van Saders 2023). For this reason, our results are only indicative rather than prescriptive. Applying this model to more stars APOGEE samples and time series spectroscopic observations of stars could elucidate the relationship between the parameters.

Cao & Pinsonneault (2022) suggest that young, magnetically active stars – stars with Rossby numbers <0.4 – have $f_{\text{spot}} > 0.1$, saturating at $f_{\text{spot}} \sim 0.3$, with significant scatter, when $Ro < 0.2$. There is also a significant scatter in f_{spot} for these stars. The use of the Rossby number to reflect the magnetic/spot activity of stars should be treated with some care. The Sun expresses periodic evolution of its magnetic activity (time-scale of the order of decades) and stellar spot expression (time-scale of the order of years). The range of fractional spot coverages we observe in the Sun is of the order of $[0, 0.12]$ without variations in the Rossby number. As a result, we draw the injected f_{spot} from relations with Rossby number and add a random scatter drawn from a Gaussian distribution with a standard deviation of 0.1.

Employing a non-spotted spectra model to fit spotted spectra can introduce a scatter to recovered parameters, but fitting a spotted model to non-spotted spectra has little to no effect on the recovered parameters. We recommend that a spotted model, if only as simple as

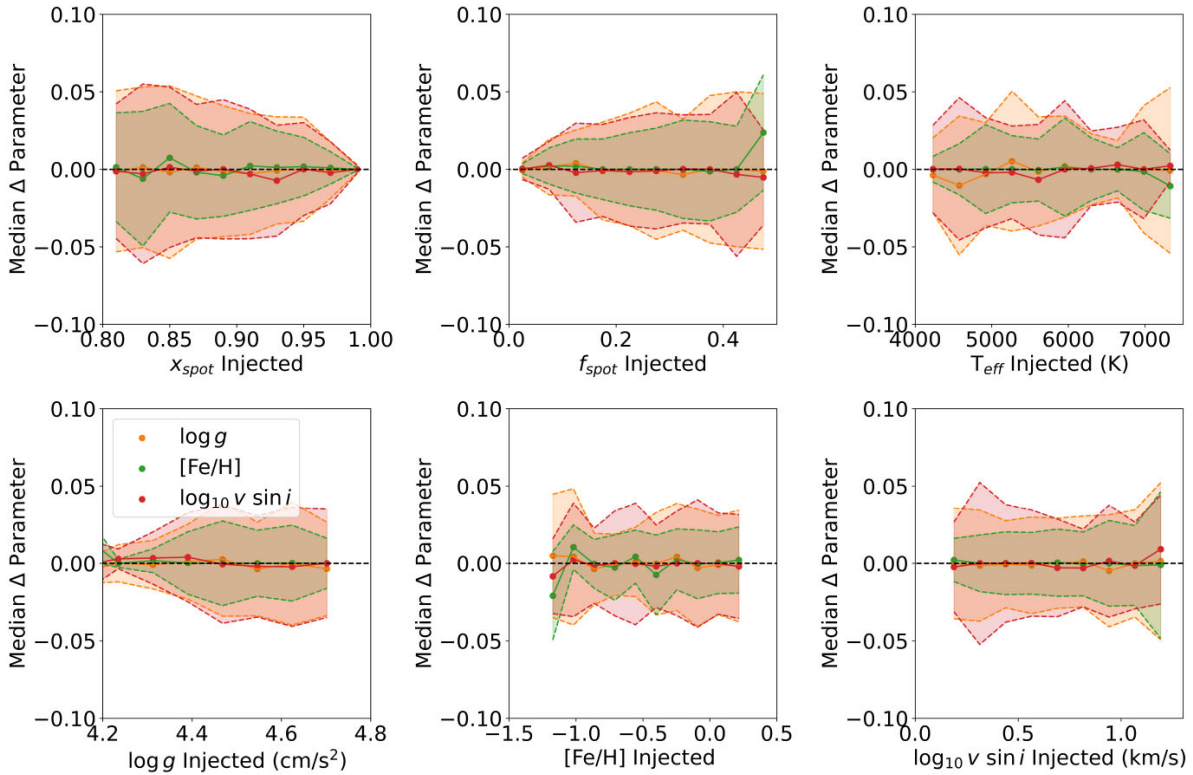


Figure 6. Bias introduced to $\log g$ (orange), $[{\rm Fe/H}]$ (green), and $\log_{10} v \sin i$ (red) when fitting spotted spectra with a non-spotted model against injected parameters of synthetic spectra. Here, we have plotted $\log v \sin i$ as the grid we perform interpolation over is distributed uniformly in $\log v \sin i$ and to make direct comparisons to the other stellar parameters ($[{\rm Fe/H}]$ and $\log g$). Each injected parameter is binned into 10 bins across the range of injected parameters. The median and median absolute deviation of the difference between the spotted and non-spotted recovered parameters (Δ parameter) are then calculated in each of these bins. Scatter points show each bin's median Δ parameter in injected parameters. Filled areas show one maximum absolute deviation above and below the median value and dashed lines indicate the edge of this range. Fitting spotted spectra with non-spotted models does not introduce a bias to the inferred parameters though it does introduce a scatter. This scatter increases with decreasing x_{spot} and increasing f_{spot} to a maximum median absolute deviation of the order of ~ 0.05 for $\log g$, $[{\rm Fe/H}]$, and $\log v \sin i$ – which corresponds to a maximum scatter on $v \sin i$ of $\sim 2 \text{ km s}^{-1}$. The scatter is otherwise approximately constant for all other parameters, and on average ~ 0.025 – which corresponds to an average scatter on $v \sin i$ of $\sim 1 \text{ km s}^{-1}$.

the one used in this work, will consistently recover stellar parameters better than a non-spotted model while also providing a measure of the spot parameters of stars.

4.2 When should a spotted model of the stellar atmosphere be employed?

The scatter introduced to the recovered stellar parameters increases with fractional spot coverage. Fractional spot coverage is inversely related to the rotation rate of stars through Ro . Further, the rotation rate of stars decreases with time, owing to magnetic braking. As a result, the fractional spot coverage of stars is expected to decrease with age.

We can probe when the scatter introduced to the recovery of stellar parameters by stellar spots is most prominent by calculating the scatter in $\Delta[{\rm Fe/H}]$ with bins of age. In Fig. 7, we show the bias and scatter introduced to $\Delta[{\rm Fe/H}]$ with respect to stellar age. The introduced scatter is greatest for stars younger than $\sim 2 \text{ Gyr}$ is ~ 0.02 , while the bias, measured through the median, is zero for stars in this age range. The scatter decreases for older stars ($> 3 \text{ Gyr}$) to ~ 0.01 ,

but the median $\Delta[{\rm Fe/H}]$ appears to increase with increasing age. The increase in the median value is most likely not indicative of a trend and rather the result of the low number of stars in the larger age bins.

The trends that we identify in this work are only qualitative – though they do allow us to make recommendations for future work. Our results indicate that fitting the spotted spectra of a star with a non-spotted model when $f_{\text{spot}} > 0.1$ will introduce a scatter to bias the recovered parameters. We suggest using a spotted model if a star is significantly photometrically variable due to stellar spots. McQuillan et al. (2014) calculated the rotation periods of low-mass main-sequence stars that are photometrically variable due to stellar spots. They were able to determine the rotation rates of stars across a wide mass range ($0.6 < M_{\odot} < 1.1$) at multiple points along the main sequence. These stars must therefore express stellar spots and may have the measured stellar parameters influenced by the effect we identify in this work. They estimated that ~ 23 per cent of main-sequence stars exhibit definite rotational modulation from stellar spots, a lower bound due to observational effects. We therefore believe at least 1/4 of the main-sequence stars may be affected by this bias.

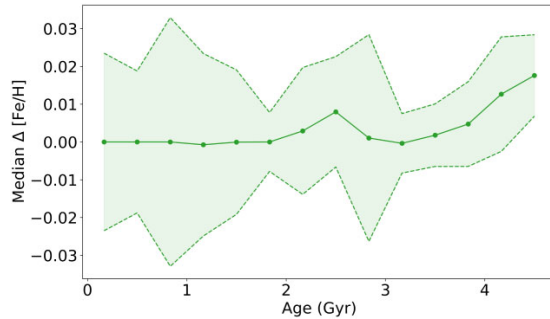


Figure 7. Bias introduced to $[Fe/H]$ when fitting spotted spectra with a non-spotted model against the age of the model used to generate synthetic spectra. Age is binned into 10 bins across the range of injected parameters. The median and median absolute deviation of the difference between the spotted and non-spotted recovered $[Fe/H]$ ($\Delta[Fe/H]$) are then calculated in each of these bins. Scatter points show the median $\Delta[Fe/H]$ for each bin in injected parameters. Filled areas show one maximum absolute deviation above and below the median value and dashed lines indicate the edge of this range. We find that the introduced scatter is greatest for stars younger than ~ 2 Gyr is ~ 0.02 while the bias is 0 for stars in this age range. The scatter decreases for older stars (> 3 Gyr) to ~ 0.01 but the median $\Delta[Fe/H]$ increases with increasing age. This is like the result of the small number of stars in our sample in this age range rather than indicative of a trend.

5 CONCLUSIONS

Here, we have shown that stellar spots can introduce measurable systematic bias and variance to inferred stellar parameters when a non-spotted model is used. The results demonstrate that spectra with strong spot features can introduce a scatter in inferred metallicity of the order of 0.05 dex. This emphasizes the need for caution when performing spectroscopic analysis on stars with visible spots, particularly young, fast-rotating stars. Our findings highlight the importance of incorporating the effect of spots into spectroscopic models to ensure accurate and precise results.

The magnitude of this effect is comparable to others that plague stellar spectroscopy, including atomic diffusion, radiative levitation, and non-local thermodynamic equilibrium. However, the impact of this effect will vary depending on the scientific context. Turn-off ages of clusters are likely to be only minimally impacted, as the metallicity bias for old, slowly rotating stars is less than 0.01 dex. In contrast, a systematic error floor of 0.05 dex caused by spots on the main sequence would critically limit the capacity of strong chemical tagging (Casamiquela et al. 2021). Similarly, star-spots could limit any inferences from differential abundance analyses of Sun-like stars, where the typical reported uncertainty is 0.01–0.02 dex (e.g. Meléndez et al. 2014; Nissen 2015; Reggiani et al. 2016; Maia et al. 2019; Liu et al. 2020; Nissen et al. 2020; Spina et al. 2021). While we have focused on the impact on overall metallicity and not on individual abundances, it will be important to examine these effects more closely at a per-element level. These results provide valuable insights for future studies on stars and their properties and underscore the need for continued research on the impact of spots on spectroscopic inference.

ACKNOWLEDGEMENTS

We thank the reviewer for their constructive feedback that helped improve the paper. We thank Prof. Ilya Mandel for his helpful feedback and our fruitful discussions. ARC thanks Jon Holtzman

and Adam Wheeler for helpful discussions. ARC was supported in part by the Australian Research Council through a Discovery Early Career Researcher Award (DE190100656). Parts of this research were supported by the ARC Centre of Excellence for All Sky Astrophysics in 3 Dimensions (ASTRO 3D) through project number CE170100013.

DATA AVAILABILITY

The data and models underlying this article are available upon request to the corresponding author.

REFERENCES

- Anders F. et al., 2016, *Astron. Nachr.*, 337, 926
 Bensby T., Feltzing S., Lundström I., 2004, *A&A*, 421, 969
 Berdyugina S. V., 2005, *Living Rev. Sol. Phys.*, 2, 8
 Blanco-Cuaresma S., 2019, *MNRAS*, 486, 2075
 Cao L., Pinsonneault M. H., 2022, *MNRAS*, 517, 2165
 Cao L., Pinsonneault M. H., van Saders J. L., 2023, preprint (arXiv:2301.07716)
 Casamiquela L., Castro-Ginard A., Anders F., Soubiran C., 2021, *A&A*, 654, A151
 Crowther P. A., 2007, *ARA&A*, 45, 177
 Gibson B. K., Fenner Y., Renda A., Kawata D., Lee H., 2003, *Publ. Astron. Soc. Aust.*, 20, 393
 Gustafsson B., Edvardsson B., Eriksson K., Jørgensen U. G., Nordlund A., Plez B., 2008, *A&A*, 486, 951
 Hegedüs V., Mészáros S., Jofré P., Stringfellow G. S., Feuillet D., García-Hernández D. A., Nitschelm C., Zamora O., 2023, *A&A*, 670, A107
 Herbst K., Papaioannou A., Airapetian V., Atri D., 2020, *ApJ*, 907, 89
 Holtzman J. A. et al., 2018, *AJ*, 156, 125
 Johnson J. A., Fields B. D., Thompson T. A., 2020, *Phil. Trans. R. Soc. A: Math. Phys. Eng. Sci.*, 378, 20190301
 Karoff C. et al., 2018, *ApJ*, 852, 46
 Kraft R. P., 1967, *ApJ*, 150, 551
 Landin N. R., Mendes L. T. S., Vaz L. P. R., 2010, *A&A*, 510, A46
 Laughlin G., Adams F. C., 1997, *ApJ*, 491, L51
 Liu F., Yong D., Asplund M., Wang H. S., Spina L., Acuña L., Meléndez J., Ramírez I., 2020, *MNRAS*, 495, 3961
 McQuillan A., Mazeh T., Aigrain S., 2014, *ApJS*, 211, 24
 McWilliam A., Rauch M., eds, 2004, Origin and Evolution of the Elements, Vol. 4 in Carnegie Observatories Astrophysics Series, Cambridge Univ. Press, Cambridge, Cambridge
 Maia M. T., Meléndez J., Lorenzo-Oliveira D., Spina L., Jofré P., 2019, *A&A*, 628, A126
 Maldonado J., Villaver E., Eiroa C., Micela G., 2019, *A&A*, 624, A94
 Mathur S. et al., 2014, *A&A*, 562, A124
 Meléndez J. et al., 2014, *ApJ*, 791, 14
 Morris B. M., Curtis J. L., Sakari C., Hawley S. L., Agol E., 2019, *AJ*, 158, 101
 Morton T. D., 2015, Astrophysics Source Code Library, record ascl:1503.010
 Nichols-Fleming F., Blackman E., 2020, *MNRAS*, 491, 2706
 Nissen P. E., 2015, *A&A*, 579, A52
 Nissen P. E., Christensen-Dalsgaard J., Mosumgaard J. R., Silva Aguirre V., Spitoni E., Verma K., 2020, *A&A*, 640, A81
 Önehag A., Korn A., Gustafsson B., Stempels E., Vandenberg D. A., 2011, *A&A*, 528, A85
 Önehag A., Gustafsson B., Korn A., 2014, *A&A*, 562, A102
 Pagel B. E. J., 2009, Nucleosynthesis and Chemical Evolution of Galaxies, Cambridge Univ. Press, Cambridge
 Pasquini L., Döllinger M. P., Weiss A., Girardi L., Chavero C., Hatzen A. P., Silva L. d., Setiawan J., 2007, *A&A*, 473, 979
 Pinsonneault M. H., Steigman G., Walker T. P., Narayanan V. K., 2002, *ApJ*, 574, 398
 Pont F., Eyer L., 2004, *MNRAS*, 351, 487

- Randich S. et al., 2022, *A&A*, 666, A121
 Reggiani H., Meléndez J., Yong D., Ramírez I., Asplund M., 2016, *A&A*, 586, A67
 Salaris M., Cassisi S., 2017, *R. Soc. Open Sci.*, 4, 170192
 Salpeter E. E., 1955, *ApJ*, 121, 161
 Santos A. R. G., Breton S. N., Mathur S., García R. A., 2021, *ApJS*, 255, 17
 Shetrone M. et al., 2015, *ApJS*, 221, 24
 Smith V. V. et al., 2021, *AJ*, 161, 254
 Somers G., Pinsonneault M. H., 2015, Proc. IAU Symp. 10, Young Stars & Planets Near the Sun. Cambridge Univ. Press, Cambridge, p. 91
 Spada F., Gellert M., Arlt R., Deheuvels S., 2016, *A&A*, 589, A23
 Spina L. et al., 2020, *ApJ*, 895, 52
 Spina L., Sharma P., Meléndez J., Bedell M., Casey A. R., Carlos M., Franciosini E., Vallenari A., 2021, *Nat. Astron.*, 5, 1163
 Tayar J., Claytor Z. R., Huber D., van Saders J., 2022, *ApJ*, 927, 31
 Wheeler A. J., Abruzzo M. W., Casey A. R., Ness M. K., 2023, *ApJ*, 165, 2

This paper has been typeset from a \TeX / \LaTeX file prepared by the author.

Chapter 4

The Intermediate Period Gap

Abstract

Photometric variability due to stellar spots allows astronomers to measure the surface rotation periods of stars. Within multiple missions' rotational period samples (e.g. *Kepler*, *K2*, *ZTF*), there is a distinct dearth of observations of stars rotating at intermediate periods $15 \gtrsim P_{\text{rot}} \gtrsim 20$ days. This dearth of observations is known as the intermediate period gap. The position of this gap varies with the colour of the stars. Various mechanisms have been proposed to explain the dearth of observations from stars physically "jumping" the gap through enhanced wind-braking, to stars above and below the gap representing two populations of stars, to the gap representing a minima of probability to observe rotation rate. The exact cause of the dearth of observations is currently unknown. In this Chapter, we show that the gap may align itself with minima in both the photometric variability range and magnetic activity indicator $\log R_{\text{HK}}^+$. This suggests that the minima of photometric variability and $\log R_{\text{HK}}^+$ result from the same mechanism. We also show that there is not a subsample of stars with uncharacteristically low magnetic activity in the sample of stars without detection rotation periods. Further, the number of stars with undetected rotation periods is unlikely to fill the dearth of observations. The data suggests that the gap does not represent a minima of observation of stellar rotation through photometric variability. Following this, we investigate the propose the hypothesis that the gap represents a sudden increase in the observed

rotation period of stars through the onset of latitudinal differential rotation. The rotational period gap can be reproduced under this mechanism with observationally derived relations between equatorial and differential rotation evolution.

4.1 Introduction

Measurement of the rotational period of samples of stars allows us to understand internal mechanisms that we otherwise would not be able to probe. An unexplained feature of the rotational period distribution of low-mass main-sequence stars comes in the form of what is known as the intermediate period gap. The intermediate period gap represents a minimum of observations of stars with particular rotation periods dependent on temperature, first observed by [McQuillan et al. \(2014\)](#). The feature is selection function independent. The gap is robust between different photometric observation missions ([McQuillan et al., 2014](#); [Davenport, 2017](#); [Davenport & Covey, 2018](#); [Lu et al., 2022](#)) and multiple period detection methods. Further, the position of the gap varies in period with respect to mass. The quality cuts made to data sets in which rotation period is attempted to be measured ([McQuillan et al., 2014](#); [Claytor et al., 2022](#), e.g. removing binaries and subgiants) are not biased away from detecting stars within the gap. If the gap aligned itself with a line of constant rotation in only one mission, then the mechanism underlying the gap could be more readily explained through the selection function of said mission. These factors suggest that the intermediate period gap represents a function of stellar evolution or an unaccounted-for problem in observing rotation periods through photometric oscillations from stellar spots. The intermediate period gap interests astronomers and astrophysicists because the mechanism underlying it is unexplained; therefore, this process's effects are unknown in stellar evolution.

Multiple mechanisms have been proposed to explain the intermediate period gap. [McQuillan et al. \(2014\)](#) first proposed that the gap represents bimodal bursty star formation in the local *Kepler* field. They suggest that the lower rotation period (faster rotators) prong represents a younger population, and the upper rotation period prong represents an older population, with the gap representing a minima in star formation at a particular time. [Davenport & Covey \(2018\)](#) support local bursty star formation hypothesis by separating the *Kepler* rotation period distribution by distance through *Gaia* parallaxes. They find that the gap appears to disappear for stars further away than 525 pc. This work does not acknowledge, however, that at those distances (a) observations of stars are magnitude-limited to brighter high-mass stars ($M \geq 0.9 M_{\odot}$) where observations of the gap are tentative and (b) period detection and temperature/colour measurement are much less precise. If the gap extends up to these high-mass stars, then its existence

can be blurred out by the imprecision of these measurements. Their work may also support this explanation. In the full ([McQuillan et al., 2014](#)) sample the gap disappears for high mass ($M \geq 0.8M_{\odot}$, $B_P - R_P \leq 1.0$) stars. In the distance limited ($\leq 525\text{pc}$) sample, the gap appears to permeate to these higher-mass stars. This can be seen in the rotational period-colour distribution in the top two panels in Figure 2 of [Davenport & Covey \(2018\)](#) where distance is limited to 525pc.

More recent works significantly disfavour the bursty star formation hypothesis. [Gordon et al. \(2021\)](#) detected the gap in multiple pointings of the *K2* mission. In contrast, [Curtis et al. \(2020\)](#) found that the open cluster Ruprecht 147 contains stars above and below the gap - and a possible star detection within the intermediate period gap. This suggests that the gap is not a coeval feature and instead a feature of the rotational evolution of low-mass stars. [Curtis et al. \(2020\)](#) instead proposed that the gap aligns with a line of constant Rossby number ($R_o \sim 0.6$) - rotation rate scaled quantity shown to be associated with the magnetic activity of stars.

As of writing, there are two leading explanations for the gap. First, consider that the intermediate rotational period gap represents a sudden onset of extreme rotational braking. ([McQuillan et al., 2014](#)) suggested another explanation for the intermediate period gap through a rapid spin-down - "jumping" across the gap quickly, resulting in decreased stars' density in this period-colour space region. For example, the rapid spin-down could be caused by core and convective envelope rotational decoupling at the upper edge of the lower prong near the rotational period gap. In this mechanism, the core and envelope evolve independently; the envelope - having a much smaller moment of inertia than the core - is spun down rapidly under the same magnetic braking conditions. Following the gap, the core and envelope then recouple, exchanging angular momentum and returning to a normal rate of magnetic braking. [Gordon et al. \(2021\)](#) argued in favour of this hypothesis based on the rotation period distribution of *K2*. [Curtis et al. \(2020\)](#) argued that two-zone angular momentum transport models, such as those by [Spada & Lanzafame \(2020\)](#) can reproduce a stalled braking behaviour required to explain the lower prong of the intermediate rotational period gap - but their model could not explain the rapid-spin down. This hypothesis is generally supported by the tentative observation of low-mass fully convective stars permeating the gap ([Lu et al., 2022](#)).

The other leading theory is that the gap results from a low probability of observing

stars within the gap. Chahal et al. (2022) proposes that the gap results from the low magnetic activity of stars within the gap resulting in very few expressed stellar spots and, thus, a low probability of observing stars in the gap. On the other hand, Reinhold et al. (2019) and Reinhold & Hekker (2020) proposed a transition from a dark spot dominance to bright faculae dominance in the activity cycle of a star may result in the rotational period gap¹. They suggest that as a star spins down and the magnetic field topology changes, the initially strong and long-lived spots are replaced by smaller, short-lived spots surrounded by bright faculae. In such a scenario, the photometric variability amplitude decreases because of the partial cancellation by the increase and decrease in brightness from the faculae and spots. Hence, the stars with small photometric variability will not be detected. These mechanisms are supported by the gap aligning with a line of constant Rossby number - indicative of common magnetic field evolution between these stars - and by the photometric variability reaching a local minimum surrounding the gap.

Both of these hypotheses are of interest to astronomers and astrophysicists. Suppose the gap manifests from sudden onset enhanced magnetic braking. In that case, gap stars represent a laboratory for understanding the evolution of the magnetism in stars, and the underlying mechanism that provides the enhanced wind braking is of interest to the scientific community. This enhanced braking would need to be accounted for in gyrochronological models. On the other hand, let's say that the gap results from a low probability of observing stars within the gap; there are stars with rotational periods that would place them in the gap, but we cannot measure their periods for whatever reason. If this is the case, we have undoubtedly observed gap stars that we do not know are gap stars. Therefore, whether gap stars are peculiar - photometrically, spectroscopically or asteroseismically - is unknown. It is entirely possible, but likely not probable, that gap stars have been previously flagged as peculiar, but the link between the gap and these stars has never been made. On the other hand, gap stars may not be otherwise peculiar - chemically or, say, in terms of magnetic activity. If indeed they are not otherwise peculiar, then, oxymoronically, the reason for their lack of observation raises more questions about the mechanism underlying the gap.

¹It is important to note that in this work differentiates between the rotation brightness modulation and brightness modulation from the stellar activity cycle. Stellar activity modulation refers to the long-term evolution of average brightness due to stellar spots and faculae rather than variations on the rotational time scale.

On the other hand, if the gap results from a low probability of observing stars within the gap, we have undoubtedly observed gap stars, spectroscopically or asteroseismically, that we do not know are gap stars. Therefore, whether gap stars are peculiar - photometrically, spectroscopically or asteroseismically - is unknown. Gap stars may have been previously flagged as peculiar, but the link between the gap and these stars has never been made. On the other hand, gap stars may not be otherwise peculiar - chemically or, say, in terms of magnetic activity. If indeed they are not otherwise peculiar, then, oxymoronically, the reason for their lack of observation raises more questions about the mechanism underlying the gap.

In this work, we will use the terms probability of observation of rotation and detectability of rotation period. While they are related, they are different terms. The detectability of rotation requires a relatively short cadence, on the time scale of days-weeks, observations with distinct variability in the light curve due to spots or faculae. It depends on several factors on a star-to-star basis, including the inclination angle, wherein the magnetic activity cycle observations are made, where faculae and spots are distributed on the star's surface, and the lifetimes of these surface features relative to the star's rotation period. ([Aigrain et al., 2015](#); [Reinhold et al., 2019, 2021](#)). On the other hand, the probability of observation of rotation refers to a more stellar parameter-based average statistic under the comparison of the set of stars with and without detection rotation periods. The detectability of rotation with fundamental stellar properties (temperature, metallicity, stellar age etc.) has been previously investigated. Cool stars, especially cooler than 5200K, have a significantly higher probability of rotational period observation than hotter stars. Cool stars both tend to have higher magnetic activity, and therefore more spots, and also have more significant brightness variations as a result of the same level of surface spot activity compared to hotter stars ([McQuillan et al., 2014](#); [Santos et al., 2021](#); [Zhang et al., 2020](#)) A relation with metallicity has also been investigated ([Amard et al., 2020](#); [See et al., 2021](#); [Claytor et al., 2022](#)). Higher-metallicity ($[\text{Fe}/\text{H}] \gtrsim -0.1$) stars are detected in periods more frequently than lower-metallicity stars. ([Avallone et al., 2022](#); [Masuda, 2022](#)) separate the metallicity dependence from age and suggest that this effect arises from the fact that younger, more active stars are enriched by metals from Galactic chemical evolution rather than a result of the metallicity on the evolution of magnetic activity and probability of rotational observation. Older stars tend to have a lower probability of observation - their rotation periods are long and thus require a

longer baseline of observations, and they tend to have weaker magnetic fields and thus express a smaller number of stellar spots.

Many stars cannot have their rotation periods measured purely from the inclination angle's effect on the rotation's detectability. If a star is pole-on, even if a star expresses surface features close to the axis of rotation, no variance in the brightness of that star will be detected. Increasing the sensitivity of telescopes, and methods of determining rotation periods, increase the number of stars that can have their rotation periods detected. Still, this number is bounded by the subsample of stars that cannot have their rotation measured. While the distribution of the inclination angle of stars is biased toward equator-on observations, a non-zero population of stars will never have their rotation periods detected through photometric variability.

This Chapter is structured as follows. In Section 4.2 we will introduce the so-called magnetic activity indicators. In Section 4.3, we reconfirm that the gap aligns with minima in the photometric variability range. In Section 4.4, we show that this minima aligns itself with a minima in $\log R_{\text{HK}}^+$. In Section 4.5, we then show that the sample of stars with undetected rotation does not contain a subsample of stars with magnetic activity low enough to fall below the rotation-detection threshold. Section 4.5 we show that the number of stars required for the dearth of observations to no longer be considered a dearth requires a larger number of stars than the number of stars within the undetected sample. In Section 4.6, we propose and show that the rotational period gap can be reproduced by considering the effects of latitudinal differential rotation on the observed rotation rates of stars. Finally, in Section 4.7, we summarise and discuss the implications of our work on proposed mechanisms to explain the intermediate period gap.

4.2 Stellar magnetic activity indicators

Stellar magnetism is a complex component of stellar evolution that is hard to predict and model. Links between magnetism and mass, metallicity, age, convection, and rotation have been identified (Cao & Pinsonneault, 2022). These links are, however, based upon observations of stars rather than astrophysical theory. The observation of rotational modulation in a light curve, and the observation of surface rotation from that modulation, requires cool spots and bright faculae created by concentrated magnetic fields

near the surface of a star. Stars with stronger magnetic fields tend to express larger spot coverage, thus having larger rotational photometric modulation and more readily observable rotation periods.

Stellar activity is the collective term used to describe different effects magnetic fields have on stars. This name arises from the variability phenomena occurring from structured magnetic fields emerging from the convective envelope of stars - for example, flares and large-scale photometric variability from stellar surface features (stellar spots or faculae). The strength of the magnetic field can be directly or indirectly measured in several ways, and a star's photometric variance varies with the magnetic field's strength. Here we will discuss three: the elemental magnetic activity through $\log R_{\text{H},\text{K}}^+$ and S , the photometric variability range (R_{per}) and the fractional spot coverage of a star (f_{spot}).

Throughout the stellar atmosphere, emission features arise through the interaction of light and elements. Different absorption features arise from both different elements and different stellar atmosphere conditions. One of the most frequently probed indicators of chromospheric activity, and thus magnetic field strength, in low-mass magnetically active stars is the non-thermal flux reversal in the cores of the Ca II H and K lines at 3968Å and 3933Å, respectively. These ions originate in the upper photosphere and chromosphere and are sensitive to magnetic activity.

Two measures of the chromospheric Ca II H and K line fluxes are generally adopted. The first is through the classical S index. This is the flux ratio in the core of the Ca II H and K lines to close by continuous windows

$$S = \alpha \frac{H + K}{R + V}, \quad (4.1)$$

where H and K are the line fluxes measured in 1.09Å-wide triangular bandpasses while R and V are estimates of the continuum on either side of the lines measured in 20Å-wide spectral windows centred on 3901Å and 4001Å. α is a normalisation constant dependent on the telescope used to make the measurements, providing a link between samples. The quantity S is sensitive to the integrated emission over these windows and the photospheric radiation transmitted in the H and K passbands. S is, therefore, evolutionary and metallicity dependent, which renders direct comparison of S between different spectral type stars unsuitable. The quantity $\log R_{\text{H},\text{K}}^+$ eliminates this contribution (Lorenzo-Oliveira, Diego et al., 2018, See) and is thus a more reliable measure of

the chromospheric Ca II *H* and *K* flux - therefore more accurately reflecting the magnetic field strength of stars and makes the comparison of magnetic activity of stars of different spectral types suitable.

Another indirect measure of the magnetic field's strength arises from the star's photometric variability. Here we differentiate between the large-scale photometric variability of a star during a magnetic activity cycle, where the average stellar flux of a star increases and decreases on the timescale of years and the variability range of a star due to stellar spots on a rotational time scale. The solar integrated Ca II index, S , correlates linearly with photospheric sunspot number ([Lorenzo-Oliveira et al., 2016](#); [Lorenzo-Oliveira, Diego et al., 2018](#)) established a robust relationship between solar chromospheric activity and the international sunspot number for solar-like stars, suggesting that the two are interconnected. However, whether this correlation is strong enough to derive long-term chromospheric activity cycles similar to photometric cycles on magnetic activity timescales (years) is uncertain. The consistently similar periods of the two relations suggest the two are interconnected - with the faculae or star spot dominance of the magnetic photometric cycles being derived from the expected relation between the two. A star that expresses a larger number of stellar spots will have a more significant photometric variability as a star rotates.

Photometric variability is generally measured through the quantity R_{per} . R_{per} is defined as the median of the range between the 5th and 95th percentile of normalised flux in bins of the light-curve divided into sections of the length of the measured rotational period ([McQuillan et al., 2014](#)). Larger R_{per} stars are expected to have more easily detectable rotation periods because the larger the star's variability as it rotates, the more easily distinguishable this variability is from noise.

Finally, the most recent measure of stellar activity has arisen from the measurement of the fractional spot coverage of stars (See Chapter 3 and ([Cao & Pinsonneault, 2022](#))). They found that fitting APOGEE spectra with two temperature components allows one to infer the surface fractional spot coverage and the temperature contrast of the spots to the ambient surroundings. The fractional stellar spot coverage of a stars is expected to be tied to the photometric variability of those stars with larger photometric variability arising from a larger fractional spot coverage.

All of these measurements of magnetic activity have been shown to be related to each other and follow similar relations with the stellar Rossby number. Magnetic activity indicators saturate below a $R_o < 0.3$ ([Cao & Pinsonneault, 2022](#)) (fast rotation) and decrease with a power law as R_o increases. This relation reflects the decreased probability of observing older slow-rotating stars in the [McQuillan et al. \(2014\)](#) sample. Variations in magnetic activity can therefore indicate variations to the expression of stellar spots and, thus, the observability of stellar rotation.

The magnetic activity also varies with the stellar magnetic cycle of a star, with some scatter to magnetic activity indicators being attributed to this. Therefore, a single temporal measurement of magnetic activity must be treated with care. Variations to the magnetic activity of stars, in a population-wide sense, should be found by the average magnetic activity of a subpopulation. We adopt a population study approach to minimise this effect in this work.

4.3 The gap aligns with a minima in photometric variability

The first mechanism we consider is that the rotation period gap reflects a decrease in photometric variability due to a variation in the magnetic field strength of stars near the gap. We will begin with the 33,000 stars with rotation periods from [McQuillan et al. \(2014\)](#). While this sample has been superseded by other missions in terms of sensitivity, the increase in sensitivity has *not* increased the number of detected rotation periods of cooler stars, particularly where the gap is most apparent. In terms of number of stars, it is still the state-of-the-art mission for precise measurement of the rotation periods of low-mass stars near the intermediate period gap. All stars in this sample lay within the crossmatch with *Gaiadat*a release 3, which contains precise measurements of the $B_P - R_P$ colour, G -band magnitude and distance from parallax. We limit our sample to stars within the nearest 525pc, motivated by the results of [Davenport & Covey \(2018\)](#). While this reduces the sample to 8,594 stars, it ensures that the measured $B_P - R_P$ and rotation periods are as accurate as possible. We made cuts in Gaia DR3 magnitudes and colours using $M_G \geq 0$ and $B_P - R_P \geq 0.8$ to target below the main-sequence turnoff and star's lower mass than the Kraft Break. This leaves us with a sample of 6,243 nearby

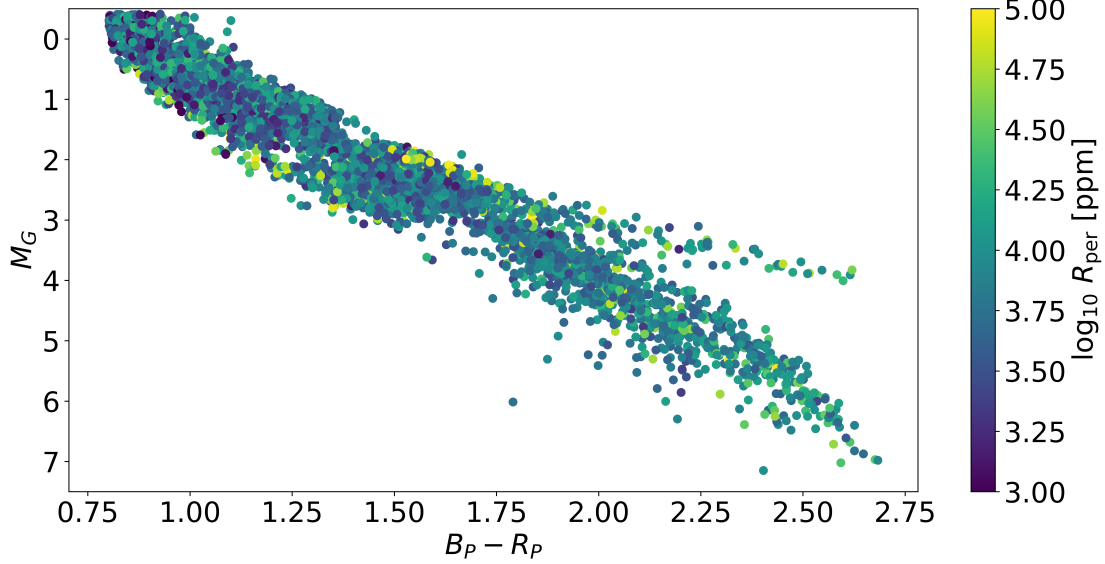


FIGURE 4.1: HR diagram of the closeby rotating main-sequence sample colours by photometric variability (R_{per}).

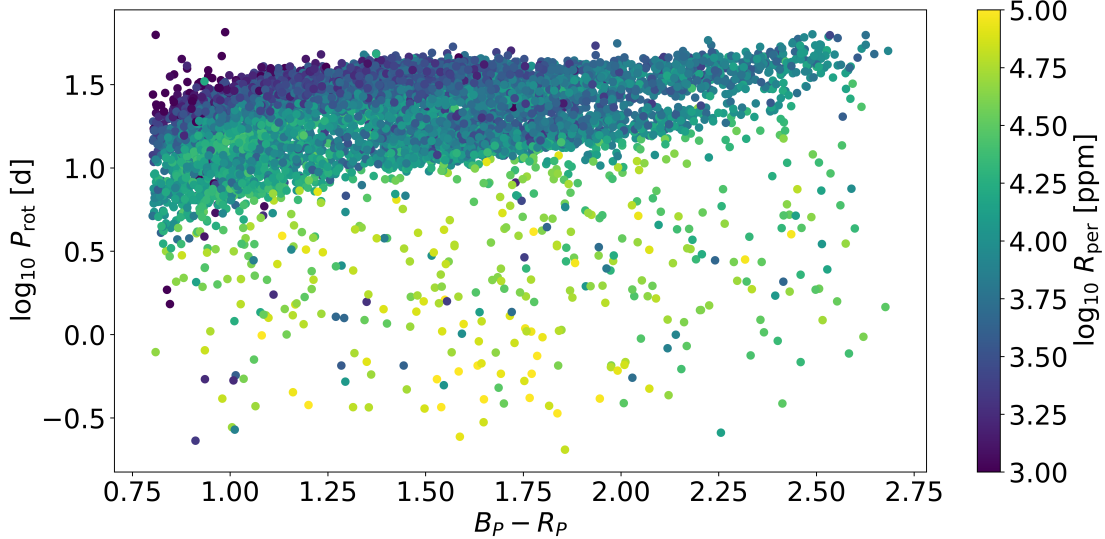


FIGURE 4.2: \log_{10} of the rotation period against $Gaia B_P - R_P$ colour of the closeby rotating main-sequence sample colours by photometric variability (R_{per}). In this Figure, we can see observe the decrease in the photometric variability of stars near the gap.

stars with reliable surface rotation and colour measurements. These measurements are shown in Figures 4.1 and 4.2, where we have plotted them as an Hertzprung-Russel (HR) diagram and log rotation period against $Gaia B_P - R_P$ colour, what we will refer to as the rotational period distribution from in this work. In Figure 4.2 we have also coloured the measurements by the log of R_{per} , which exhibits the decrease in photometric variability surrounding the gap.

From this sample, we can describe the average evolution of photometric variability

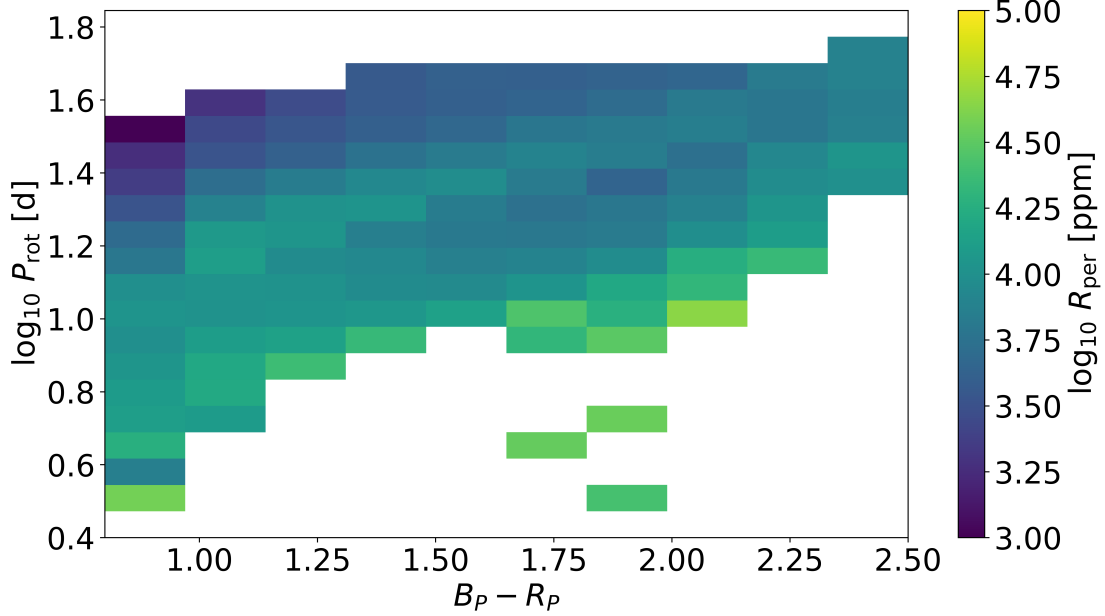


FIGURE 4.3: 2D binned photometric variability (R_{per}) for the slices of \log_{10} of the rotation period and colour $GaiaB_P - R_P$ used in this work. Comparing this Figure and 4.2, the alignment of the minima of photometric variability and observation of stars in the gap can be seen.

around the intermediate period gap. We will first separate the subsample into bins of $B_P - R_P$ (colour) from 0.8-2.5 of size 0.17 (10 bins). In each colour interval, we then split the data into *log* rotational period intervals of width 0.07 dex between 0.4 and 1.8 dex, corresponding to 2.5 and 70 days, respectively. We then compute the median and median absolute deviation of R_{per} in each colour and rotational period bin. The median is used here to attempt to alleviate the effect of activity cycles on the variance of the magnetic activity, and the median absolute deviation establishes the scatter on the measured photometric variability - regions with large median absolute deviation should be treated as less reliable measurements. We neglected the regions with few stars (<5). This removes the spurious stars that have not ascended onto the lower prong of the intermediate period gap, which does not indicate large-scale trends in the data. We reconfirm that R_{per} tends to increase with mass, decrease with the rotational period, and decrease towards the rotational period gap (Reinhold & Hekker, 2020; ?; Santos et al., 2021). Comparing Figures 4.2 and 4.3, we also confirm that the gap aligns itself with a minima in R_{per} .

As a result of the large-scale variability with stellar mass and rotational period, the position of the minima becomes harder to notice as $B_P - R_P$ approaches 0.8. We plot the same data in Figure 4.4 to make the minima more prominent. We show the median

R_{per} (scatter points) and scatter (errorbars) against the \log_{10} of the rotation period for each colour range indicated in brackets - here, the colour of the interval increases down the plot - as well as fitted cubic spline to the data (dashed). From the cubic spline, we can use the first and second derivatives of the spline to accurately determine the position of the local minima in R_{per} , which is indicated by the solid vertical blue line.

The calculation of the position of the minima is an automated process. To identify minima, we calculate the first and second derivatives of the cubic spline fit and find where the first derivative is close to zero and where the second derivative is greater than 5 to ensure we ignore any spurious jitter in the spline fit. We use an automated process to ensure we have not selected a position that we believe aligns with the intermediate period gap. We found that the resulting position of minima can vary slightly depending on the smoothing of the cubic spline and the threshold value chosen for the second derivative. However, the found minima here tended to be robust to variations of the smoothing at that threshold. The first minima, in regards to the rotational period, in the $B_P - R_P = (0.8-0.97)$ bin was also manually ignored.

The position of the minima are shown in blue in Figure 4.5, where it is clear that the majority of minima align with the intermediate period gap. We note that the minima do not accurately predict the position of the intermediate period gap for $B_P - R_P \geq 2.16$. We believe this is because of the small number of stars below the gap in this colour range which were cut due to them not containing enough stars. With larger numbers of observations of low-mass stars below the gap we believe our prediction of the position of the rotation period gap with R_{per} would be more accurate in this regime. We also note that the average photometric modulation amplitude tends to peak to a maximum with a larger R_{per} than stars on the lower prong of the rotational period gap despite having longer rotation periods. Whether this peak is indicative of stronger photometric activity suddenly above the gap or of suppression of photometric activity below the gap is unknown.

A possible explanation for the decrease in median photometric variability comes from the nature of a dearth of observations, as the gap is not horizontally aligned and increases in period for stars of lower mass (higher $B_P - R_P$). R_{per} generally decreases with mass and rotation period. Taking the median value in slices of constant rotation period near the dearth of observations will be systematically biased in different ways as it passes

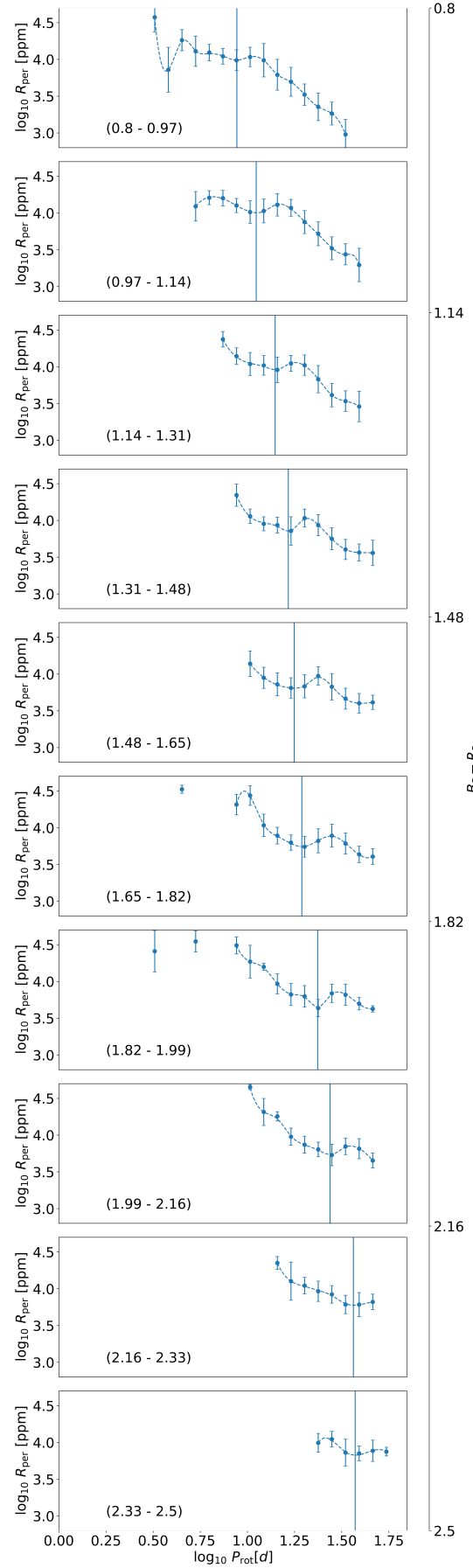


FIGURE 4.4: Median and median absolute deviation of photometric variability (R_{per}) against \log_{10} of the rotation period in bins of and colour $Gaia B_P - R_P$ (indicated in brackets). Here we have fitted a cubic spline to median R_{per} and calculated minima using the first and second derivatives of the fitted cubic spline. Solid vertical blue lines show the minima here. These minima align with the rotational period gap.

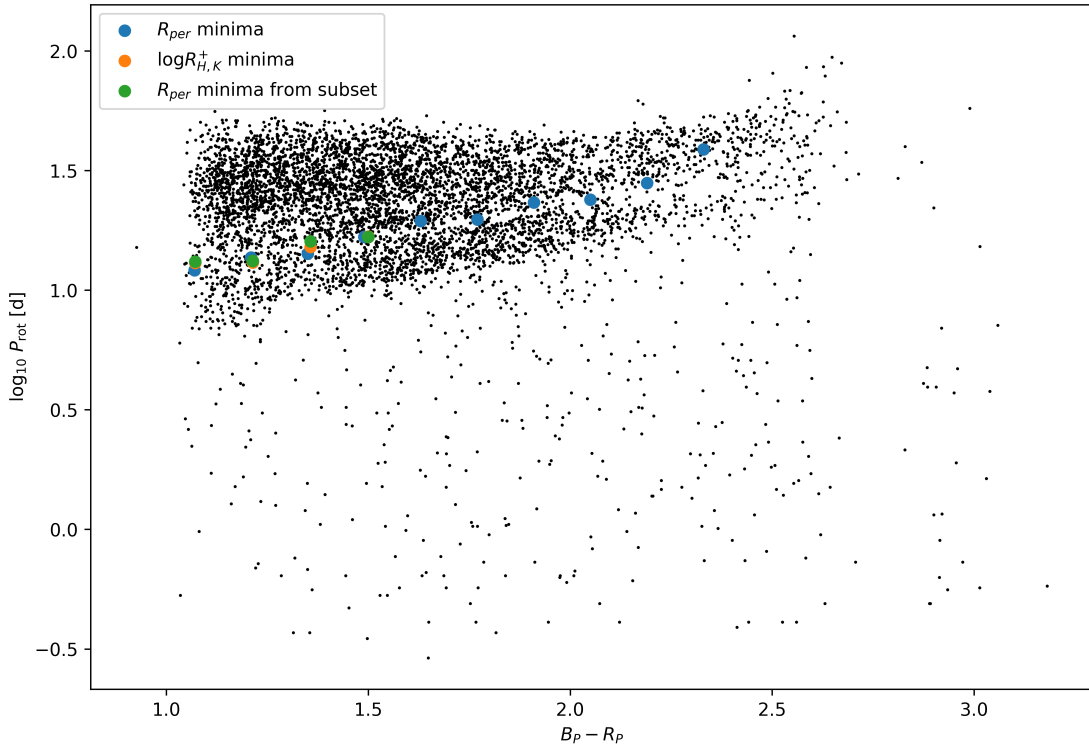


FIGURE 4.5: The position of the identified minima in R_{per} against rotational period using the full close-by rotating main-sequence Kepler sample, the R_{per} minima identified with the Kepler LAMOST crossmatch and the $\log_{10} R_{H,K}^+$ minima identified with the Kepler LAMOST crossmatch.

through the dearth. In order of increasing rotation period, a sample of stars in each bin of rotation period will contain (1) majority fast rotating but redder stars and a small number of slow-rotating bluer stars, (2) approximately equal fast-rotating red stars and slow-rotating blue stars, and finally (3) majority slow-rotating bluer stars and a small number of fast-rotating redder stars. The relationship between the R_{per} and mass or rotation period are not easily parameterised - especially near the gap. However, we can confirm that this effect does not skew our results by calculating the median and median absolute deviation of $B_P - R_P$ in each colour and rotational period bin. We have shown this in Figure 4.6. We confirm that the minima and maxima of R_{per} with rotation period in each colour bin do not correspond to minima or maxima in colour that would indicate that this effect is at play. The variation in R_{per} is, therefore, a physical effect that aligns itself with the rotational period gap.

At first glance, the minima in R_{per} surrounding the gap suggests that the rotation period gap is the result of the decreased probability of observing stars at the given rotation period. However, the minima values of R_{per} within the gap can otherwise be detected

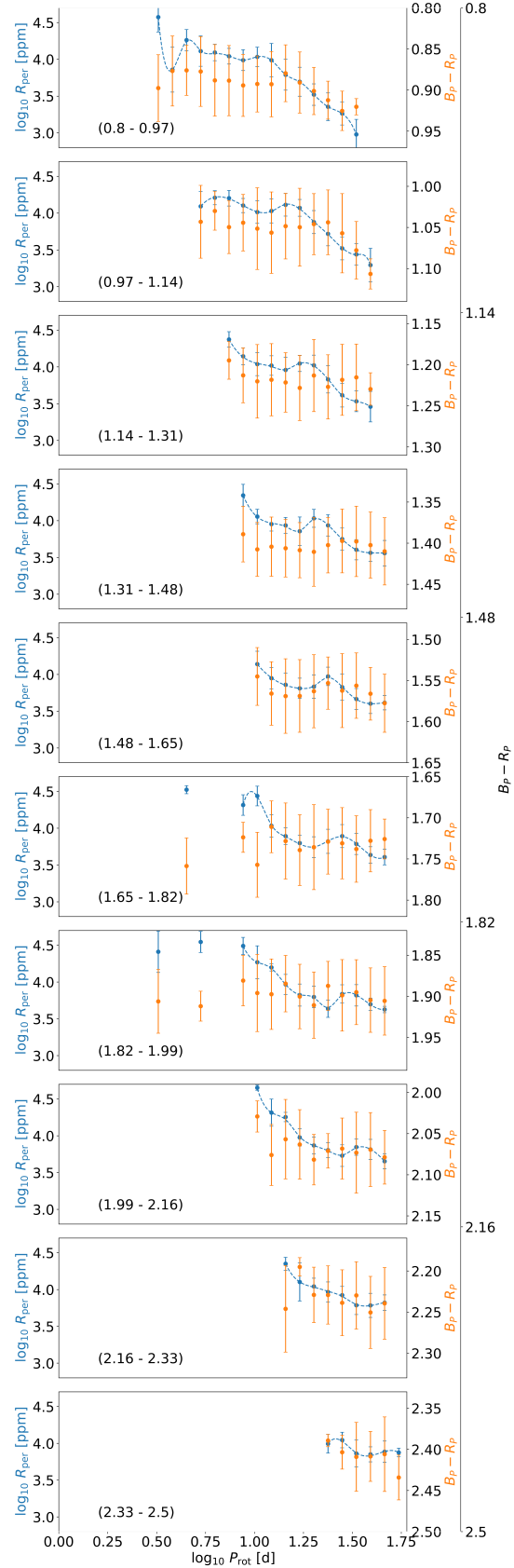


FIGURE 4.6: Median and median absolute deviation of photometric variability (R_{per}) (blue) and $B_P - R_P$ (orange) against \log_{10} of the rotation period in bins of $B_P - R_P$ colour (indicated in brackets). The position of the minima in R_{per} do not align with maxima or minima in $B_P - R_P$ implying that the colour bias when fitting across the dearth can be the cause of the R_{per} minima.

for other colour stars. For example, the minima in the $B_P - R_P$ - (0.97-1.14) slice has a R_{per} value of ~ 4.0 , which can otherwise be easily detected for slower rotating or redder stars. This either suggests that the periodic variability drops suddenly to levels where rotation is not measurable at the rotation period gap or that the rotational variability drops due to the process by which stars cross the gap. Santos et al. (2021) increased the sensitivity of period detection for *Kepler* lightcurves and did not increase the number of stars observed near the intermediate period gap - suggesting that the drop in photometric variability does not result in a decreased probability of observing stars near the gap. This implies that if the drop in photometric variability is not the cause for the dearth of observations near the rotational period gap and rather that the drop in photometric variability is purely coincident with the rotational period gap - suggesting that the mechanism underlying the two observations is the same. R_{per} is not defined for stars where rotation is not detected - as R_{per} is defined by the photometric variability range over a rotational period timescale. Therefore we do not know whether the potential stars that lay within the gap, which we cannot observe because of the supposed dramatic decrease in R_{per} , do or do not suddenly decrease in R_{per} .

4.4 The gap aligns with a minima in $\log R_{HK}^+$

While it has been well established that the photometric variability of stars decreases towards the intermediate period gap other magnetic activity indicators have not been explored in this regard, only the large-scale trends with stellar mass and rotation (Zhang et al., 2020). Suppose other magnetic activity indicators vary in the same fashion as R_{per} - decreasing to a minimum at the rotational period gap. In that case, it is more likely that the decrease in R_{per} towards the gap results from a variation in the magnetic field of stars. We will begin by testing whether this is indeed the case.

Zhang et al. (2020) extracted the chromospheric magnetic activity indexes, S and $\log R_{HK}^+$, for 59,816 stars from low-resolution LAMOST spectra in the LAMOST-Kepler program. The crossmatch of their work with the nearby rotating main sequence we established yielded 1060 stars. The stars in the crossmatch tend to be the higher mass, brighter stars with $B_P - R_P < 1.8$, where the intermediate period gap is less apparent. Given that we could predict the gap position for these stars in our earlier experiment, we carry forward and re-analyse their data under a new framework.

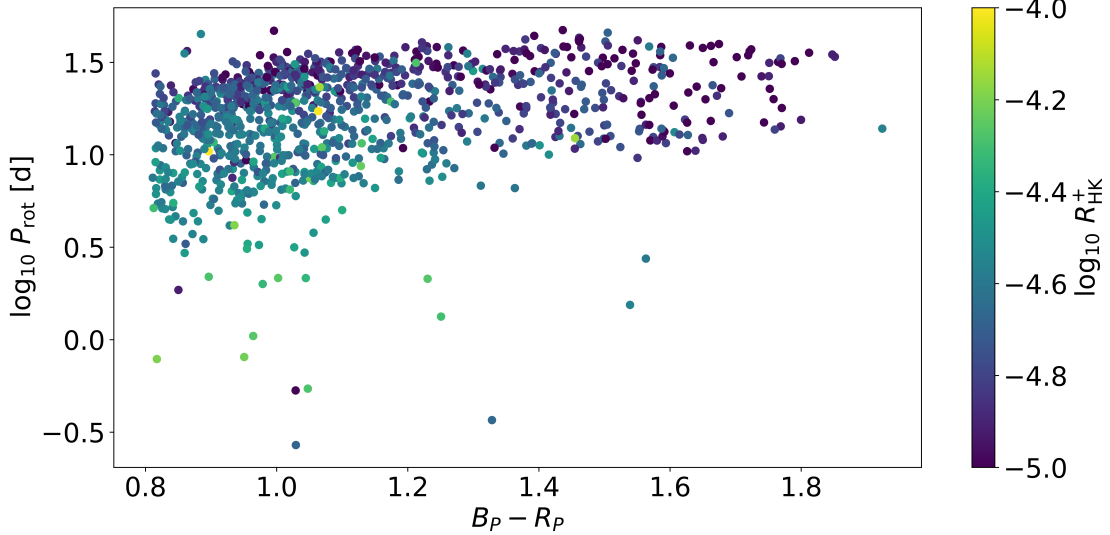


FIGURE 4.7: The LAMOST chromospherically active and *Kepler* rotating closeby, main-sequence cross-match \log_{10} of rotational period \log_{10} against $Gaia B_P - R_P$ colour coloured by $\log_{10} R_{HK}^+$. It is unclear from this whether $\log_{10} R_{HK}^+$ decreases toward the gap like R_{per} .

$\log R_{HK}^+$ provides a more accurate measure of the chromospheric magnetic activity than S , which is uncoupled from a radiative contribution, so we adopt $\log R_{HK}^+$ in this work. The resulting rotational distribution of stars is shown in Figure 4.7 coloured by $\log R_{HK}^+$. Due to the smaller number of stars and lower precision of $\log R_{HK}^+$ than R_{per} it is not clear whether $\log R_{HK}^+$, like R_{per} decreases towards the intermediate period gap.

To determine this more concretely, we adopt the same process as we described earlier to find the minima in R_{per} in a bin of colour against the rotational period. We again separate the stars into the same slices of $B_P - R_P$ and log of rotation period, and remove any bins containing small numbers of stars (< 2). This cut-off was chosen because of the reduced number of stars in the sample *Kepler*-LAMOST crossmatch, compared to the [McQuillan et al. \(2014\)](#) sample. Still, the results should be treated with more caution because we rely on small number statistics. The median and median absolute deviation of both $\log R_{HK}^+$ and R_{per} in these slices was then calculated, which we then fit with cubic splines against the log of the rotation period. We have repeated this method on R_{per} here because we are using a subset of the original stars and to compare the recovered minima from the subset more accurately - this also allows us to confirm the accuracy of the fit of our minima in the first test. The minima of the cubic spline fits are then calculated again using the first and second derivatives using the same smoothing and first and second derivative thresholds.

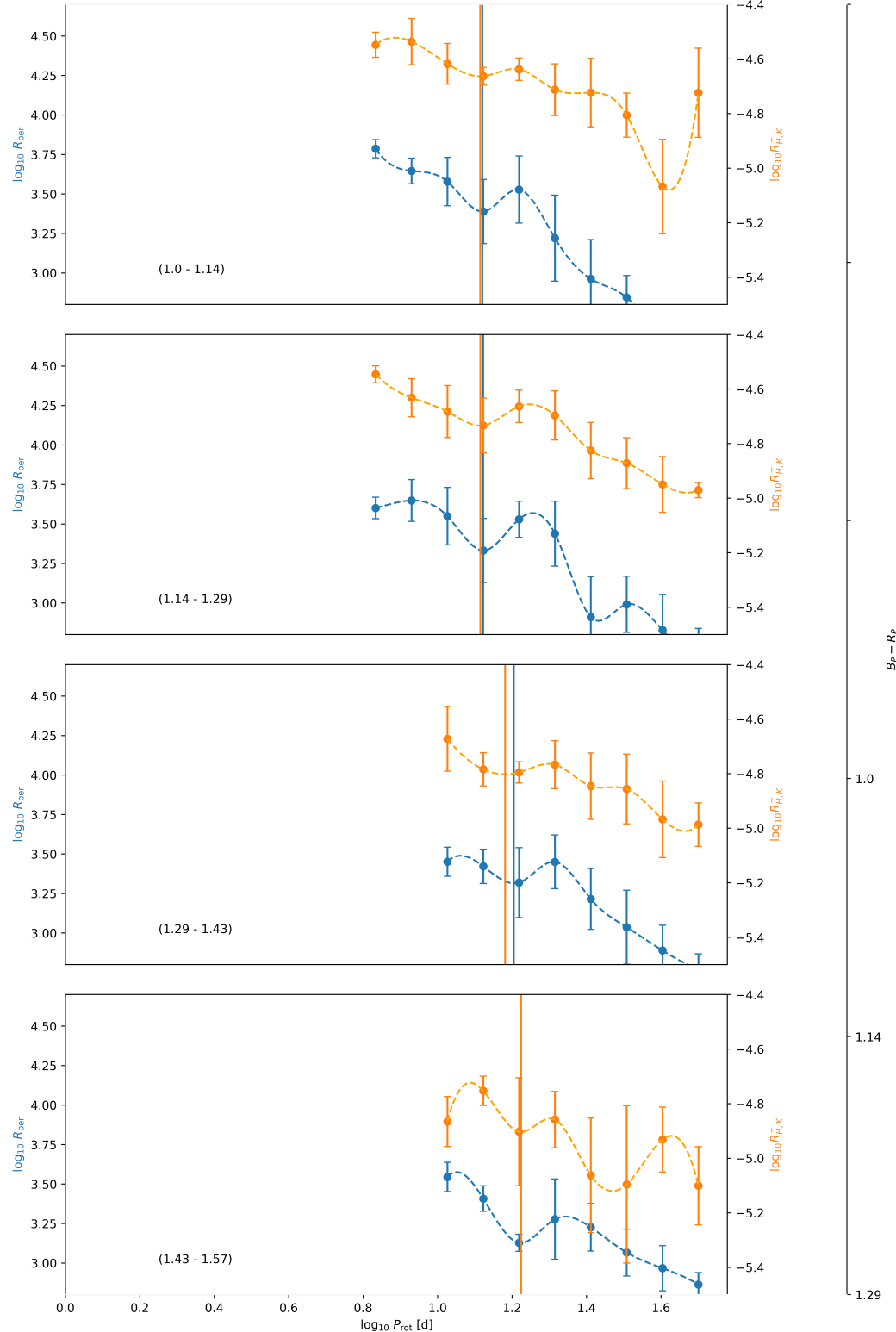


FIGURE 4.8: Median and median absolute deviation of photometric variability (R_{per}) (blue) and LAMOST $\log_{10} R_{\text{HK}}^+$ against \log_{10} of the rotation period in bins of and colour $Gaia B_P - R_P$ (indicated in brackets). Here we have fitted a cubic spline to the median of these values in each bin and calculated minima using the first and second derivatives of the fitted cubic spline. The minima in R_{per} are shown by solid vertical blue lines, while the minima in $\log_{10} R_{\text{HK}}^+$ are shown in solid vertical orange lines. These minima align with each other and the rotational period gap.

We compare the distributions of R_{per} and $\log R_{HK}^+$ against the log of rotation period in Figure 4.8 and show the found minima in blue and orange solid vertical lines for R_{per} and $\log R_{HK}^+$ respectively. Like photometric variability, $\log R_{HK}^+$ tends to decrease with rotational period - owing to their relation to the strength of the magnetic field. We find that, generally, R_{per} and $\log R_{HK}^+$ are directly tied - increases and decreases to the median value with rotational period in one tends to align with a similar response in the other.

We show the comparison of the recovered minima from R_{per} using this subset as well as the minima recovered using $\log R_{HK}^+$ in Figure 4.5. The recovered R_{per} minima using the subset lay on top of the R_{per} minima recovered using the full sample. Interestingly, we may detect previously unreported minima in $\log R_{HK}^+$ close to the rotation period gap. Excluding the minima recovered in the $B_P - R_P$ - (0.8-0.97) bins, the minima that we recover in $\log R_{HK}^+$ against logged rotational period are in the same period bin and are close in position to the minima of R_{per} we recover, which we have established aligns with the intermediate period gap. The alignment of the minima is also robust to variation in the smoothness of the fitted cubic spline - suggesting that the minima are not spurious.

Measurements of $\log R_{HK}^+$ are less precise than R_{per} , which is reflected in the relatively larger median absolute deviation. The detection of the coincidence in a single slice of $B_P - R_P$ could be explained through this imprecision. Alternatively, the coincidence of the two may simply be a coincidence. Detecting this in multiple slices of $B_P - R_P$ suggests that the cause of the minima is related. Further study of this relationship is required to confirm the coincidence of the minima with a larger dataset of chromospheric magnetic activity indicators or with other magnetic activity indicators. We will assume, for now, that the rotational period gap does align itself with minima in both R_{per} and $\log R_{HK}^+$ and explore whether there is a sample of low-magnetic activity, non-detected rotators.

4.5 Is there a sample of low-magnetic activity stars without rotational period detection?

If the gap contains stars that have dramatically low R_{per} and thus do not have detectable rotation periods, then $\log R_{HK}^+$ should also dramatically drop within this regime. If there is a sample of dramatically lower $\log R_{HK}^+$ stars without detected rotation periods, then the existence of such a subsample would support the hypothesis that the intermediate period gap results from a decreased probability of observing stars at those rotation periods due to a decrease in stellar activity.

We will compare the $\log R_{HK}^+$ distributions of the [McQuillan et al. \(2014\)](#) rotating and non-rotating samples. We prepare the sample of 99,000 stars without detected rotation periods from their work² in the same way that we did for the rotating sample - ensuring they are close by ($< 525pc$), on the main-sequence and redder than $B_P - R_P = 0.8$ where the rotational period gap is most apparent. This leaves us with a sample of 5574 non-rotating close by, main-sequence stars, which we can cross match with the LAMOST-Kepler sample of chromospheric active stars measured in [Zhang et al. \(2020\)](#) - reducing the number of stars to 1134 stars. The number of stars in this sample is similar to that in the rotating sample. We show the resulting HR diagram of stars without rotational detection (bottom) and with rotational detection (top) in Figure 4.9 coloured by $\log R_{HK}^+$. Comparing the distributions, it is clear that the non-rotating sample is clearly biased for higher mass stars and does not permeate into the low mass regime, where the gap would be most apparent.

With the rotating and non-rotating LAMOST-Kepler samples we can investigate the detectability of rotation as a function of $\log R_{HK}^+$. We expect more magnetically active stars (higher $\log R_{HK}^+$) to be easier to detect in rotation as R_{per} should increase in turn - however, as we have noted earlier in this work, stars can have their rotation go undetected for a multitude of reasons and the non-detection of rotation will not purely be the result of lower magnetic activity. Figure 4.10 shows the distribution of rotation detected and rotation non-detected samples with $\log R_{HK}^+$. The left panel shows the probability density, while the right shows the cumulative probability density function.

²This is a slight misnomer as *some* of the stars $\sim 100,000$ stars have detectable rotation periods, but do not pass a detectability threshold, see Section A in the appendix of their work, and those periods should be treated with some care.

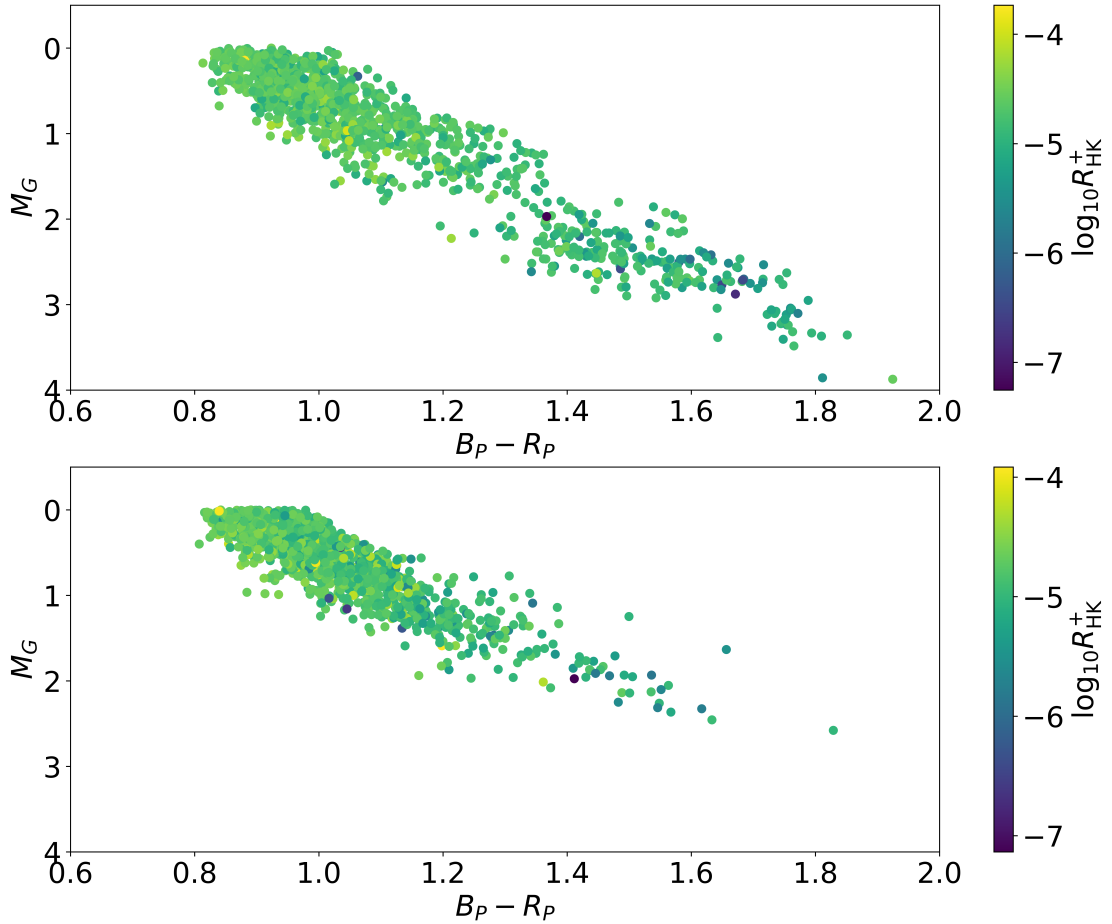


FIGURE 4.9: HR diagram of the closeby rotating (top) and non-rotating (bottom) main-sequence sample crossmatched with the LAMOST-Kepler field coloured by the chromospheric magnetic activity indicator $\log R_{HK}^+$. Comparing these two samples, we observe very few low-mass stars for which the rotation period is undetected.

Stars detected in rotation appear to have higher $\log R_{HK}^+$ than those without detection. A Kolmogorov-Smirnov (KS) test returns a p -value of $4 \cdot 10^{-15}$. With this, we can reject the null hypothesis that the two samples are drawn from the same underlying distribution with strong statistical significance. The non-rotation detected tends to be less magnetically active, in terms of $\log R_{HK}^+$, than the rotationally detected sample which aligns with our general expectations. Less magnetically active stars tend to have a lower detection rate due to the decrease in prominence of stellar spots with lowering magnetic activity.

To investigate the detectability of rotation, let us consider the fraction of targets for which we detected periods in bins of colour and $\log R_{HK}^+$. The detection efficiency here is measured from the ratio of the number of stars with a measured rotation rate to the total number of stars in that bin. Other works (Claytor et al., 2022, See e.g.)

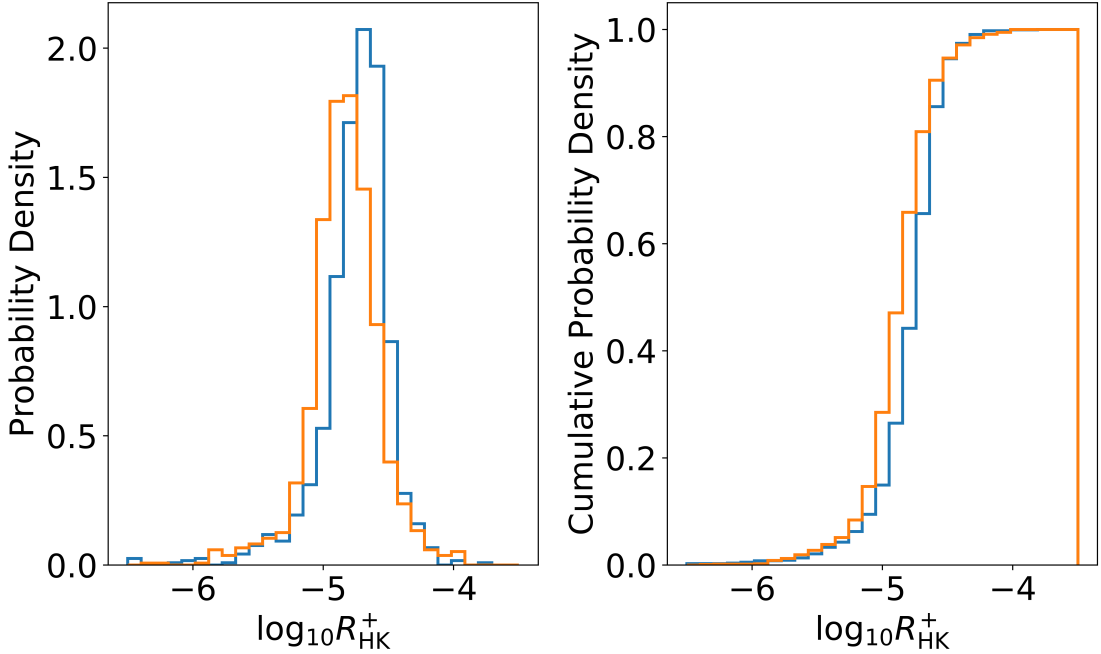


FIGURE 4.10: The probability density function (left) and cumulative probability density function (right) of $\log R_{HK}^+$ are separated by whether rotation was or was not detected in the close-by main-sequence LAMOST-Kepler crossmatch. We expect less magnetically active stars to have a lower detection rate due to the decrease in prominence of stellar spots with lowering magnetic activity. This is supported by the data here as the non-rotation detected sample contains a larger number of low $\log R_{HK}^+$ stars.

consider the ratio of stars with highly precise rotation period measures to those without. We forgo any cuts to the fractional error on the rotational period as we have limited our stars to nearby stars, which should have very high precision recovery of the stellar rotation period, and we also make no cuts to the number of stars in each bin that we calculate the histogram for. While limiting the minimum number of stars would allow us to clarify large-scale trends, we are searching for a subsample of stars with spuriously low magnetic activity with an already small sample size.

Figure 4.11 shows the detection fraction (top) and a 2D histogram of the non-detected rotation sub-sample (bottom) against colour and $\log R_{HK}^+$. We confirm that rotation is preferentially measured in stars with higher magnetic activity (larger $\log R_{HK}^+$) and tends to increase with colour. Low-mass stars have a high probability of rotation being measured. If we assume that stars of the same $\log R_{HK}^+$ express the same number of stellar spots, then dimmer stars will express larger R_{per} and thus will have a higher detectability of rotation. We do not observe an ultra-low magnetic activity population with undetected rotation that would be required to explain the lack of observation of

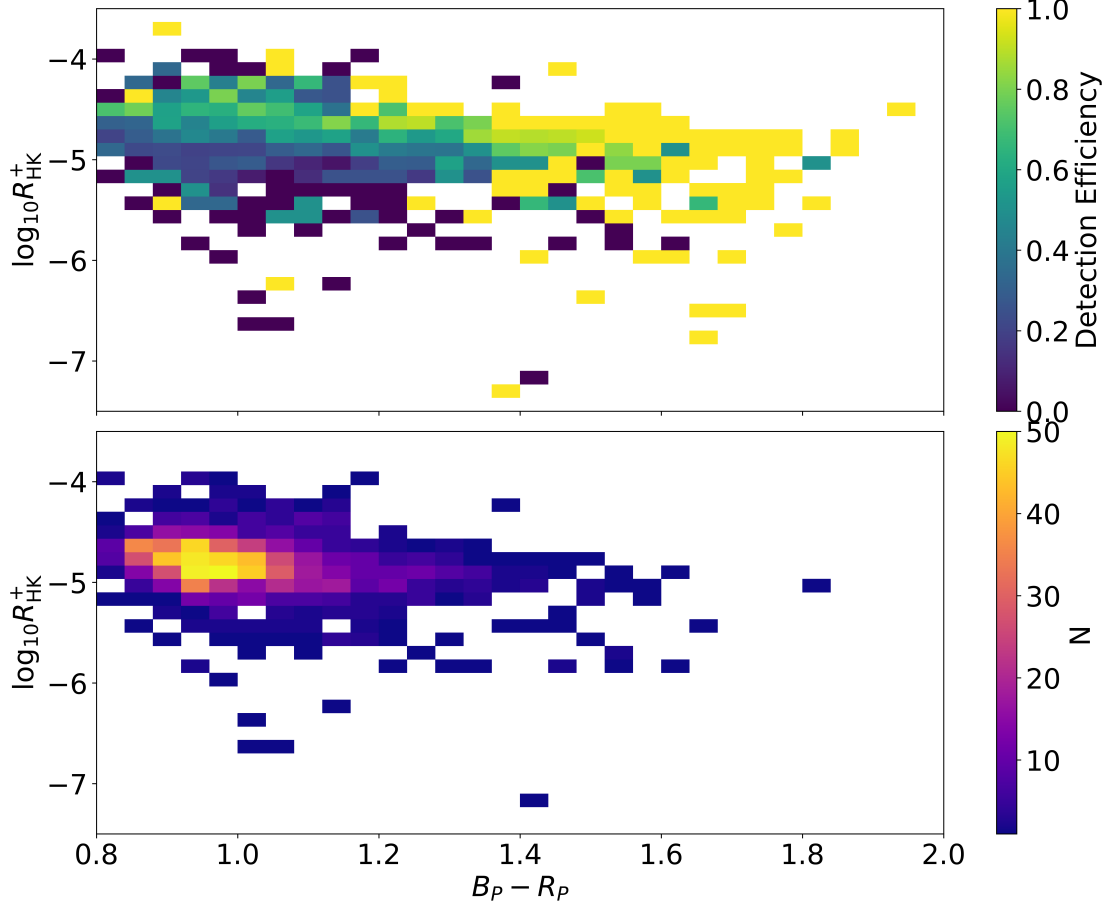


FIGURE 4.11: The detectability of rotation (top) and 2D histogram of stars without detected rotation periods (bottom) across Gaia $B_P - R_P$ colour and $\log R_{HK}^+$. Rotation is preferentially measured in stars with higher magnetic activity (larger $\log R_{HK}^+$) and tends to increase with colour. Low-mass stars have a high probability of rotation being measured. Stars with low magnetic activity have a lower likelihood of rotational observation. Bins with detection efficiency equal to zero or one tend to contain single stars, with detected rotation or without detected rotation, respectively and are not indicative of trends in the detection efficiency. We do not observe an ultra-low magnetic activity population with non-detected rotation that would be required to explain the lack of observation of stars in the intermediate period gap. While there are stars with ultra-low $\log R_{HK}^+$ (< 5.5) in each $B_P - R_P$ bin they can either both rotationally detected or not rotationally detected. The ultra-low magnetic activity does not indicate their lack of rotational observation probability.

stars in the intermediate period gap. While there are stars with low, for a given colour bin, and ultra low $\log R_{HK}^+$ (< 5.5) in each $B_P - R_P$ bin, stars in those bins can both be rotationally detected or not rotationally detected. Ultra-low magnetic activity does not indicate their lack of probability of rotational observation, and there is no subsample of ultra-low magnetic activity stars without detected rotation periods. While stars older-slowly rotating stars also tend to have lower $\log R_{HK}^+$, which may camouflage a population of low $\log R_{HK}^+$ gap stars, they still tend to have observable rotation

periods. For the gap to exist the magnetic activity would need to drop to a point where observation of rotation period is impossible, which is not supported by the data here.

Section The lack of observation of stars that could fill the intermediate period gap

For the hypothesis that the gap represents a minimum of stellar rotational period detection and that the gap is indeed full of stars, then must be enough stars without detected rotation periods to fill the shortage of observations. In this Section, we will determine whether this is indeed the case.

We will assume that the multiple missions that have observed the rotation period gap (*Kepler*, *K2*, *ZTF*, *TESS*) missions are not biased away from observing stars within the rotation period gap and compare the distribution of stars in the [McQuillan et al. \(2014\)](#) *Kepler* rotating and undetected rotating samples. Further, this analysis will focus on very low-mass stars where the gap is most apparent - where [McQuillan et al. \(2014\)](#) remains the state-of-the-art in detecting rotational periods for low-mass stars near the gap. We make no quality cuts to the data to ensure we are not preferentially selecting for stars that could/could not possibly fill the gap.

If we compare the distribution of the number of stars in the rotation detected and undetected samples with colour, as we have shown in Figure 4.12, we observe that stars with detectable rotation periods outnumber stars with undetectable rotation periods at lower masses ($B_P - R_P \geq 1.3$), despite the overall 3:1 ratio of the detectable rotation period to undetectable period catalogues. In the inset of this Figure, where we compare the distributions where the gap is most apparent, we see that the proportion of stars with undetectable rotation periods to stars with detectable rotation periods decreases with decreasing mass, to a minimum of 1:10 undetectable to detectable rotation periods at the lowest masses. This suggests that there are not a large number of stars available to fill the rotational period gap.

We will more concretely investigate this by determining how many stars would be required to fill the gap - or rather for the dearth in observations to be undetectable in the low mass range where the proportion of stars between the samples is largest and where the gap is most apparent ($B_P - R_P \geq 1.5$). To find the number of stars required for the dearth of observations to be no longer considered a dearth we first separate the sample with detected rotation into bins of $B_P - R_P$ from 1.5-2.2 of size 0.045 (15 bins).

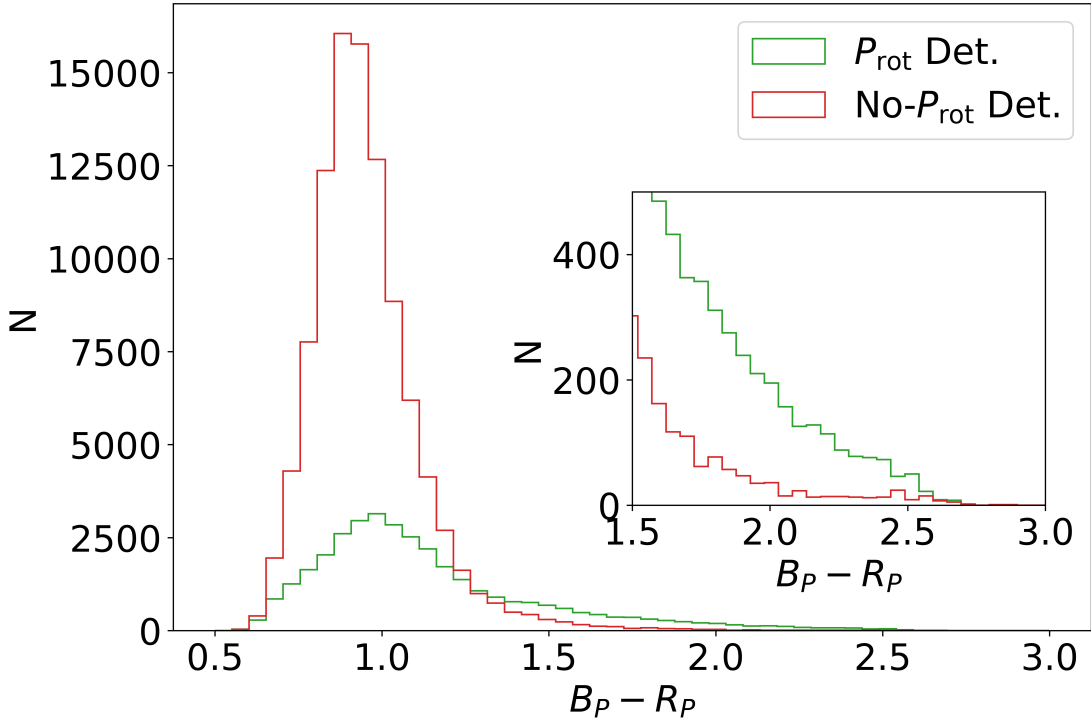


FIGURE 4.12: A histogram of the distribution of $B_P - R_P$ colour of stars with (green) and without (red) detected rotation periods. **Inset:** A zoom-in of the distribution for $B_P - R_P \geq 1.5$ where the rotational period gap is most apparent. The distribution in colour of stars with and without detected rotation periods vary. The undetected rotation sample is strongly biased towards stars with $B_P - R_P$ close to 1, comparative to the lower-mass stars where the number of stars drops quickly. Despite the $\sim 3:1$ ratio of the number of stars with undetected rotation periods to those with detected rotation periods, the number of stars without detected rotation periods drops below those with detected rotation at $B_P - R_P \geq 1.3$.

In each colour interval, we then split the data into log rotational period intervals of width 0.07 dex between 1.0 and 1.7 dex (10 bins) - which correspond to 10 and 50 days, respectively. We then calculate the number of stars in each slice of log period for a given colour range. In Figure 4.13 we show the number of stars in each slice (scatter points) against \log_{10} of the rotation period for each colour range indicated in brackets to which we have fit a cubic spline (dashed). From the cubic spline, we determine the position of the local minima in number of stars with detected rotation period, which is indicated by the solid vertical black line. The calculation of the position of the minima is again an automated process as carried out in the previous Sections. To calculate the number of stars required for the dearth, we compare the average of the two scatter bins surrounding the closest bin of the minima position. While this approach is admittedly naive, as it assumes all of the stars will be in the bin closest to the minima rather than being distributed throughout the dearth region, it places a lower bound on the stars

required to fill the gap.

In Figure 4.14 we compare the number of stars required to fill the gap to the number of stars without detected rotation periods in each colour range. The number of stars required to fill the gap is approximately constant at $N \sim 20$. This suggests that the number of stars required gap is independent of the total number of stars observed in that mass range. Suppose the gap is full of stars without detectable rotation periods. In that case, we expect the proportion of stars required to fill the gap to increase proportionate to the total number of stars (detected and non-detected rotation), but this is not the case. The number of stars required to fill the gap is much smaller than the number of stars without detected rotation periods for $B_P - R_P < 1.8$. Still, as colour increases and the number of observed (detected rotation period stars) stars decrease, the number of stars required to fill the gap becomes the majority of stars without detected rotation periods. This suggests that for the gap to be full of stars with undetectable rotational period stars, all of the stars in the undetected rotational period sample would need to be in this small rotational period range, and only a very small number of stars with undetectable rotation are the result of noise or inclination effects. The requirement of most (if not all) stars within the undetected rotation period sample suggests that the gap is not full of stars with undetectable rotation.

4.6 Latitudinal differential rotation

We have proposed in this work that there is a lack of evidence to suggest that the rotational period gap represents a regime of evolution by which stars have low detectability due to low stellar activity. The only other proposed mechanism to explain the gap arises from extreme wind braking, causing stars to spin down quickly across the gap. Leaving that explanation for the coming Section, we propose a previously uninvoked mechanism to consider: the onset of latitudinal differential rotation. Stars, most concretely for the Sun, have been observed to express latitudinal differential rotation. Further, stars express latitudinally distributed spots across their surface. The observed rotation rate of stars from stellar spots is generally taken as the average rotation rate across the surface of a star Santos et al. (2021). If a star swiftly transitioned from flat to latitudinally differentially rotating, then the observed average rotation rate could change significantly.

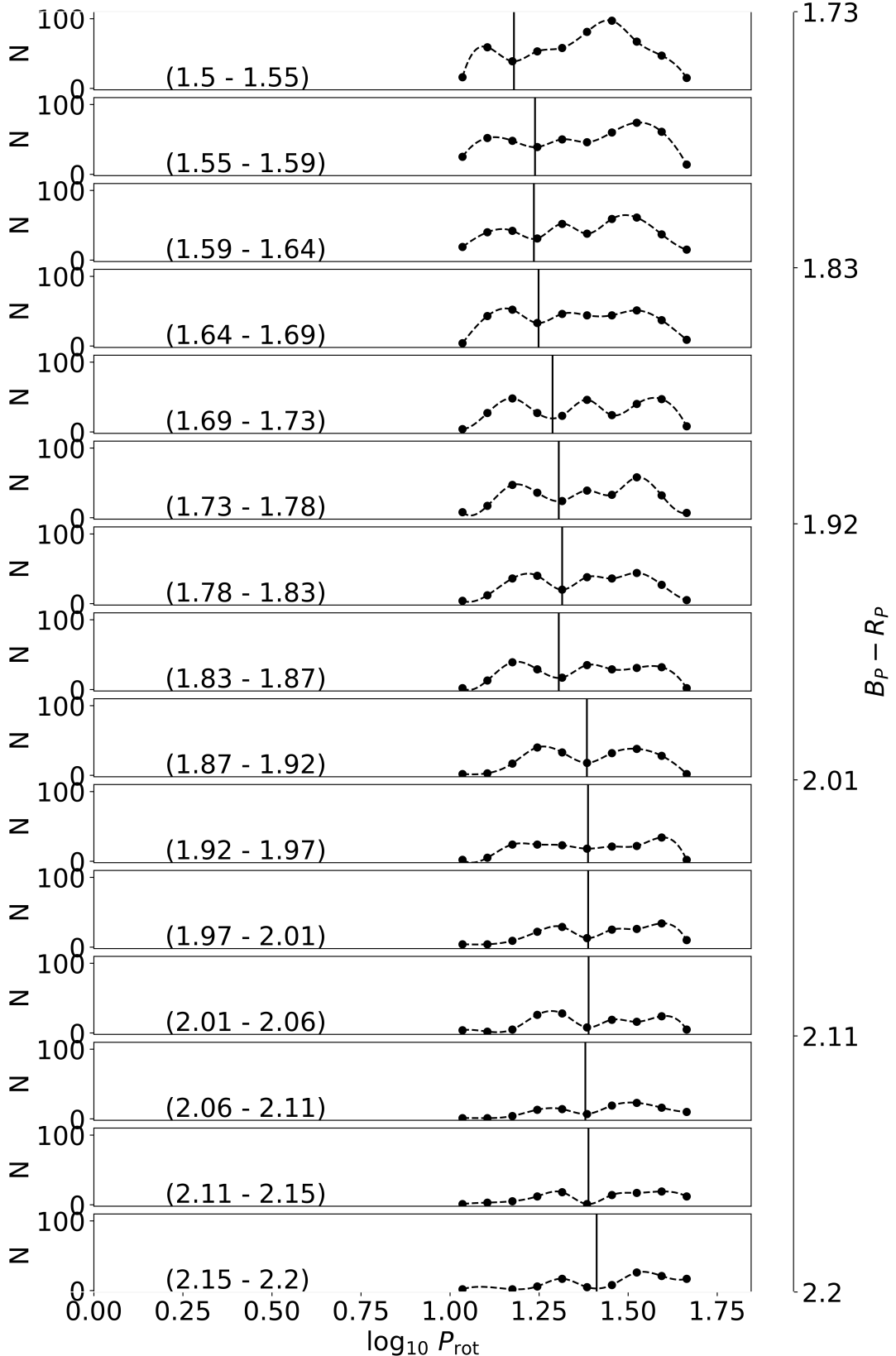


FIGURE 4.13: Number of stars in each bin against \log_{10} of the rotation period in bins of colour $Gaia B_P - R_P$ (indicated in brackets). Here we have fitted a cubic spline to the number of stars in each bin and calculated minima using the first and second derivatives of the fitted cubic spline. Solid vertical black lines show the minima in number of stars. These minima are the rotational period gap.

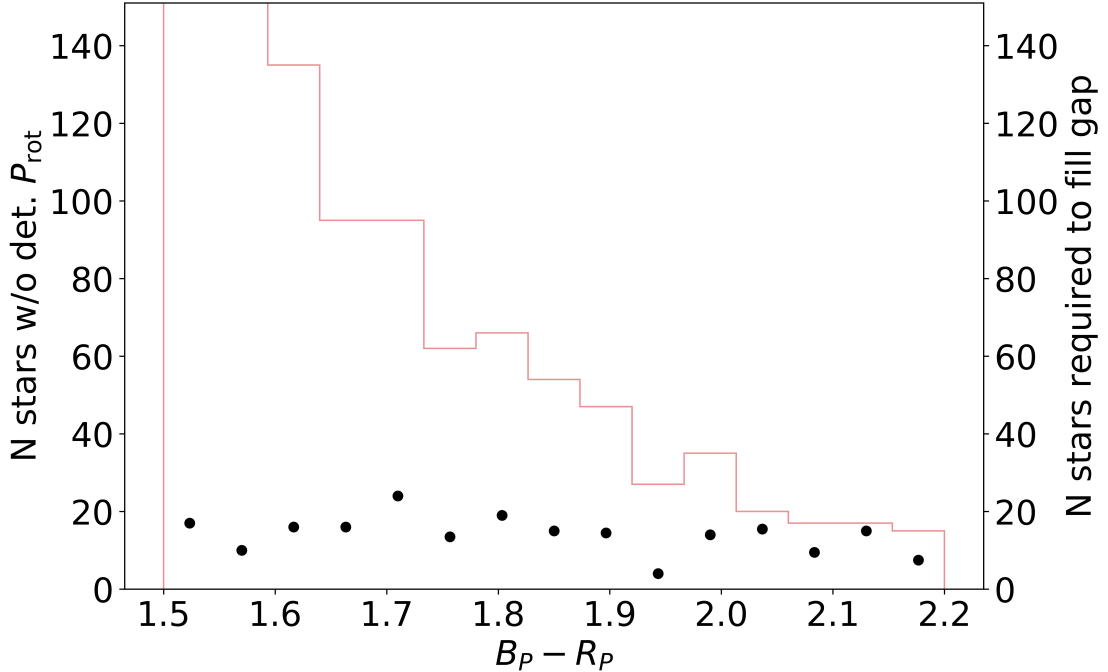


FIGURE 4.14: The number of stars required to fill the gap (black scatter points) against the number of stars with undetected rotation periods against $B_P - R_P$. The number of stars required to fill the intermediate period gap is roughly constant at $N \sim 20$. While the number of stars without detected rotation greatly outnumbers the number required to fill the gap below $B_P - R_P \sim 1.8$, the two are almost equal for lower mass stars.

Benomar et al. (2015); Benomar et al. (2018); Bazot et al. (2019); Hall et al. (2021), for example, have measured the differential rotation of main-sequence solar-like, in terms of mass and rotation rate, stars through asteroseismology. Within their sample Bazot et al. (2019) found that every star in their sample expressed evidence of latitudinal differential rotation that is equator-fast (colloquially known as solar-like). Saar (2011) performed observations of the latitudinal differential rotation of single main-sequence stars from Ca II HK P_{rot} variations (Donahue et al., 1996, e.g.) and photometric P_{rot} variations (Messina & Guinan, 2003, e.g.). They found that fast-rotating stars ($R_o < 0.45$) support quenched - latitudinally flat ³ - rotation profiles, which increase in scale of differential rotation, which they measure as the rotation rate difference between the equator and at a latitude of 60° , proportional to the Rossby number

$$\frac{|d\Omega|}{\Omega} \propto R_o^2 \quad (4.2)$$

Intermediate rotating stars $0.45 \leq R_o \leq 2$ support solar-like (equator fast) differential rotation and slow rotators ($R_o \geq 2$) support anti-solar (pole fast) rotation. They argue

³or rather, close to latitudinally flat

that in both of these regimes, the scale of differential rotation is constant - $\frac{|d\Omega|}{\Omega} \sim 0.2$ - but that the sign of the differential rotation changes suddenly at $R_o \sim 2$. [Brun et al. \(2022\)](#) showed, through 2-D magnetohydrodynamic simulations, that the presence of a magnetic field inhibits the growth of differential rotation for fast rotators. They suggest that the growth of differential rotation for fast rotators could scale with $\frac{|d\Omega|}{\Omega} \propto R_o^p$, where p could take any value between 2 and 6. They also tentatively argue for the growth of the scale of differential rotation for anti-solar rotators proportional to the square of the Rossby number.

Interestingly the transition from latitudinally flat rotation profiles, to equator fast rotation profiles occurs near $R_o \sim 0.5$ - the Rossby number where the rotational period gap occurs. If latitudinal differential rotation becomes significant at this point in the evolution of rotation of a star, then the rotation period gap may reflect a sudden increase in average, and thus observed, surface rotation period from that onset. We consider this as the mechanism underlying the intermediate period gap by investigating an observationally motivated observed rotation period distribution under the proposed differential rotation relationships proposed by [Saar \(2011\)](#) and [Brun et al. \(2022\)](#)

We generate 40,000 main-sequence and early post-main-sequence stars with various values of mass, age, metallicity and rotations rate. We drew masses from a uniform mass function between 0.5 and 1. This limits our range of masses to those with a radiative surface and convective core and especially targets stars where the rotational period gap is most apparent. We have not assumed an initial mass function here - this is because the *Kepler* sample is biased towards brighter high-mass stars, which we assume here effectively cancels out, say, a Saltpeter IMFs bias towards a larger number of low-mass stars.

Metallicity is drawn from a distribution to approximately reflect what is observed in the Milky Way. Specifically, we defined a variable ϕ to be drawn from a Beta distribution

$$\phi \sim \mathcal{B}(\alpha = 10, \beta = 2) \quad (4.3)$$

and applied a transform from ϕ to [Fe/H] by requiring the metallicities be bounded between $[\text{Fe}/\text{H}]_{\min} = -2$ and $[\text{Fe}/\text{H}]_{\max} = +0.5$. We also required that the mode of ϕ , defined as $\frac{\alpha-1}{\alpha+\beta-2}$ for a Beta distribution, occurs at Solar metallicity. This leads to the

transform:

$$[\text{Fe}/\text{H}] = \left([\text{Fe}/\text{H}]_{\text{max}} - [\text{Fe}/\text{H}]_{\text{min}} \right) \left(\phi - \frac{\alpha - 1}{\alpha + \beta - 2} \right) . \quad (4.4)$$

The stars we generate mock data for in this work span from the zero-age main sequence (ZAMS) to low-luminosity subgiants. We draw equivalent evolutionary phase (EEP) values from a uniform distribution $\text{EEP} \sim \mathcal{U}(200, 450)$, where $\mathcal{U}(x, y)$ denotes a uniform prior between x and y . The bounds of this range (200 and 450) represent the ZAMS and the low-luminosity subgiant phase, respectively. Using the EEP, mass and metallicity, we interpolate a position along the MIST stellar isochrones (Morton, 2015) to calculate the expected T_{eff} and $\log g$ for each star. We also obtain the star's age (post-ZAMS) that we can use in conjunction with the other stellar parameters to determine rotational properties (see below). We have limited the age of the stars we consider in this work up to the age of the Sun. This is the range available for rotational rate. The equator surface rotation period is interpolated from stellar cluster-tuned rotational isochrones given the stellar age and mass (Table A1 in Spada et al. (2016)). This sample does not produce the observed rotational period gap and assumes a smooth distribution of rotational periods around the $R_o = 0.5$.

We evaluate the first evaluate the convective turnover timescale (τ_c^{CS}) of our sample using the scaling relation derived in Cranmer & Saar (2011),

$$\tau_c^{\text{CS}} = 314.24 \exp \left[-\frac{T_{\text{eff}}}{1952.5\text{K}} - \left(\frac{T_{\text{eff}}}{6250\text{K}} \right)^{18} \right] + 0.002d \quad (4.5)$$

from this we calculate R_o of our sample from $R_o = P_{\text{rot}}/\tau_c^{\text{CS}}$.

From R_o we obtain the scale of differential rotation of our stars. We adopt the 3 different piecewise functions to represent the evolution of the scale of differential rotation between the equator and at a latitude of 60° . The first is the observational trend found in Saar (2011), where the scale of differential rotation grows with a decrease in rotation rate below $R_o \leq 0.5$ and is constant above this limit,

$$\frac{|\Delta\Omega|}{\Omega} = \begin{cases} 0.2/(0.45^{2.5})R_o^{2.5} & R_o \leq 0.45 \\ 0.2 & 0.4 \leq R_o \end{cases}$$

where we have ensured continuity with the prefactor $0.2 / 0.45^p$, and $\Delta\Omega$ is the difference between the equator rotation rate and the rotation rate at a latitude of 60° .

The other two relations we adopt reflect two cases for the transition of the scale of

differential rotation that are steeper than the [Saar \(2011\)](#) relation that fall within the range suggested by the edges of the scale of differential rotation in [Brun et al. \(2022\)](#)

$$\text{(See Figure 8 in their work). These are: } \frac{|\Delta\Omega|}{\Omega} = \begin{cases} 0.2/(0.45^4)R_o^4 & R_o \leq 0.45 \\ 0.2 & 0.45 \leq R_o \leq 2 \\ 0.2/(2^2)R_o^2 & 2 \leq R_o \end{cases}$$

and

$$\frac{|\Delta\Omega|}{\Omega} = \begin{cases} 0.2(0.5^6)R_o^6 & R_o \leq 0.45 \\ 0.2 & 0.45 \leq R_o \leq 2 \\ 0.2/(2^2)R_o^2 & 2 \leq R_o \end{cases}$$

where the prefactors $0.2 / 0.45^4$, $0.2 / 2^4$, $0.2 / 0.45^6$, and $0.2 / 2^2$ ensure continuity. We have chosen these two relations to investigate the effect of the steepness of the relation between differential rotation and R_o on the observed rotational period distribution as well as the effect of an increase to the scale of differential rotation beyond $R_o = 2$. The relations we investigate in this work are shown in Figure ??, where we show the relation determined in [Saar \(2011\)](#) (orange), the range of the scale of differential rotation suggested by [Brun et al. \(2022\)](#) and the two steeper relations (green and purple respectively) relations we adopt in this work.

Here we assume that have solar-like differential rotation profile below $R_o = 2$ - the sign of $\frac{\Delta\Omega}{\Omega}$ is positive - and above this R_o the star instantly transitions to anti-solar like - the sign becomes negative. From this, we calculate the differential rotation by multiplying this factor by the equator rotation rate. While the instantaneous nature of this transformation may not be physical, the transition from solar-like to anti-solar-like differential rotation will have the same effect - an increase in the density of stars with observed rotational periods near the transition.

We adopt a second-order solar-like differential rotation profile with the rotation rate with inclination:

$$\Omega(\theta) = \Omega_{\text{eq}} + \frac{\Delta\Omega}{\sin^2(60^\circ)} \sin^2 \theta \quad (4.6)$$

where the prefactor $\frac{\Delta\Omega}{\sin^2(60^\circ)}$ ensures continuity.

We can then calculate the average observed rotation rate from the integral of the rotation rate given a distribution of stellar spots on a star's surface divided by the star's surface area, both calculated where the stellar spots are expressed. Here we are assuming that

all stars in our sample are viewed equator-on. While this is not the case for all stars, the rotational period gap is not an effect of the observation angle. Further, inclination angles are uniformly distributed in $\cos i$, and stars must be viewed close to the equator for their rotation periods to be measurable (see Section 4.1) - therefore, most stars with observed rotation profile are close to equator-on.

The distribution of stellar spots on the surfaces of these stars requires some thought. While the probability distribution of stellar spots of the Sun is well known, this distribution does not account for the variation of the distribution of spots with mass, equator rotation rate or differential rotation. [Granzer & Strassmeier \(2003\)](#) performed magnetohydrodynamic simulations of rotating low-mass stars in the Pleiades and determined the distribution of stellar spots of stars of various masses and rotation rates (see Figure 3. in their work). We adapt their findings to suit the work we complete here. We take the sparse grid of grid of equator rotation rates and stellar masses and measure the maximum and minimum latitudes that stellar spots are expressed for those models. In this work, we assume that stellar spots are uniformly distributed between the maximum and minimum latitudes that stellar spots are expressed. While their work explicitly contradicts this assumption, their distributions are decidedly non-uniform, their grid is sparse, and we cannot easily interpolate between distributions of stellar spots. Furthermore, the stellar spot distributions can be skewed towards the equator and the pole, dependent on the mass and rotation rate of the model - any shape of the distribution that we assume does not adequately reflect the presented stellar spot distributions in their work.

If the stellar spots are uniformly distributed, then the average rotation rate of the surface is simply the average rotation rate between the edges of the latitudes where the stellar spots are expressed. The average rotation rate is calculated from the integral of the rotation rate divided by the surface area both over the maximum and minimum latitudes that the spots are expressed,

$$\Omega_{\text{avg}} = \frac{\int_{\theta_{\min}}^{\theta_{\max}} \Omega(\theta) \sin(\theta) d\theta}{\int_{\theta_{\min}}^{\theta_{\max}} \sin(\theta) d\theta} \quad (4.7)$$

where rotation rate is independent of radius and azimuthal angle, and their contributions cancel. Here θ_{\max} and θ_{\min} are the upper and lower bounds of the distribution of spots

on the surface of the star. Because the rotation profile is symmetric about the equator of rotation we only need to calculate the contribution to the rotation rate in one hemisphere.

We compare the effect of each of the chosen relations between differential rotation and R_o on the observed rotation period of $0.7M_\odot$ star in Figure 4.16. The growth of differential rotation below $R_o < 0.45$ is observed at $P_{\text{rot,injected}} \approx 20$ d. Steeper relations of R_o with differential rotation in this range result in a quicker growth in observed rotation periods for the same injected period. The steeper the growth of the observed rotational period, the lower the number of stars that would be observed with that rotational period, while the transition from solar-like to anti-solar-like rotation ($P_{\text{rot,injected}} = 70$ d) results in an instantaneous transition from observed rotational periods greater than the injected value, to an observed rotational period less than the injected value.

Under these assumptions, the observed rotation period under each relation of differential rotation and R_o of the stars in our synthetic sample can be calculated. The resulting distributions of stars (blue, orange, green and purple) relative to the observed distribution of *Kepler* rotational periods measured in [McQuillan et al. \(2014\)](#) (black) are shown in Figure 4.17. Here, the colour of each distribution corresponds to the same colour showing the relation between differential rotation and R_o in Figure 4.15 and blue corresponds to the injected, or flat rotation profile observed, rotational period. For clarity, we have also shown the 2D histograms of the distributions in Figure 4.18 where the effects are more recognisable.

Comparing the rotational distributions under these differential rotation relations, we observe that a dearth of observations occurs when a transition from latitudinally flat to solar-like differential rotation at $R_o = 0.45$ is introduced to calculate the observed rotation rate of stars. Further, the increased density of observation of stars above the intermediate period gap in the *Kepler* sample is reproduced under this model - unlike a model of extreme magnetic braking to explain the gap. The distinctness, or rather the decrease in density of stars within the gap, increases with the power on $R_o \leq 0.45$. However, the decreased density of stars within the gap is, qualitatively, most accurately reflected by the observationally prescribed relation between R_o and scale of differential rotation found in [Saar \(2011\)](#).

We also find an over-density of stars where the transition from solar-like to anti-solar-like latitudinal differential rotation occurs ($\log P_{\text{rot}} = 1.2$, $T_{\text{eff}} = 6000K$). While the

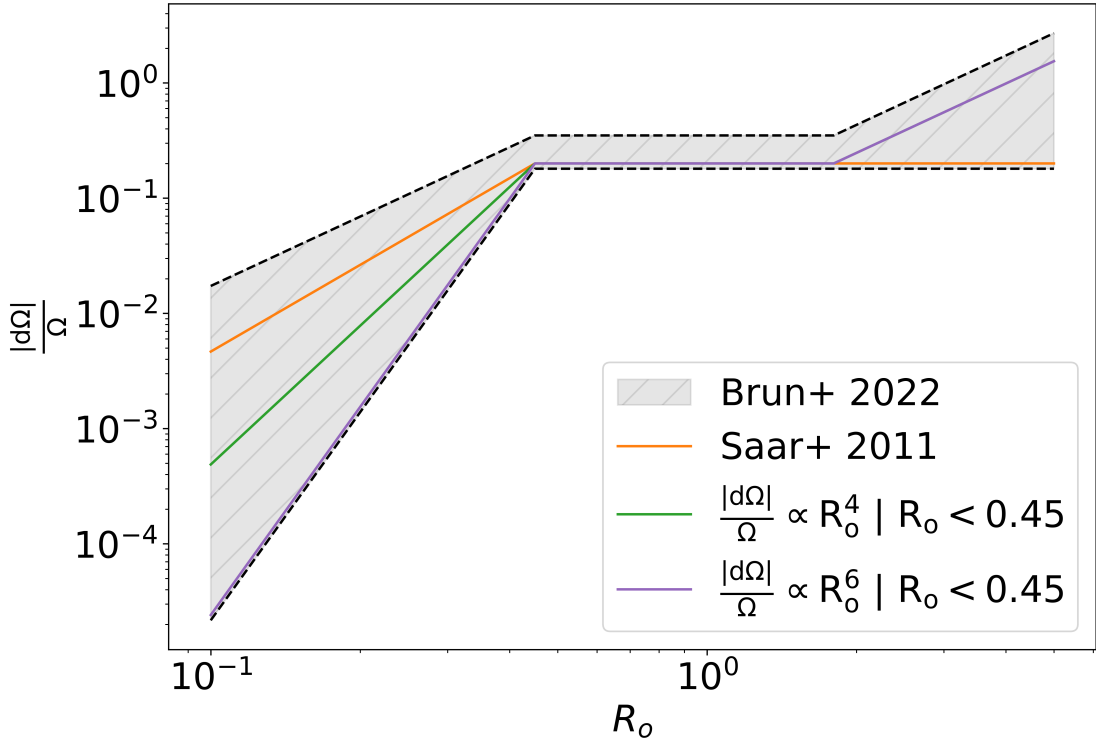


FIGURE 4.15: The various relationships between latitudinal differential rotation and the stellar R_o adopted in this work. We compare between the observationally derived relation from [Saar \(2011\)](#) (orange) and two steeper relations for $R_o \leq 0.45$, $|\Delta\Omega|/\Omega \propto R_o^4$ (green) and $|\Delta\Omega|/\Omega \propto R_o^6$ (purple). The scale of differential rotation is greater for the latter two relations and we have an increase to the scale of differential rotation for $R_o \geq 2$. All three relations are consistent with the magnetohydrodynamic investigations into stellar differential rotation from [Brun et al. \(2022\)](#).

observed *Kepler* rotation periods do contain a high density of stars near this location, we are hesitant to suggest whether this feature is the result of this transition or from the selection function of *Kepler* observations being biased towards higher mass, brighter, stars. Further, given the small number of nearby, old (≥ 3 Gyr) clusters in the *Kepler* field, and the evolution of rotational spin-down with variations to the latitudinal differential rotation, we believe that the cluster-tuned isochrones used in this work to determine the rotational periods of stars are less reliable for these stars.

4.7 Summary, Discussion, and Future Work

In this Chapter, we have investigated the distributions of the magnetic activity of stars in regard to their rotational period - specifically near the rotational period gap. We have reconfirmed that the gap aligns with a minima in the photometric variability range (R_{per}). The coincidence of the gap and the minima has been invoked to suggest that

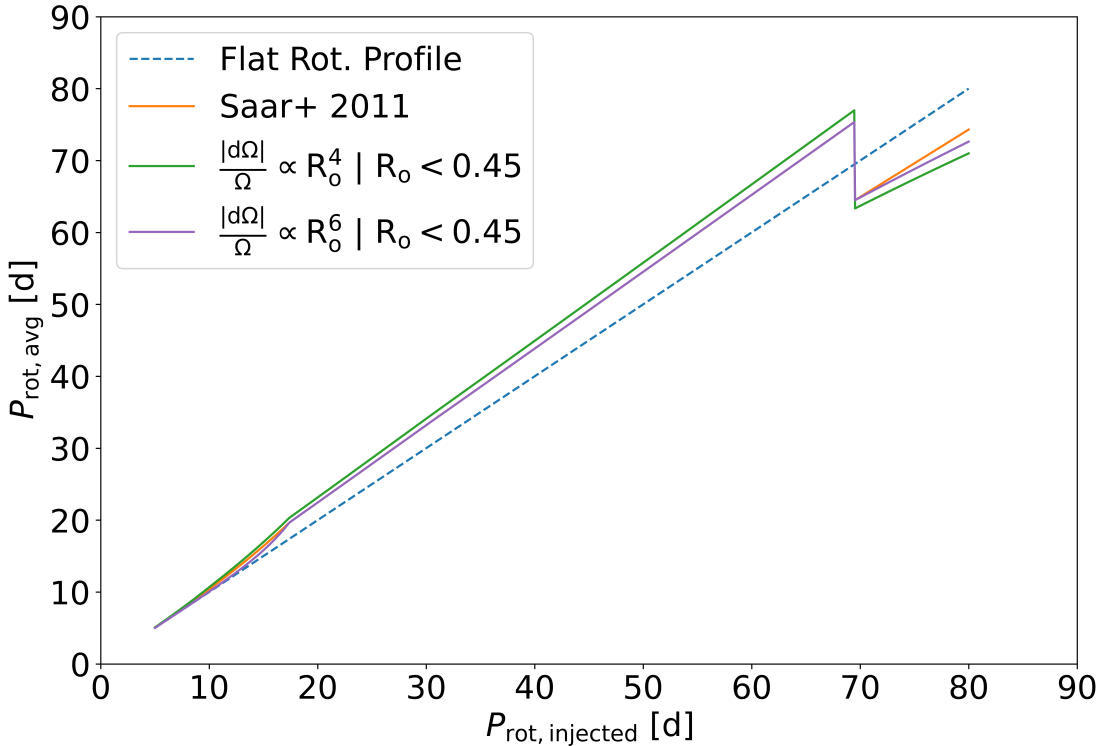


FIGURE 4.16: The effect of the differential rotation on the observed rotational period of a $0.7 M_{\odot}$ star. Here the colour of the relations corresponds to the adopted differential rotation relation in Figure 4.15 compared to the observed rotation profile of a latitudinally flat rotating star. At $R_o < 0.45$ for injected rotation periods ($P_{\text{rot,injected}}$) less than 20 days. It is evident that steeper relations between R_o and differential rotation lead to more rapid growth in observed rotation periods for the same injected period. Moreover, a steeper growth in the observed rotational period corresponds to a lower number of observed stars with that particular rotation period. The transition from solar-like to anti-solar-like rotation, occurring at $P_{\text{rot,injected}} = 70$ days, results in an instantaneous shift in observed rotational periods from being greater than the injected value to being less than the injected value.

the gap results from a very low probability of observing stars within the gap and that the gap is, in fact, full of stars with undetectable rotation periods. The average R_{per} of stars around the gap does not fall below the detectability threshold of rotation - stars with much lower R_{per} have detectable rotation periods can be detected.

One explanation could be that R_{per} could drop suddenly and dramatically, below the rotation detectability threshold, for stars precisely within the gap. Whether this be from a drop to the magnetic activity of stars within the gap to little to no expression of stellar spots or, as ? suggests, the result of the cancellation brightness variations of spots by faculae is currently unknown. We found in this work that the drop in R_{per} , and thus the gap, is also coincident with a drop in $\log R_{\text{HK}}^+$ suggesting that the decrease in photometric variability in stars close to the gap is the result of a decrease in magnetic

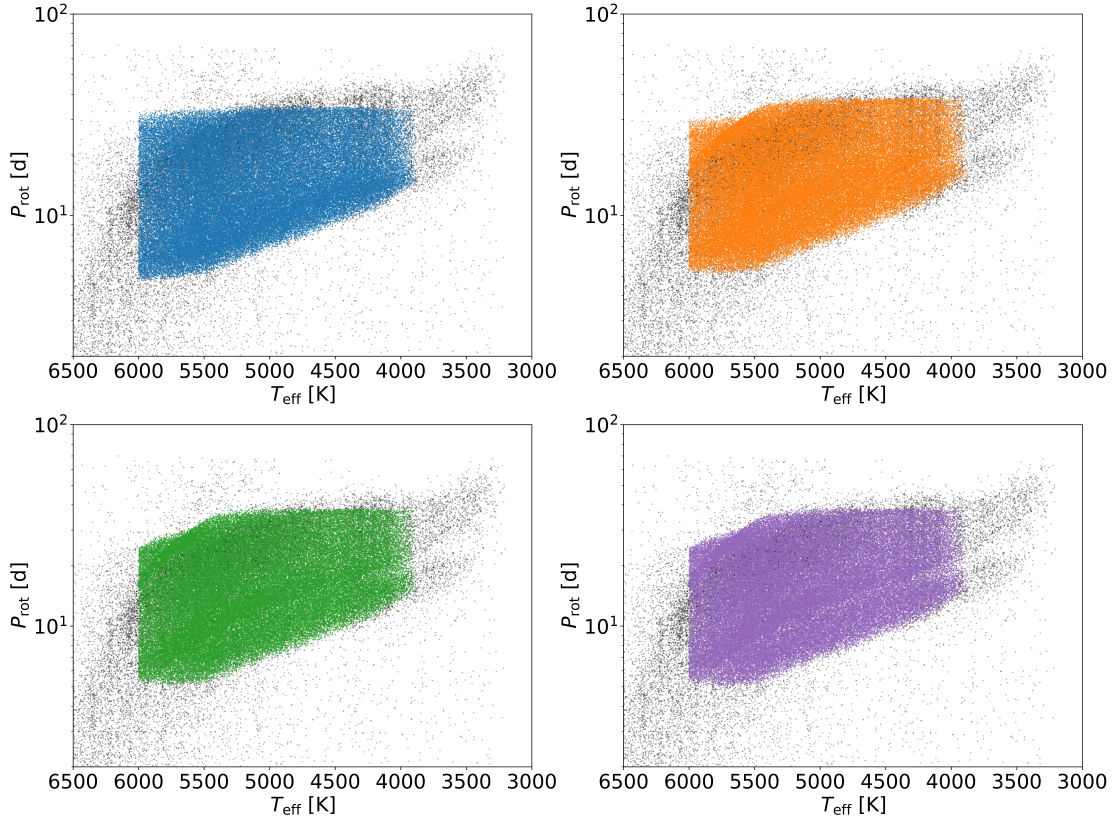


FIGURE 4.17: The observed rotational period distributions of the synthetic sample of stars given various relations between latitudinal differential rotation and R_o overlayed over the observed distribution of rotational periods of the Kepler sample from [McQuillan et al. \(2014\)](#) (black). Here, the coloured observed rotational period distributions correspond to the various differential rotation relations adopted in this work, as seen in Figure 4.15. The latitudinally flat (blue, top left) sample reflects the injected rotational periods of our sample considered in this work. We observe that there is no intermediate period gap in this synthetic sample of stars without differential rotation. If we include the effects of differential rotation on the observed rotation period, a dearth of observations at the transition between latitudinally flat ($R_o < 0.45$) and solar-like rotation occurs precisely at the location of the intermediate period gap. Further, we find that as the steepness of the relation between $|\Delta\Omega|/\Omega$ increases (where in order of increasing steepness, we have the orange, green and purple distributions) the gap becomes more distinct - fewer stars are observed within the gap. We also find that due to the transition from solar-like to anti-solar-like differential rotation, we obtain an over-density of stars consistent with the overdensity of slow-rotating stars near 6000K. See ?? for 2D histograms of the distribution of rotation periods in these panels.

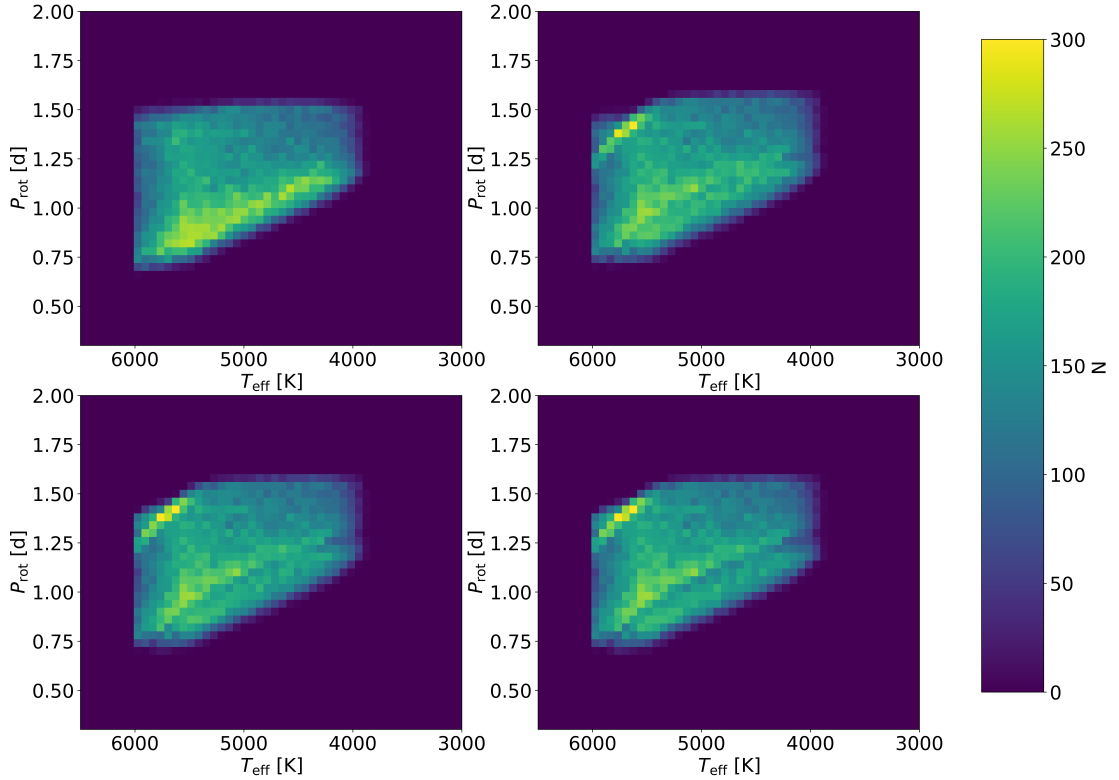


FIGURE 4.18: A 2D histogram of the synthetic observed rotational period distribution assuming various relations between the scale of differential rotation and R_o . Here, the panels correspond to the same panels in Figure 4.17.

activity, rather than a transition in the spots dominance to faculae dominance. However, we also found that there is not a subsample of stars without rotational period detection but with ultra-low $\log R_{\text{HK}}^+$. While the stars without rotational period detection tend to have lower magnetic activity, there is not an obvious subsample of stars with $\log R_{\text{HK}}^+$ below the rotation period detection threshold. This suggests that there are no stars within the gap with ultra-low magnetic activity that make rotational period observation impossible.

Another possible mechanism we can investigate using this data arises if we consider that stars within the gap may have magnetic activity so great that noise dominates their light curves making observation of their rotation impossible. Rotation tends to be less readily detectable at high activity when the light curve is noisy from the stochastic production of a larger number of surface features. Consider a scenario whereby the average magnetic activity of stars increases in the region of evolution around the magnetic activity gap. Indeed, the magnetic activity of stars tends to decrease with rotation rate, but we will ignore this for now. Let us assume instead that the spot-faculae cancellation

does not occur and that brightness variations on a magnetic activity timescale are spot dominated below the Vaughn-Preston Gap ⁴. Conceivably, as the average magnetic activity increases for stars near the gap, the regions where noise is minimal enough for rotation to be detected become smaller and more concentrated to times when the magnetic activity of stars is very small - which must constitute a minority of stars for a given $B_P - R_P$ and rotational period. This would coincide with a decrease in R_{per} of stars as average magnetic activity increases. The gap would then represent a region of evolution where the average magnetic activity of stars would be large enough that the noise permeates the entire magnetic activity cycle, and no rotation observations could be made. Observations of rotation period should therefore be more likely to occur when a star is minimally active and thus has the smallest observed magnetic activity- which would also correspond to a minima in observed $\log R_{\text{HK}}^+$. This would suggest that there is a population of magnetically active stars with $\log R_{\text{HK}}^+$ greater than the average magnetic activity of stars near the gap that have otherwise undetectable rotation periods. In Figure 4.11, we show that there is not a subsample low rotation detectability stars with $\log R_{\text{HK}}^+$ greater than the average of stars near the rotational period gap - suggesting that this selection mechanism is not at play.

The proposition that the rotational period gap represents a minimum of detectability of stars is not favoured by the data. Increases to detector efficiency have also not increased the observation of stars near, nor in, the intermediate period gap as each model proposed to explain the minima of detectability of rotation period predicts. The coincidence of the minima in R_{per} with minima in $\log R_{\text{HK}}^+$ along with the lack of a population of low or high $\log R_{\text{HK}}^+$ stars with low detectability suggests that minima in R_{per} cannot be explained by a spot-faculae transition nor a selection effect for stars with low or high magnetic activity near the rotational period gap. Furthermore, we found that for the gap to be explained by a lack of detection of the rotational period, stars within the gap must make up most stars in the *Kepler* non-detected rotational period sample. This explanation is unlikely due to the many factors by which rotation is not observed for all stars - inclination effects, noise drowning the rotational period signal etc. Recent works have also tentatively shown that the kinematic ages of stars above and below the rotation period gap have comparable kinematic ages (Lu et al., 2022) - suggesting no missing sample of stars that fill the gap.

⁴A distinct gap from the intermediate period gap wherein the transition from spot dominance to faculae dominance occurs in their work

The only alternative mechanism that has been proposed in the literature is the onset of strong surface angular momentum loss whereby stars "jump" the gap. However, this explanation does not have a proposed physical mechanism. As stars evolve toward the gap, their core and envelope undergo recoupling, slowing their spin-down. Cao et al. (2023) suggest that the process of core-envelope recoupling with significant angular momentum flux (See Section 4. of their work) between the core and the surface enhances the magnetic dynamo of stars, inducing larger photometric variability from greater spot coverage. The decrease in photometric variability towards the gap can be explained under this framework if the enhancement of the magnetic dynamo is dependent on the scale of the radial shear between the core and the dynamo, which decreases towards the gap if the core and envelope have completely recoupled.

Two mechanisms could then be invoked to explain the sudden enhanced spin-down: core-envelope re-decoupling or enhanced magnetic spin-down. Conceivably the core and the surface of the star can again decouple at the rotational period gap; the surface spins down at a much faster rate than below the gap resulting in the apparent dearth of observations. It is, however, not clear the effect that this decoupling would have above the gap. If the core and envelope are strongly decoupled above the gap then angular momentum transport between the core and surface is likely to reoccur, supported by the relatively flat radial differential rotation profile observed for the Sun and young subgiants (Deheuvels et al., 2015) R_{per} of stars just above the gap is similar to stars below the gap, suggesting that they do not have enhanced dynamos consistent with the strong radial shears. Further R_{per} increases with rotation period above the gap, suggesting instead that the enhancement of the dynamo by core-envelope should grow as the star evolves. For this to be the case the core-surface radial shear must grow and the core and surface must remain decoupled until recoupling enhances the magnetic dynamo. However, the gap is only apparent for a small rotational period range and the density of stars with observed rotation periods above and below the gap are consistent - suggesting that the decoupling is not slowly counteracted by core-envelope recoupling resulting in the enhanced R_{per} away from the gap.

Enhanced magnetic angular momentum loss is another possible explanation for the gap. The magnetic braking of a star is dependent on the rotation rate, mass loss rate and the strength of the magnetic field. Stars near and just above the gap are rotating slower and have smaller magnetic activity indicators than stars below the gap. Further, we found

that stars just above the gap do not show significant enhancement in $\log R_{\text{HK}}^+$. If the sudden increase in magnetic braking arises from enhancement to the magnetic field, it is not reflected in the magnetic activity of stars near the gap. The only other variable to consider here is increased mass loss. While mass loss rates of main-sequence stars are an ongoing field of research, to reflect the change in rotation period of stars passing through the gap, we speculate that the mass loss rate would need to be enhanced by several orders of magnitude compared to the observed mass loss rate of the Sun. That significant mass loss is not reflected in any other measurements of stars surrounding the gap, nor is there a known mechanism by which the enhanced mass loss would occur. As a result, currently, there is no known mechanism for said enhanced magnetic braking to arise.

Finally, in this work, we consider the effect of latitudinal differential rotation on the observed rotation periods of main-sequence stars. To do this, we developed a model to predict the observed/average rotation period of stars given models of surface latitudinal differential rotation growth from observational and 2D magnetohydrodynamical simulations of rotating main-sequence stars. The observations of latitudinal differential rotation and magnetohydrodynamical models of latitudinal differential rotation with R_o agree - suggesting that latitudinal differential rotation grows from latitudinally flat to solar-like differentially rotating at a $R_o \approx 0.5$. Introducing this differential rotation to our calculation of the average surface rotation period of stars produces a lower density of observations where the differential rotation grows.

Given that latitudinal differential rotation grows near where the rotational period gap occurs, this suggests that the underlying mechanism of the intermediate period gap is the onset of latitudinal differential rotation. We investigated several relationships between the scale of growth of latitudinal differential rotation and R_o , and the qualitatively best-fit relation is the observationally derived relation of [Saar \(2011\)](#).

The features of the rotational period gap become clear under this mechanism. Here, we will again invoke the explanation for the decrease in magnetic activity from the recoupling of the core and surface from ([Cao et al., 2023](#))

- The density of stars just above the gap is similar to the density below the gap.

While the observed rotation period of stars increases quickly within the gap, the increase tapers as the scale of differential rotation saturates when $R_o \geq 0.45$.

Compare the gradient of observed against injected rotation period above and below the gap in Figure 4.16.

- Stars above and below the gap have similar equatorial rotation rates and coupled core and surface. The decreased and similar magnetic activities of stars above and below the gap reflect this.
- Stars below and above the gap are similar in age. Reflecting the tentative observation of similar kinematic ages ([Lu et al., 2022](#))
- The rotational period gap is a reflection of an introduced bias to observed rotation rates. Increases to the sensitivity of the method used to observe rotational periods, therefore, are not expected to increase the number of stars in or near the gap. Gap stars do not need be filled by an undetected rotation period sample.

It is unclear why the intermediate period gap disappears for fully convective stars; we leave this as future work as our understanding of the differences between the magnetic dynamo of partially and fully convective stars is fundamentally changing [Lu et al. \(2023\)](#). It is possible, therefore, that the growth of latitudinal differential rotation of fully convective stars is not well described by the relations we use in this work and do not result in a dearth of observations.

If, indeed, the rotational period gap arises from the transition from latitudinally flat to solar-like differential rotation, then a contradiction arises in our method. We have assumed here that the rotational periods we generate are the equator rotation rates of those stars. We then claim that the measured rotation periods of stars are biased by the introduction of differential rotation to the surfaces of those stars - then the cluster-tuned rotation periods must be tuned from the observed (biased by differential rotation) surface rotation rates. However, the clusters used to tune the stellar spin-down rates of stars in this work have ages that place their rotational period distributions below the intermediate period gap. Further, the Sun is the only star used to tune the stellar spin-down above the gap. The cluster-tuned rotational isochrone periods used to generate this sample are interpolated between the rotational period gap and the rotational period of the Sun and thus reflect a smooth distribution between the lower edge of the intermediate period gap and solar rotation period. We do not believe this has biased the qualitative result we identify in this work.

The Sun is believed to be currently transitioning from solar-like to anti-solar-like differential rotation. As a result of this transition, the average observed, rotation period will decrease suddenly. We believe this is a feature of the measurement of the average rotation period with differential rotation. In this work, we have identified the over-density of stars with solar R_o and the shape of the upper left edge of the rotational period distribution. This results in the high density of stars observed near the solar rotation period and colour and the curved shape of the upper edge of the observed [McQuillan et al. \(2014\)](#) rotational period distribution.

We believe that this representative study of the effect of differential rotation on the observed rotation periods of stars is a promising avenue to explain the gap. Further works to confirm this mechanism with more rigorous methods. We propose the following investigations:

- Observations of the differential rotation of nearby stars with Doppler imaging above and below the rotational period gap to search for evidence of variance to latitudinal differential rotation.
- Use of more rigorous models of the latitudinal expression of stellar spots and their effect on the observed rotation period of stars. Such an analysis could first be completed with non-uniform distributions of stellar spots on the surface of stars from magnetohydrodynamic simulations of rotating stars using a similar analysis to that performed in this work. We also propose a hare and hound investigation where lightcurves of a synthetic sample of stars with model-motivated stellar spot distributions and observationally motivated differential rotation profiles are then treated as data to determine whether the rotational period gap is recovered using methods of rotational period measurement.
- Finally, we propose further modelling work to determine the evolution of surface differential rotation of fully convective stars. If surface differential rotation is suppressed or otherwise peculiar from partially convective stars, then this mechanism can fully explain the observations of [Lu et al. \(2022\)](#).

We thank Jing Hua Zhang for providing us with the magnetic activity indicators $\log R_{\text{HK}}^+$ and S values of the non-rotating sample of the Kepler-LAMOST crossmatch in their work [Zhang et al. \(2020\)](#) that made sections of this work possible.

Bibliography

- Affer L., Micela G., Favata F., Flaccomio E., Bouvier J., 2013, [Monthly Notices of the Royal Astronomical Society](#), 430, 1433
- Ahlborn F., Bellinger E. P., Hekker S., Basu S., Angelou G. C., 2020, [Astronomy & Astrophysics](#), 639, A98
- Aigrain S., et al., 2015, Monthly Notices of the Royal Astronomical Society, 450, 3211
- Albrecht S., Winn J. N., Carter J. A., Snellen I. A. G., de Mooij E. J. W., 2011, [The Astrophysical Journal](#), 726, 68
- Albrecht S., Setiawan J., Torres G., Fabrycky D. C., Winn J. N., 2013, [The Astrophysical Journal](#), 767, 32
- Amard L., Palacios A., Charbonnel C., Gallet F., Georgy C., Lagarde N., Siess L., 2019, [Astronomy & Astrophysics](#), 631, A77
- Amard L., Roquette J., Matt S. P., 2020, [Monthly Notices of the Royal Astronomical Society](#), 499, 3481
- Angus R., et al., 2020, [The Astronomical Journal](#), 160, 90
- Arlt R., Hollerbach R., Rüdiger G., 2003, [Astronomy & Astrophysics](#), 401, 1087
- Augustson K. C., Brun A. S., Toomre J., 2019, [The Astrophysical Journal](#), 876, 83
- Avallone E. A., et al., 2022, [The Astrophysical Journal](#), 930, 7
- Balbus S., Hawley J., 1994, [Monthly Notices of The Royal Astronomical Society - MON NOTIC ROY ASTRON SOC](#), 266
- Barker A. J., Jones C. A., Tobias S. M., 2019, [Monthly Notices of the Royal Astronomical Society](#), 487, 1777

- Barker A. J., Jones C. A., Tobias S. M., 2020, *Monthly Notices of the Royal Astronomical Society*, 495, 1468
- Bazot M., Benomar O., Christensen-Dalsgaard J., Gizon L., Hanasoge S., Nielsen M., Petit P., Sreenivasan K. R., 2019, *Astronomy & Astrophysics*, 623, A125
- Beck P. G., et al., 2011, *Science*, 332, 205
- Beck P. G., et al., 2012, *Nature*, 481, 55
- Bedding T. R., et al., 2011, *Nature*, 471, 608
- Belkacem K., et al., 2015, *Astronomy & Astrophysics*, 579, A31
- Benomar O., Takata M., Shibahashi H., Ceillier T., García R. A., 2015, *Monthly Notices of the Royal Astronomical Society*, 452, 2654
- Benomar O., et al., 2018, *Science*, 361, 1231
- Borucki W. J., et al., 2010, *Science*, 327, 977
- Brun A. S., Strugarek A., Noraz Q., Perri B., Varela J., Augustson K., Charbonneau P., Toomre J., 2022, *Astrophysical Journal*, 926, 21
- Cantiello M., Mankovich C., Bildsten L., Christensen-Dalsgaard J., Paxton B., 2014, *The Astrophysical Journal*, 788, 93
- Cao L., Pinsonneault M. H., 2022, *Monthly Notices of the Royal Astronomical Society*, 517, 2165
- Cao L., Pinsonneault M. H., van Saders J. L., 2023, Core-envelope decoupling drives radial shear dynamos in cool stars, <http://arxiv.org/abs/2301.07716>
- Ceillier T., et al., 2017, *Astronomy & Astrophysics*, 605, A111
- Chaboyer B., Zahn J.-P., 1992, *Astronomy and Astrophysics*, 253, 173
- Chahal D., de Grijs R., Kamath D., Chen X., 2022, *Monthly Notices of the Royal Astronomical Society*, 514, 4932
- Charbonnel C., Talon S., 2005, *Science*, 309, 2189
- Charbonnel C., Talon S., 2008,] 10.1017/S1743921308022710, 252, 163

- Charbonnel C., Vauclair S., Maeder A., Meynet G., Schaller G., 1994, *Astronomy and Astrophysics*, 283, 155
- Claytor Z. R., van Saders J. L., Llama J., Sadowski P., Quach B., Avallone E. A., 2022, *Astrophysical Journal*, 927, 219
- Cranmer S. R., Saar S. H., 2011, *Astrophysical Journal*, 741, 54
- Curtis J. L., Agüeros M. A., Douglas S. T., Meibom S., 2019, *The Astrophysical Journal*, 879, 49
- Curtis J. L., et al., 2020, *The Astrophysical Journal*, 904, 140
- Davenport J. R. A., 2017, *The Astrophysical Journal*, 835, 16
- Davenport J. R. A., Covey K. R., 2018, *The Astrophysical Journal*, 868, 151
- David T. J., Angus R., Curtis J. L., van Saders J. L., Colman I. L., Contardo G., Lu Y., Zinn J. C., 2022, *The Astrophysical Journal*, 933, 114
- Deheuvels S., et al., 2014, *Astronomy and Astrophysics*, 564, A27
- Deheuvels S., Ballot J., Beck P. G., Mosser B., Østensen R., García R. A., Goupil M. J., 2015, *Astronomy & Astrophysics*, 580, A96
- Deheuvels S., Ballot J., Eggenberger P., Spada F., Noll A., Hartogh J. W. d., 2020, *Astronomy & Astrophysics*, 641, A117
- Delorme P., Collier Cameron A., Hebb L., Rostron J., Lister T. A., Norton A. J., Pollacco D., West R. G., 2011, *Monthly Notices of the Royal Astronomical Society*, 413, 2218
- Denissenkov P. A., Pinsonneault M., Terndrup D. M., Newsham G., 2010, *The Astrophysical Journal*, 716, 1269
- Distefano E., Lanzafame A. C., Lanza A. F., Messina S., Korn A. J., Eriksson K., Cuypers J., 2012, *Monthly Notices of the Royal Astronomical Society*, 421, 2774
- Distefano E., et al., 2022, Gaia Data Release 3. Rotational modulation and patterns of colour variations in solar-like variables, <http://arxiv.org/abs/2206.05500>
- Donahue R. A., Saar S. H., Baliunas S. L., 1996, *Astrophysical Journal*, 466, 384

- Douglas S. T., Agüeros M. A., Covey K. R., Kraus A. L., 2017, [The Astrophysical Journal](#), 842, 83
- Douglas S. T., Curtis J. L., Agüeros M. A., Cargile P. A., Brewer J. M., Meibom S., Jansen T., 2019, [The Astrophysical Journal](#), 879, 100
- Dumont T., Palacios A., Charbonnel C., Richard O., Amard L., Augustson K., Mathis S., 2021, [Astronomy & Astrophysics](#), 646, A48
- Eddington A. S., 1918, [The Astrophysical Journal](#), 48, 205
- Eddington A. S., 1925, [The Observatory](#), 48, 73
- Eddington A. S., 1926, [The Internal Constitution of the Stars](#). <https://ui.adsabs.harvard.edu/abs/1926ics..book.....E>
- Eddington A. S., 1929, [Monthly Notices of the Royal Astronomical Society](#), 90, 54
- Eggenberger P., 2013, [EPJ Web of Conferences](#), 43, 01005
- Eggenberger P., Meynet G., Maeder A., Hirschi R., Charbonnel C., Talon S., Ekström S., 2008, [Astrophysics and Space Science](#), 316, 43
- Eggenberger P., Miglio A., Montalban J., Moreira O., Noels A., Meynet G., Maeder A., 2010, [Astronomy and Astrophysics](#), 509, A72
- Eggenberger P., Montalbán J., Miglio A., 2012, [Astronomy & Astrophysics](#), 544, L4
- Eggenberger P., et al., 2019, [Astronomy & Astrophysics](#), 621, A66
- Elvey C. T., 1929, [The Astrophysical Journal](#), 70, 141
- Endal A. S., Sofia S., 1978, [The Astrophysical Journal](#), 220, 279
- Fang X.-S., Zhao G., Zhao J.-K., Bharat Kumar Y., 2018, [Monthly Notices of the Royal Astronomical Society](#), 476, 908
- Fellay L., Buldgen G., Eggenberger P., Khan S., Salmon S. J. A. J., Miglio A., Montalbán J., 2021, [Astronomy & Astrophysics](#), 654, A133
- Fricke K., 1967, [Science](#), 156, 1101
- Friend D. B., Abbott D. C., 1986, [The Astrophysical Journal](#), 311, 701

- Fritzewski D. J., Barnes S. A., James D. J., Järvinen S. P., Strassmeier K. G., 2021, [Astronomy & Astrophysics](#), 656, A103
- Fuller J., Cantiello M., Stello D., Garcia R. A., Bildsten L., 2015, [Science](#), 350, 423
- Fuller J., Piro A. L., Jermyn A. S., 2019, [Monthly Notices of the Royal Astronomical Society](#), 485, 3661
- Gallet F., Bouvier J., 2013, [Astronomy & Astrophysics](#), 556, A36
- Garaud P., 2002, [Monthly Notices of the Royal Astronomical Society](#), 335, 707
- Gehan C., Mosser B., Michel E., Samadi R., Kallinger T., 2018, [Astronomy & Astrophysics](#), 616, A24
- Goldreich P., Schubert G., 1967, [The Astrophysical Journal](#), 150, 571
- Gordon T. A., Davenport J. R. A., Angus R., Foreman-Mackey D., Agol E., Covey K. R., Agüeros M., Kipping D., 2021, arXiv:2101.07886 [astro-ph]
- Gough D. O., Thompson M. J., 1990, [Monthly Notices of the Royal Astronomical Society](#), 242, 25
- Granzer T., Strassmeier K. G., 2003, in Brown A., Harper G. M., Ayres T. R., eds, Cambridge Workshop on Cool Stars, Stellar Systems, and the Sun Vol. 12, The Future of Cool-Star Astrophysics: 12th Cambridge Workshop on Cool Stars, Stellar Systems, and the Sun. pp 763–768
- Hall O. J., et al., 2021, [Nature Astronomy](#), 5, 707
- Hartman J. D., et al., 2009, [The Astrophysical Journal](#), 691, 342
- Hartman J. D., Bakos G. Á., Kovács G., Noyes R. W., 2010, A Large Sample of Photometric Rotation Periods for FGK Pleiades Stars, doi:10.48550/arXiv.1006.0950, <http://arxiv.org/abs/1006.0950>
- Hatt E., et al., 2023, [Astronomy & Astrophysics](#), 669, A67
- Heger A., 1998, PhD thesis, Technical University of Munich
- Heger A., Langer N., Woosley S. E., 2000, [The Astrophysical Journal](#), 528, 368
- Henderson C. B., Stassun K. G., 2012, [The Astrophysical Journal](#), 747, 51

- Herbst W., Bailer-Jones C. a. L., Mundt R., Meisenheimer K., Wackermann R., 2002, *Astronomy & Astrophysics*, 396, 513
- Hermes J. J., et al., 2017, *The Astrophysical Journal Supplement Series*, 232, 23
- Hollerbach R., Teeluck V., Rudiger G., 2010, *Physical Review Letters*, 104, 044502
- Irwin J., Hodgkin S., Aigrain S., Bouvier J., Hebb L., Moraux E., 2008, *Monthly Notices of the Royal Astronomical Society*, 383, 1588
- Irwin J., Aigrain S., Bouvier J., Hebb L., Hodgkin S., Irwin M., Moraux E., 2009, *Monthly Notices of the Royal Astronomical Society*, 392, 1456
- Johnstone C. P., Güdel M., Brott I., Lüftinger T., 2015a,] 10.1051/0004-6361/201425301
- Johnstone C. P., Güdel M., Lüftinger T., Toth G., Brott I., 2015b, *Astronomy & Astrophysics*, 577, A27
- Kim E.-j., MacGregor K. B., 2000, *AIP Conference Proceedings*, 537, 256
- Kippenhahn R., 1974, in Symposium-International Astronomical Union. Cambridge University Press, pp 20–40
- Kippenhahn R., 1977, *Astronomy and Astrophysics*, 58, 267
- Kippenhahn R., Thomas H.-C., 1970, in International Astronomical Union Colloquium. Cambridge University Press, pp 20–29
- Kippenhahn R., Weigert A., 1990, Stellar Structure and Evolution. <https://ui.adsabs.harvard.edu/abs/1990sse..book.....K>
- Kippenhahn R., Meyer-Hofmeister E., Thomas H. C., 1970, *Astronomy and Astrophysics*, 5, 155
- Lagarde N., Decressin T., Charbonnel C., Eggenberger P., Ekström S., Palacios A., 2012, *Astronomy & Astrophysics*, 543, A108
- Langer N., 1991, *Astronomy and Astrophysics*, 252, 669
- Lanzafame A. C., Spada F., 2015, *Astronomy and Astrophysics*, 584, A30
- Li Y., Bedding T. R., Li T., Bi S., Stello D., Zhou Y., White T. R., 2020a, *Monthly Notices of the Royal Astronomical Society*, 495, 2363

- Li T., Bedding T. R., Christensen-Dalsgaard J., Stello D., Li Y., Keen M. A., 2020b, *Monthly Notices of the Royal Astronomical Society*, 495, 3431
- Lockwood G. W., Skiff B. A., Henry G. W., Henry S., Radick R. R., Baliunas S. L., Donahue R. A., Soon W., 2007, *The Astrophysical Journal Supplement Series*, 171, 260
- Lorenzo-Oliveira, Diego et al., 2018, *A&A*, 619, A73
- Lorenzo-Oliveira D., Porto de Mello G. F., Dutra-Ferreira L., Ribas I., 2016, *Astronomy and Astrophysics*, 595, A11
- Lu Y., Curtis J. L., Angus R., David T. J., Hattori S., 2022, *The Astronomical Journal*, 164, 251
- Lu Y., See V., Amard L., Angus R., Matt S. P., 2023, An abrupt change in the stellar spin-down law at the fully convective boundary ([arXiv:2306.09119](https://arxiv.org/abs/2306.09119))
- Maeder A., 1999, *Astronomy and Astrophysics*, 347, 185
- Maeder A., 2003, *Astronomy and Astrophysics*, 399, 263
- Maeder A., 2009, *Physics, Formation and Evolution of Rotating Stars*. Springer
- Maeder A., Meynet G., 1996, *Astronomy and Astrophysics*, 313, 140
- Maeder A., Meynet G., 1997, *Astronomy and Astrophysics*, 321, 465
- Maeder A., Meynet G., 2000, *Annual Review of Astronomy and Astrophysics*, 38, 143
- Maeder A., Zahn J.-P., 1998, *Astronomy and Astrophysics*, 334, 1000
- Masuda K., 2022, *The Astrophysical Journal*, 937, 94
- Mathis S., Zahn J.-P., 2004, *Astronomy and Astrophysics*, 425, 229
- Mathis S., Prat V., Amard L., Charbonnel C., Palacios A., 2018, *Astronomy & Astrophysics*, 620
- Matt S. P., MacGregor K. B., Pinsonneault M. H., Greene T. P., 2012, *The Astrophysical Journal*, 754, L26
- McQuillan A., Mazeh T., Aigrain S., 2014, *The Astrophysical Journal Supplement Series*, 211, 24

- Meibom S., Mathieu R. D., Stassun K. G., 2009, [The Astrophysical Journal](#), 695, 679
- Meibom S., et al., 2011, [The Astrophysical Journal](#), 733, L9
- Menou K., Mer J. L., 2006, [The Astrophysical Journal](#), 650, 1208
- Messina S., Guinan E. F., 2003, [Astronomy & Astrophysics](#), 409, 1017
- Mestel L., 1953, [Monthly Notices of the Royal Astronomical Society](#), 113, 716
- Mestel L., Spitzer Jr. L., 1956, [Monthly Notices of the Royal Astronomical Society](#), 116, 503
- Metcalfe T. S., et al., 2010, [The Astrophysical Journal](#), 723, 1583
- Milne E. A., 1923, [Monthly Notices of the Royal Astronomical Society](#), 83, 118
- Mishra A., Mamatsashvili G., Galindo V., Stefani F., 2021, [Journal of Fluid Mechanics](#), 922, R4
- Montesinos B., Thomas J. H., Ventura P., Mazzitelli I., 2001, [Monthly Notices of the Royal Astronomical Society](#), 326, 877
- Moraux E., et al., 2013, [Astronomy and Astrophysics](#), 560, A13
- Morton T. D., 2015, [Astrophysics Source Code Library](#), p. ascl:1503.010
- Mosser B., et al., 2012, [Astronomy & Astrophysics](#), 548, A10
- Moyano F. D., Eggenberger P., Meynet G., Gehan C., Mosser B., Buldgen G., Salmon S. J. A. J., 2022, [Astronomy & Astrophysics](#), 663, A180
- Noyes R. W., Hartmann L. W., Baliunas S. L., Duncan D. K., Vaughan A. H., 1984, [The Astrophysical Journal](#), 279, 763
- Núñez A., et al., 2022, [The Astrophysical Journal](#), 931, 45
- Ouazzani R.-M., Marques J. P., Goupil M.-J., Christophe S., Antoci V., Salmon S. J. A. J., 2018, arXiv e-prints, 1801, arXiv:1801.09228
- Pantillon F. P., Talon S., Charbonnel C., 2007, [Astronomy & Astrophysics](#), 474, 155
- Parker E. N., 1958, [The Astrophysical Journal](#), 128, 664

- Pinçon C., Belkacem K., Goupil M. J., Marques J. P., 2017, *Astronomy & Astrophysics*, 605, A31
- Pinsonneault M. H., Kawaler S. D., Sofia S., Demarque P., 1989, *The Astrophysical Journal*, 338, 424
- Pizzolato N., Maggio A., Micela G., Sciortino S., Ventura P., 2003, *Astronomy and Astrophysics*, 397, 147
- Reinhold T., Hekker S., 2020, *Astronomy & Astrophysics*, 635, A43
- Reinhold T., Reiners A., 2013, *Astronomy and Astrophysics*, 557, A11
- Reinhold T., Bell K. J., Kuszlewicz J., Hekker S., Shapiro A. I., 2019, *Astronomy & Astrophysics*, 621, A21
- Reinhold T., Shapiro A. I., Witzke V., Némec N.-E., Işık E., Solanki S. K., 2021, *The Astrophysical Journal Letters*, 908, L21
- Rüdiger G., Schultz M., Stefani F., Mond M., 2015, *The Astrophysical Journal*, 811, 84
- Ruediger G., Gellert M., Schultz M., Hollerbach R., Stefani F., 2014, *Monthly Notices of the Royal Astronomical Society*, 438, 271
- Saar S. H., 2011, in Prasad Choudhary D., Strassmeier K. G., eds, Vol. 273, Physics of Sun and Star Spots. pp 61–67, doi:10.1017/S1743921311015018
- Santos A. R. G., Breton S. N., Mathur S., García R. A., 2021, *The Astrophysical Journal Supplement Series*, 255, 17
- Schatzman E., 1962, *Annales d'Astrophysique*, 25, 18
- See V., Roquette J., Amard L., Matt S. P., 2021, *Astrophysical Journal*, 912, 127
- Skumanich A., 1972, *The Astrophysical Journal*, 171, 565
- Soderblom D. R., Stauffer J. R., Hudon J. D., Jones B. F., 1993, *The Astrophysical Journal Supplement Series*, 85, 315
- Spada F., Lanzafame A. C., 2020, *Astronomy & Astrophysics*, 636, A76
- Spada F., Gellert M., Arlt R., Deheuvels S., 2016, *Astronomy & Astrophysics*, 589, A23
- Spina L., et al., 2020, *The Astrophysical Journal*, 895, 52

- Spruit H. C., 1999, *Astronomy and Astrophysics*, 349, 189
- Spruit H. C., 2002, [Astronomy and Astrophysics](#), 381, 923
- Spruit H., Phinney E. S., 1998, [Nature](#), 393, 139
- Strugarek A., Brun S., Zahn J., 2011, [Astronomy & Astrophysics - ASTRON ASTRO-PHYS](#), 532
- Struve O., 1930, [The Astrophysical Journal](#), 72, 1
- Struve O., Elvey C. T., 1930, [Nature](#), 125, 308
- Sweet P. A., 1950, [Monthly Notices of the Royal Astronomical Society](#), 110, 548
- Talon S., Charbonnel C., 2005, [Astronomy & Astrophysics](#), 440, 981
- Talon S., Zahn J.-P., 1997, [Astronomy and Astrophysics](#), 317, 749
- Tassoul J. L., 1978, Princeton University Press
- Tassoul J.-L., 2000, Stellar Rotation. Cambridge University Press
- Tayar J., et al., 2015, [The Astrophysical Journal](#), 807, 82
- Vaughan A. H., Preston G. W., 1980, [Publications of the Astronomical Society of the Pacific](#), 92, 385
- Weber E. J., Davis Jr. L., 1967, [The Astrophysical Journal](#), 148, 217
- Wilson T. A., Casey A. R., 2023, *Monthly Notices of the Royal Astronomical Society*, 524, 731
- Wilson T. A., Casey A. R., Mandel I., Ball W. H., Bellinger E. P., Davies G., 2023, *Monthly Notices of the Royal Astronomical Society*, 521, 4122
- Wright N. J., Drake J. J., Mamajek E. E., Henry G. W., 2011, [The Astrophysical Journal](#), 743, 48
- Zahn J.-P., 1974, in *Symposium-International Astronomical Union*. Cambridge University Press, pp 185–195
- Zahn J. P., 1975, *Memoires of the Societe Royale des Sciences de Liege*, 8, 31
- Zahn J.-P., 1992, *Astronomy and Astrophysics*, 265, 115

- Zhang J., et al., 2020, *The Astrophysical Journal Supplement Series*, 247, 9
- den Hartogh J. W., Eggenberger P., Hirschi R., 2019, *Astronomy & Astrophysics*, 622, A187
- van Saders J. L., Pinsonneault M. H., Barbieri M., 2019, *The Astrophysical Journal*, 872, 128
- von Zeipel H., 1924, *Monthly Notices of the Royal Astronomical Society*, 84, 684